

Fabrication, Characterization and Applications of Nanomechanical
Resonators

by

Tushar Shuvra Biswas

A thesis submitted in partial fulfillment of the requirements for the degree of

Doctor of Philosophy

Department of Physics
University of Alberta

©Tushar Shuvra Biswas, 2017

Abstract

Nanomechanics is a branch of nanotechnology where fundamental mechanical properties of nanomaterials are studied, for example nanomechanical resonators, tiny vibrating devices. These mechanical resonators are of interest and have a large number of potential sensing applications. In particular nanomechanical strings recently made attention for their high quality factor (Q) and simple sinusoidal mode shapes. These high- Q resonators show great promise in sensing applications and the simple mode shapes make it easy to characterize the device. Here work was performed to make one dimensional hybridized arrays of high- Q nanostrings and to show the sensing applications of different nanostrings. To accomplish this, a standard fabrication process is established to make nanostrings from high stress silicon nitride. These resonators provide high- Q and show string like behavior because of the intrinsic high stress of the material. The dissipation mechanism of a high stress silicon nitride nanostring is studied to find the loss channel of the device. This provides a new way to engineer the anchor points of the nanostring to increase the Q of the device. Then one dimensional arrays are fabricated from high- Q strings that are joined end-to-end by tiny post in between them. These arrays show strong coupling between individual connecting nanostrings and hence provide remote sensing opportunity, *i.e.* measurement performed on only one string of the array and it can acquire full information of the array. It is a state of the art device and technique

in sensing applications. To prove the concept of sensing applications of the nanostrings, explosive molecules called RDX are detected by a single high stress silicon nitride nanostring on the order of femtogram by IR absorption spectroscopy (which is the lowest amount to date by this method). In addition, a multimode analysis is developed to show better accuracy in mass sensing applications. However these devices are limited in chemical sensing applications due to the inert nature of the silicon nitride material. Therefore, a metallic layer is added to the bare silicon nitride nanostring to activate this for chemical sensing applications by a particular thiol intermediary technique. It is shown that the addition of the metallic layer does not change the quality factor of the device adversely for the fundamental mode. These devices are functionalized by thiol species to have self-assembled monolayers (SAMs). SAMs provide the opportunity to adsorb specific molecules. Here it is shown that a functionalized gold coated string, by a particular thiol species, can be used to capture acetone. After showing the potential applications of individual strings, I propose an experimental procedure for future works of my thesis, to use hybridized arrays in real sensing applications.

Dedicated to my parents.

*Narayan Chandra Biswas
and
Maya Rani Biswas*

Acknowledgements

First off, I would like to thank my mentor and supervisor, Prof. John P. Davis. I am grateful for all of the support he provided throughout my PhD program. He gave me the freedom to choose my projects for this thesis. He also provided sufficient opportunity to conduct my thesis. His friendly behavior and positive criticism made my work successful. It would not have been possible to finish this work without his excellent guidance.

I would also like to thank Prof. Kevin Beach for his collaboration with my projects. He helped me to understand and build theoretical models for my experimental results.

I would like to thank all of my group members and supporting staff. I can still remember those days we started our lab and how we have grown like a family through the last few years. All of our group members help each other in every single way. I would like to give special thanks to Bradley Hauer for his helping hand in providing theoretical insight related to my projects. I would like to extend my thanks to Allison Macdonald for her support and being a good friend. I would like to thank Callum Doolin for his support in computer programming whenever I need to compile my experimental data. I would also like to thank Paul Kim for his cordial support from the very beginning of his starting in our lab. I am also grateful to Abdul Halim Suhel for his initial help and support to adjust not only our lab environment but also to life in Canada. I would like to thank Greg Popwich for his technical support. He helped me to modify and install the experimental set-up. He also provided support in maintaining my instruments through out my graduate carrier. I would like to extend my thanks to Yikai Yang, Parnian Saberi, Hugh Ramp, Pearse Doolin, Xavier Rojas, Ruhul Amin, Tommy Clark, Holly Christiani, Clinton Potts, and Fabian Souris.

I would like to thank the Department of Physics staff for their technical and academic support. I would also like to thank the staff at the nanoFab for training me and providing opportunities to become an expert in micro- and nano-fabrication processes.

I would also like to thank all of the funding agencies who helped me to continue my research without any distraction. I am grateful to University of Alberta, along with Alberta Innovates Health Solutions (AIHS), CIFAR, Grand Challenge Canada.

Finally, I would like to thank my mother and my sister for their sacrifice to make my dream successful. I am also grateful to my wife Mawsumi Mandal for her continuous support and the best gift to me, my son Turio Turzo Biswas.

Last but not least, I would like to thank Avalon Holographics where I started my first job in Canada as a process specialist. I am thankful to them for taking me aboard before officially finishing my PhD.

Contents

1	Introduction	1
2	Background	6
2.1	Analytical theory of a simple beam	6
2.1.1	Analytical theory of a simple beam with tensile stress	10
2.1.2	Analytical theory of a beam with large tensile stress	11
2.2	Proper calibration of a nanostring to find the resonance frequency and the quality factor	12
2.2.1	Free vibration of a mass in simple harmonic motion	12
2.2.2	Free vibration with a damping force	14
2.2.3	Forced vibration with viscous damping	15
2.2.4	Resonance frequency	17
2.2.5	Quality factor	17
2.2.6	Power spectral density	19
2.3	Coupled string array	21
2.4	Frequency shift in response to added mass	25
2.4.1	Frequency shift for a single string in response to added mass	26
2.4.2	Frequency shift for a coupled string in response to added mass	31

3	Fabrication Process	34
3.1	Photolithography	34
3.1.1	Optical mask	34
3.1.2	Photoresist and substrate	36
3.1.3	Sources	38
3.2	Electron beam lithography	41
3.3	Dicing	43
3.4	Etching	43
3.4.1	Dry (plasma) etch	43
3.4.2	Wet etching	46
3.5	Characterization	48
3.5.1	Alpha-step IQ	48
3.5.2	Optical microscopes	49
3.5.3	Scanning electron microscope	50
4	Experimental Setup	52
4.1	Detection laser and collimator	52
4.2	Attenuator	54
4.3	Beam splitter and nano-stage	55
4.4	Objective	56
4.5	Detection and data acquisition	57
4.6	Vacuum chamber	58
5	Dissipation mechanism	59
5.1	Dissipation in high stress materials	59
5.2	Experiment details to detect resonance frequencies of high stress silicon nitride nanostrings	60

5.3	Theoretical framework for dissipation mechanism	61
5.4	Thermomechanical calibration and peak displacements	66
6	Remote Sensing in Hybridized Arrays	70
6.1	Mode shapes and eigenfrequencies of a hybridized array	70
6.2	Q -enhancement in coupled arrays	74
6.3	Allan deviation of frequency and amplitude	78
6.4	Remote sensing in hybridized array	80
7	Explosive Molecule Detection	83
7.1	Adding chemical specificity	83
7.2	Measurement of RDX	84
7.3	Photothermal Spectroscopy	90
7.4	Lowest RDX detection by photothermal spectroscopy	92
8	Time Resolved Mass Sensing	95
8.1	Relationship between frequency response and mass distribution . . .	95
8.2	Experimental method	97
8.3	Two-parameter mass distribution ansatz	101
8.4	Sublimation model	106
9	Gold and Silicon nitride bilayer string	109
9.1	Addition of gold on top of silicon nitride string	109
9.2	Dissipation in bi-layer nanostrings	114
9.3	Local and global heating of bi-layer nanostrings	115
9.4	Integrated actuation of bi-layer nanostrings	119

10 Metabolite Acetone Detection	124
10.1 Functionalization of a gold surface to form self assembled monolayers (SAMs)	125
10.1.1 Functionalization with 3-amino-1-propanethiol hydrochloride	125
10.1.2 Confirmation of SAMs formation on gold surface	127
10.1.3 Data from a functionalized gold and silicon nitride bi-layer string	128
10.2 Acetone detection by a functionalized nanostring	128
10.2.1 Fabrication of nanostring with two gold pads	130
10.2.2 Baseline of a silicon nitride nanostring with two gold pads . .	131
10.2.3 Functionalization of new nanostrings	135
10.2.4 Acetone detection	135
11 Metabolites sensing by hybridized arrays	138
11.1 Better frequency stability avoiding laser heating effect	138
11.2 Theoretical model to enable hybridization between a silicon nitride and gold coated silicon nitride string	139
11.3 Functionalization of two-string array	140
11.4 Parallel sensing by three-string array	141
12 Summary	142
A Frequency stability	153
A.1 Frequency stability of a silicon nitride string	153
A.2 Frequency variation of a gold and silicon nitride bilayer nanostring as a function of optical power.	155
A.3 Frequency stability of a silicon nitride string over a long period of time	156
B FIB milling	158

C Objective Comparison	161
D Sublimation Model	163
D.1 Sublimation model	163

List of Tables

8.1	Results of a sequence of RDX depositions onto nanostrings spanning four different geometries, organized by string length and deposition trial. The dagger (†) marks the one experiment in which the RDX deposition process was completely unbiased; the others involved some degree of masking in order to engineer a nonuniform mass distribution.	102
-----	---	-----

List of Figures

2.1	(a) Schematic of a simple beam with cross section A , and (b) shearing force V and bending moment M acting on two ends of a small segment of the beam. The figure is re-drawn from the ref [29].	7
2.2	A diagram of a spring attached to a mass.	13
2.3	(a) Schematic of an array of two strings which are inter-connected with a small post, and (b) spring mass model of the array.	23
2.4	The response of the relative frequency shifts of first and third harmonics of a string with respect to the position of the added mass. The graph is produced using Eq. 2.101 for the first and third modes. The relative frequency shift is normalized to $\delta m/m$	29
2.5	(a) Schematic of remote sensing of an array of two strings which are inter-connected with a small post. A small mass δm lands on string #2 and measurement performed on the string #1.	32
3.1	Drawing shows the side view (a-e) and top view (f) of device fabrication. (a) Silicon nitride wafer with photoresist (PR), (b) exposed and developed PR, (c) device after reactive ion etch (RIE), (d) device after the removal of PR, and (e) string is released by a wet etch . (f) Top view of a finished device	35
3.2	(a) An example of a mask designed using L-edit software, and (b) 5 x 5 inch hard mask with the same pattern as in (a).	36
3.3	A patterned string onto HPR 504 on a silicon nitride substrate. . .	36
3.4	The variation of HPR 504 film thickness with respect to the spinner rotation speed. The data is taken from nanoFab SOP for HPR 504. .	38
3.5	(a) Mask aligner with UV source, and (b) a patterned PR on a 100 mm diameter wafer	38

3.6	Patterned devices on PR with (a) over exposed, and (b) under exposed to UV sources. (c) A device with a trench in the middle. . . .	40
3.7	(a) A 125 μm long device patterned on PR, and (b) zoom in image of a portion of the string.	41
3.8	(a) Dicing saw (Disco DAD 321) in the NanoFab, and (b) a diced wafer using this dicing saw.	42
3.9	RIE processed on Au and Cr coated silicon nitride chips with (a) no O_2 , (b) with 5 sccm of O_2 , and (c)with 60 sccm of O_2	45
3.10	(a) A device after the gold etch, and (b) uncontrolled gold etching of a device.	46
3.11	(a) A 210 μm long released string, and (b) zoom in image of a portion of the string and an anchor pad	48
3.12	(a) A contact profilometer in the nanoFab, and (b) step height of HPR 504 measured by this profilometer.	49
3.13	(a) An optical microscope in our lab, and (b) an image taken by this microscope after the deposition of explosive molecules called RDX. .	50
3.14	(a) A scanning electron microscope in the nanoFab and (b) an SEM image of a 215 μm long silicon nitride nanostring. The scale bar is equivalent to 20 μm long.	51
4.1	Schematic of our experimental setup with major components. Here, DAQ stands for data acquisition cards and PC stands for a computer.	53
4.2	(a) A HeNe laser head, and (b) laser controller.	54
4.3	An optical attenuator.	55
4.4	A 50:50 beam splitter.	56
4.5	An optical photo-detector.	57
4.6	Photograph of our (a) home made vacuum chamber, and (c) cryogenic vacuum chamber.	58
5.1	(a)Schematic of experimental setup and (b)Scanning electron micrographs with false color of the 215 μm long silicon nitride nanostring, with scale bars in the main image and inset of length 20 μm and 3 μm , respectively	60

5.2	(a) Voltage signal of a 105 μm long string for various drive voltages. (b) Phase response of the string at corresponding drive voltage. Data are not included for low drive voltages 0.025, 0.05, 0.075 and 0.1 mV. (c) Zoomed in graph, to show how the frequency shifts to the higher value at non linear regime, and (d) zoomed in graph to show the corresponding phase shifts.	62
5.3	Cartoons showing the mode shapes of the first six harmonics of a nanostring.	63
5.4	The post-processed (a sliding average over five points) thermomechanical spectra of the first six harmonics. The data is calibrated by fitting to an analytical expression for the power spectral density function.	65
5.5	(a) Peak displacement and (b) Q from thermomechanical calibration of three devices, all 250 nm thick. Black circles are for a string 215 μm long and 2.1 μm wide, green squares for 102 μm long and 1.1 μm wide, red triangles for 74 μm long and 1.2 μm wide. The blue curve in (a) is a fit to Eq. 5.6	67
6.1	Scanning electron microscope (SEM) image of the 50 μm long string arrays with false color. (a) Several arrays with different numbers of strings(scale bar 100 μm), (b) tilted SEM image of two-string array (scale bar 2 μm) and (c) tilted and zoomed SEM image of a connecting post (scale bar 2 μm).	71
6.2	(a)–(b) antisymmetric and symmetric mode shapes for two-string array using FEM simulation, (c)–(d) thermomechanical signals, (e)–(f) driven signals with 1 mV piezoelectric drive voltage and (g)–(h) phase shift for antisymmetric and symmetric modes. Red and black lines represent the data for strings 1 and 2 in the array respectively. The Q s associated with the symmetric and antisymmetric modes are $\approx 7.6 \times 10^4$ and $\approx 10.4 \times 10^4$	72
6.3	(a) Three different mode shapes for the three-string array from FEM simulation. 1, 2, and 3 present 1st, 2nd, and 3rd string in the array respectively, (b) thermomechanical signal amplitude for three different modes for each string, (c) driven signal amplitudes for three different modes for three different strings and (d) phase angle for each string in three different modes. The red, black and orange lines represent 1st, 2nd and 3rd string in the array respectively.	75
6.4	Q comparison for a single string, a two-string and a three-string array.	76

6.5	(a)–(b) The thermomechanical signal amplitudes of the two-string array both before and after a mass deposition on the 2nd string in the array. Red and black colors represent 1st and 2nd string in the array. Dark and light colors represent PSD of the strings before and after mass deposition respectively.	77
6.6	The thermomechanical signal The stability of (a) frequency and (b) amplitude for different string array.	78
6.7	Frequency response for mass deposition on (a–c) second string and (d–f) first string in the array. Circles, squares and triangles represent individual experimental data.	81
7.1	(a) Optical image of a 100 μm long silicon nitride nanostring with RDX on the surface. Note that the RDX crystallites have an affinity for the silicon nitride surfaces (green), as compared with the underlying silicon surface (purple). Scale bar 50 μm . (b) AFM topography of RDX crystallites on an un-patterned silicon nitride surface. Scale bar 1.5 μm	85
7.2	(a) Schematic and (b) photograph of the experimental setup. The various key parts are labeled.	87
7.3	ZnSe window that allows to transmit IR laser through it.	88
7.4	The mechanical resonance frequency extracted from the power spectral density (PSD) function. (a) The frequency variation as a function of infrared wavelength for the first mode of a 215 μm long string with 2.72 pg RDX on the string. (b) The background frequency variation of the string (without shining IR laser) for the corresponding sweeping time of (a). (c) The baseline frequency variation from the silicon nitride (without RDX) as a function of infrared wavelength. (d) The photothermal signal from RDX only (light blue), after background subtraction. The dark blue curve is a multi-peak Lorentzian fit to the data.	89
7.5	The frequency shifts due to the RDX photothermal effect on the string for the first (a) and third mode (b). The corresponding background and baseline frequency traces are subtracted to get each trace in these plots. The data is taken from a 215 μm long string.	91
7.6	Data from (a–e) 174 μm long and 2 μm wide string, and (f–j) 150 μm long and 500 nm wide string, with small initial RDX deposition. The data is fit with an automated multi-peak Lorentzian fit, which helps to reveal the RDX adsorption peaks.	92

7.7	Power absorbed at $7.55 \mu\text{m}$ as a function of RDX mass adsorbed on a string. We show four different strings of 215, 200, 174 and $100 \mu\text{m}$ lengths, with 2.78, 2.2, 0.224 and 2.8 pg initial amounts of RDX deposited. They all follow a linear trend, with small differences due to varying cross-sectional areas of the strings. Error bars for power are from the Lorentzian fit to the data, and the error bars in mass are due to the variation during data acquisition.	94
8.1	Optical microscope images show a $101.7 \mu\text{m}$ nanostring with a large number of RDX crystallites physisorbed onto the device surfaces. (a), (b), and (d), show various RDX mass profiles along the string and (c) shows unbiased mass profile onto the string.	97
8.2	Multimode relative frequency shifts as a function of elapsed time from (a) $309.49 \mu\text{m}$, (b) $101.07 \mu\text{m}$, and (c) $172.60 \mu\text{m}$ long string. The initial deposited RDX amounts are 2.85, 11.8 and 0.028 pg for 309.49, 101.07, and $172.60 \mu\text{m}$ long string respectively. For visual clarity, the mode 3 and mode 5 data sets are translated upward by some arbitrary numbers.	99
8.3	Figure shows the RDX mass extracted from the data presented in the Fig. 8.2 using the two-parameter model.	104
8.4	Profiles of the mass distributed along the nanostring of length $310 \mu\text{m}$ and mass 641.88 pg at representative moments in time.	107
8.5	The instantaneous rate at which RDX desorbs from the nanostring clearly increases over time. A linear fit over the time interval [250 s, 7750 s] produces $\alpha(t) = \alpha_0 + \alpha_1 t = 0.00032865(6) + 1.445(1) \times t$. . .	108
9.1	Scanning electron microscope (SEM) image of a $210 \mu\text{m}$ long gold and silicon nitride bilayer nanostring (scale bar $20 \mu\text{m}$). The overhead view of the device is shown in inset (scale bar $2 \mu\text{m}$).	110
9.2	Optical image of the experimental setup.	112
9.3	Spatial scan of amplitude and phase of a $210 \mu\text{m}$ long string for (a) 0.852 MHz, (b) 0.981 MHz, (c) 4.229 MHz, and (d) 4.729 MHz resonance frequencies.	113
9.4	The Q variation with mode harmonics for the $210 \mu\text{m}$ long gold bilayer nanostring and a similar bare silicon nitride string. The orange circles are out-of-plane and purple triangles are in-plane Q s for the bilayer string and red squares are out-of-plane Q s for the bare string from Ref. [10]. Here the string is actuated using an external piezoelectric.	114

9.5	Relative frequency shift of the fundamental out-of-plane mode in vacuum (actuated with external piezoelectric) versus temperature as the entire sample stage is heated.	117
9.6	Absolute frequency shift of the fundamental mode in vacuum versus applied voltage using AC ohmic actuation (red squares) and corresponding device resistance (blue circles). Fit (dashed grey curve) is to Eq. 9.5.	118
9.7	Fundamental out-of-plane mode of a 210 μm long string, actuated at (a) f , and (b) $f/2$ by the AC ohmic thermal effect. The corresponding line widths are 5.28 and 5.62 Hz for figure (a) and (b) respectively. .	120
9.8	Fundamental out-of-plane mode actuated by the AC ohmic thermal effect.	121
9.9	(a) Frequency response of the first out-of-plane (lower frequency) and in-plane (higher frequency) modes in air using AC thermoelastic actuation (400 mV drive) with corresponding PSD fits (red) to extract the Q . (b) SEM of the gold bilayer nanostring after current induced failure after ≈ 450 mV AC drive. Gold has come off the device enough to break the current path, resulting in insulating behavior. Scale bar is $2\mu\text{m}$	122
10.1	(a) Structure of 3-amino-1-propanethiol hydrochloride, and (b) mechanism of imine formation.	125
10.2	XPS data shows comparison for two gold chips with same dimensions and same gold thickness. One gold chip is functionalized with 3-amino-1-propanethiol and another without functionalization. The peaks due to the existence of (a) sulfur and (b) nitrogen from the functionalized device. However no peaks are visible from the gold chip without functionalization.	126
10.3	The frequency sweep is taken from a 174 μm long string (a) before, and (b) after functionalization with 3-amino-1-propanethiol hydrochloride. 14.42 Hz and 12.55 Hz are corresponding line widths of the string before and after functionalization.	129
10.4	Optical microscope image showing a 90 μm and 1 μm wide nanostring. The optical image is taken (a) before and (b) after functionalization. .	131
10.5	SEM image are taken from a 90 μm and 1 μm wide nanostring after functionalization. (a) Full image of the device, and (b) zoomed in image of a single gold pad on the string. The scale bars are of 20 μm and 2 μm long respectively.	132

10.6	(a) Chemical structure of 11-(aminooxy)undecane-1-thiol, and (b) acetone capture scheme with a functionalized Au surface with this thiol molecule.	133
10.7	IR frequency sweep of (a) bare string, (b) after functionalization, and (c) after acetone capture.	134
10.8	(a) Baseline is subtracted from the frequency sweeps after functionalization and after acetone capture. (b) Baseline subtracted functionalized sweep is subtracted from the baseline subtracted acetone sweep.	136
11.1	Schematic shows hybridized array of a silicon nitride string and gold coated silicon nitride string.	139
11.2	Diagram of a gold pad on a bare silicon nitride string.	140
11.3	Schematic shows parallel sensing by a three-string array.	141
A.1	Frequency variation of a 215 μm long string with respect to incident optical power.	153
A.2	Frequency variation of a 200 μm long string with respect to incident optical power.	154
A.3	Frequency variation of a 175 μm long string with respect to incident optical power.	155
A.4	Frequency variation of a 175 μm long string with respect to time.	156
B.1	(a) A released device fabricated by optical lithography process. (b) The same device is trimmed by FIB milling to reduce the width and to remove the undercut. Scale bars are 1 μm long and 2 μm long respectively.	158
B.2	Frequency sweep of a 124 μm long string (a–b) before and (c–d) after trimming by FIB milling. (a) and (c) present data due to thermomechanical actuation. (b) and (d) present driven data. The corresponding line widths are 11.9, 8.48, 38.8 and 39.81 Hz for (a), (b), (c), and (d) respectively.	160
C.1	Frequency sweep of (a) first mode, (b) second mode, and (c) third mode of a 130 μm long string using 20x, 50x and 100x long working distance objectives. The line widths are 172, 166, and 151 Hz for 20x, 50x, and 100x objectives for the first mode. The line widths are 153, 148, and 145 Hz for 20x, 50x, and 100x objectives for the second mode. The line widths are 160, 139, 178 Hz for 20x, 50x, and 100x objectives for the third mode.	162

List of symbols

Q	mechanical quality factor	1
E	Young's modulus	6
I	Moment of inertia	6
L	Length	6
M	Bending moment	6
V	Shearing force	6
W	Width	6
t	Thickness	6
A	Cross sectional area	7
ρ	Mass density	7
n	Modes of the vibration	9
ω_n	Angular frequency of higher modes	10
σ	Tensile stress	10
f	Natural frequency	11
m	Mass of a resonator	12
k	Spring constant	13
ω_0	Angular frequency of fundamental mode	13
f_p	External periodic driving force	15
ξ	Damping ratio	17

E_0	Total energy of a system	18
f_d	Damping force	18
R_{yy}	Autocorrelation function	19
S_{ff}	Power spectral density function for thermal force	20
$f_{th}(t)$	Force due to thermal noise	20
Γ	Constant thermal noise	20
\mathcal{F}	Fourier transform	20
k_B	Boltzmann constant	20
μ	Mass per unit length	26
δm	Small perturbed mass	31
EBL	Electron beam lithography	33
PR	Photoresist	34
RIE	Reactive ion etch	34
LPCVD	Low pressure chemical vapor deposition	36
UV	Ultraviolet	37
DUV	Deep ultraviolet	37
SEM	Scanning electron microscope	49
σ_{Allan}	Allan deviation	77
α	Thermal expansion coefficient	88
κ	thermal conductivity	88
C	Heat capacity	115
P	Power	116
R	Electrical resistance	116

CHAPTER 1

Introduction

“There’s Plenty of Room at the Bottom”– famous quote by Richard Feynman in 1959. This quotation is believed to be the first inspiration behind the development of nanotechnology. In the late 1990, the nanotechnology field ushered in a new era in semiconductor technology. Micro- and nano-electromechanical systems (MEMS and NEMS) are branches of nanotechnology which are now rich in information and research for advanced technology.

Generally, when a mechanical system is brought to nanoscale dimensions, it exhibits high frequency as well as high mechanical responsivity. The resonance frequency of a resonator is one of its fundamental properties. The change in resonance frequency of a resonator can be used to characterize the properties of it and can also be used for sensing applications depending on a frequency shift. For example, frequency shift can be used to detect a small perturbation to the resonator’s mass using $\frac{\delta f_0}{f_0} = \frac{1}{2} \times \frac{\delta m}{m}$ (for a string with high Q), where f_0 is the resonant frequency, δf_0 is the frequency shift, δm is the small perturbation to the mass and m is the effective mass of the string. Therefore, nanoscale mechanical systems become very sensitive to their environment due to their reduced mass [1]. One of the great challenges of these devices is to maintain a large mechanical quality factor (Q). For devices with high quality factor, we have $Q = f_0/\Delta f_0$, where Δf_0 is the full width at half maximum power of the resonant lineshape. The larger the Q of a resonator, the narrower the resonant peak resulting a larger amplitude and a larger signal to noise ratio.

It is possible to fabricate high- Q resonators with nanoscale dimensions from high stressed materials such as silicon nitride [2, 3], the polymer SU-8 [4], aluminum [5] and AuPd [6]. Silicon nitride nanostrings have already demonstrated many applications including mass sensing at the level of individual molecules [7], force sensing at the attonewton level [7], and heat sensing below the yoctocalorie level [8].

I have two goals in my PhD thesis. They are to fabricate new types of ultra-sensitive nanomechanical resonators and then characterize them for use as probes of various systems. Since I was the first grad student in the Davis Lab, I had to establish a standard process for device fabrication. It is worth mentioning that all of the devices described in this thesis are fabricated by myself in the nanoFab facility at the University of Alberta. In the beginning, doubly clamped nanobeams were fabricated from high-stress silicon nitride material. This large intrinsic stress enhances the mechanical quality factor (Q) of the device [9], which is on order of 10^5 . These resonators also behave like strings rather than doubly clamped beam due to their high intrinsic tensile stress. The resonance frequency of the higher modes of a nanostring are defined as $f_n = n f_0$, where f_0 is the fundamental mode frequency and n indicates the mode number. Hence, these devices are called nanostrings instead of nanobeams in the research community. Since these high Q nanoresonators show great promise in applications, there is an ongoing interest in improving the efficiency of these devices. One of the ways to do this is to increase the Q of those devices, which requires studying its energy loss channels. To this end, I have characterized the dissipation mechanisms of high-stress silicon nitride nanostrings. Through my research, we found that the main energy losses for these nanostrings, comes from dissipation due to bending at anchor points [10, 11, 12] or the tunneling of phonons out of the string [13, 14]. The systematic analysis of dissipation for these nanostrings provides an opportunity to increase the Q further by clever designing of anchor points. Hence, we have made arrays of the nanostrings expecting to get enhanced Q by reflecting phonons back into the string instead of leaking into the substrate. Moreover, there are exciting applications of arrays of resonators such as detection of multiple molecular species simultaneously [15, 16, 17, 18]. Interestingly, these resonators can be coupled to each other to form a hybridized system [19, 20]. To date, coupled cantilevers [19, 20] or doubly clamped beams [21, 22] have been studied which are coupled through a mutual overhang. For the first time, we study strongly coupled silicon nitride nanostrings in a one-dimensional (1D) array. In our

system, nanostrings are connected end-to-end to form 1D arrays of various lengths. Particularly, nanostrings share a tiny, flexible post with each of their neighbours, with the two end strings attached to large support pads. The coupling between these strings can be tuned by controlling the geometry of the connecting posts during fabrication, allowing one to enter the regime of strong mode hybridization. Hence, we are able to detect the state of all resonators in the array, through measurements performed on a single resonator. This greatly simplifies the detection of the array and significantly reduces the need for fabrication and bonding of electrical leads [16]. Furthermore, the simple mode shape allows us to understand the coupling mechanism between individual nanostrings, while letting us compare between finite element modeling (FEM) and analytic expressions.

After successful fabrication and characterization of one dimensional hybridized arrays, I focused on finding potential applications for our nanostrings. To this end, an explosive molecule 1,3,5-Trinitroperhydro-1,3,5-triazine (RDX) was deposited onto silicon nitride nanostrings. The RDX is deposited by a chemical vapor technique [23]. To excite particular vibrational modes of RDX, a quantum cascade laser (QCL) is incorporated into our system. When the excitation IR wavelength matches with one of the vibrational mode frequencies of the molecules, the IR of that wavelength is absorbed by the RDX and results local heating. This local heating shifts the frequency of the nanostring, producing a dip in the frequency spectrum, leaving the signature of that molecule. Using this technique, we demonstrate the lowest amount of RDX (on the order of a femtogram) detection to date. However, it is noticed that the determination of effective mass of adsorbed molecules on a resonator is not straight forward for a non-uniform mass deposition. Hence, we develop a method using multi-mode analysis to provide better accuracy in mass sensing applications for a non-uniform mass distribution.

Due to the inert nature of the silicon nitride it is not a good candidate for molecule sensing applications [24, 25]. In fact, even RDX shows slow sublimation under vacuum. Generally, silicon and silicon nitride resonators are coated with gold to make them chemically functionalizable to use them as a chemical sensor. Here it is shown that metallization (53 nm of gold) of our silicon nitride nanostrings does not affect the Q of our resonators adversely. Hence, these resonators have potential to be good candidates for molecular sensing applications. Moreover, it is also shown that the nanostrings can be actuated by applying an alternating current (AC) across the

string. This helps to avoid having to use an external actuator such as piezoelectric buzzer.

In order to functionalize these nanostrings for molecular sensing applications, a thiol intermediary [26, 27] is affixed to the gold layer. Thiols work well to functionalize the gold surfaces due to the very stable gold-sulfur bond. In fact, the dissociation energy of gold-sulfur bond is higher than that of gold-gold bond [28]. In this case, a thiol compound named 11-(aminooxy)undecane-1-thiol is used to produce a self-assembled monolayer (SAM) on the gold surfaces. The thiol molecule is chosen in such a way that it bonds to acetone with a high affinity. With this thiol SAM, it is shown that it is possible to capture acetone using our functionalized strings. For future work, a method is proposed where this functionalization technique will be incorporated to hybridized arrays, to be used as sensors to detect specific molecules.

The organization of this thesis is as follows:

Chapter 2 describes the theoretical framework and calibration procedure for beam-like nanomechanical resonators. In addition, it is also shown that the frequency of a resonator can be used as a sensing parameter.

Chapter 3 describes the details of the fabrication process used to make the nanomechanical resonators in this thesis.

Chapter 4 describes the experimental set-up used to measure the nanomechanical sensors.

Chapter 5 describes the dissipation mechanism of a high stress silicon nitride nanostring. Here we systematically investigate the energy loss channels of the devices providing information which could be used to further increase the quality factor of these devices.

Chapter 6 describes the hybridization of a one dimensional array of high-stress silicon nitride nanostrings for which strong hybridization provides the opportunity for remote sensing. Included is a demonstration of remote sensing for a small amount of mass deposition by a traditional scanning electron microscope (SEM).

Chapter 7 describes the application of silicon nitride nanostrings as a detector of explosive molecules that can be identified using an IR absorption spectroscopy technique.

Chapter 8 describes a multimode analysis which provides higher accuracy in mass sensing for a non-uniform mass distributions along a nanostring.

Chapter 9 describes the metallization of silicon nitride nanostrings by depositing gold. The gold layer provides integrated actuation which obviates any external actuator, such as piezobuzzer.

Chapter 10 describes functionalization of gold coated silicon nitride nanostrings. It includes functionalization by a specific thiol molecules which provides an opportunity to detect specific metabolites, which we demonstrate using acetone.

Chapter 11 describes a method by which the functionalization technique could be applied to an array of strings as a potential technique for molecular sensing applications.

Chapter 12 outlines the summary of this thesis.

CHAPTER 2

Background

The geometry of my devices (nanoresonators) are that of a doubly clamped beam with high internal stress. In this chapter, I will review the mode shapes and mode frequencies of a simple beam. I will also discuss the mode shapes and mode frequencies of a beam with high internal stress. Then a proper calibration method is discussed, which can be used to extract the resonance frequency and quality factor of a resonator. Finally, it is shown how we can use this resonance frequency as a parameter for sensing applications.

2.1 Analytical theory of a simple beam

Fig. 2.1(a) shows a simple beam of length L , width W and thickness t . The flexural rigidity EI of the beam is assumed to be small in this case. Let us consider the transverse displacement of a small segment of the beam is y that is located at the distance x from the left end. The free-body diagram of this small segment of length dx is shown in Fig. 2.1(b). The shearing force V and bending moment M acting on this segment are indicated in this diagram clearly.

Let us now find the transverse vibration of the beam in the x-y plane. The equilibrium condition for a small element dx of the beam subjected to forces in the y-direction is [29]

$$\frac{\partial V}{\partial x} dx = -\rho A dx \frac{d^2 y}{dt^2}, \quad (2.1)$$

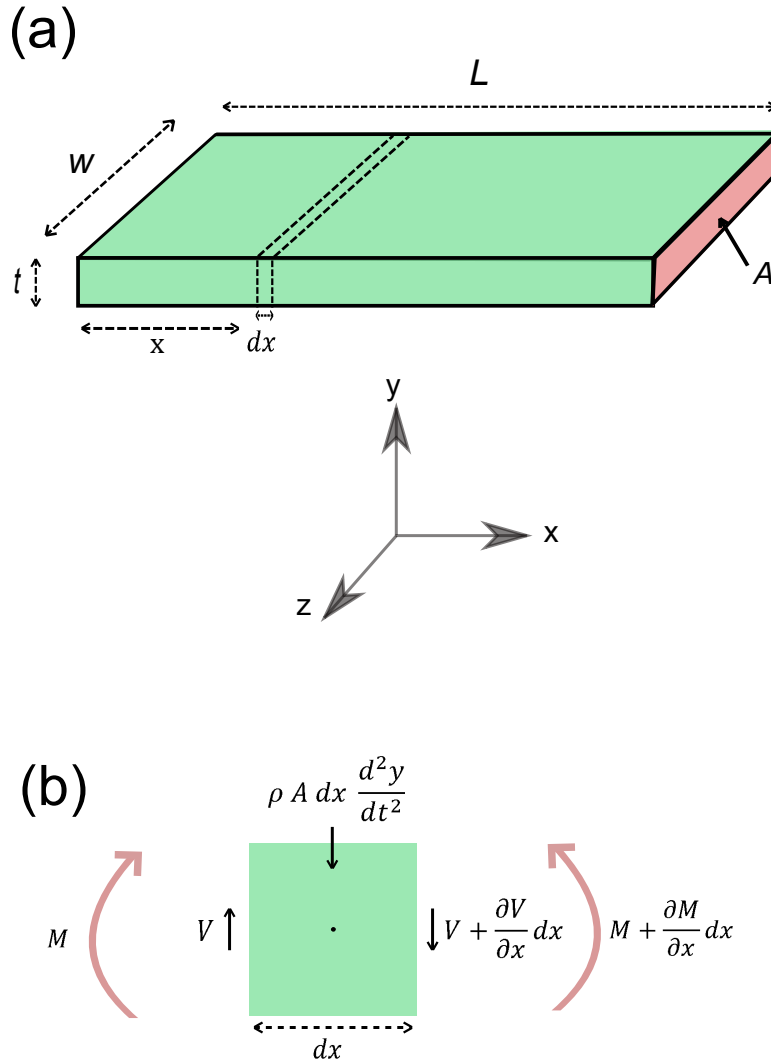


Figure 2.1: (a) Schematic of a simple beam with cross section A , and (b) shearing force V and bending moment M acting on two ends of a small segment of the beam. The figure is re-drawn from the ref [29].

where V is the shearing force, ρ is the mass density and A is the cross sectional area of the beam . Similarly, moment equilibrium condition can be written as [29]

$$V dx = \frac{\partial M}{\partial x} dx. \tag{2.2}$$

Now putting the expression for V in the Eq.2.1, we have

$$\frac{\partial^2 M}{\partial x^2} = -\rho A \frac{d^2 y}{dt^2}. \quad (2.3)$$

From Eq. 2.3 and elementary relationship $\frac{d^2 y}{dx^2} = \frac{M}{EI}$, we get the expression for transverse vibrational motion of the beam as

$$EI \frac{d^4 y}{dx^4} = -\rho A \frac{d^2 y}{dt^2}. \quad (2.4)$$

This is the general equation for free transverse vibration of a beam [29]. To solve this equation, we rewrite it as

$$\frac{d^4 y}{dx^4} = -\frac{1}{a^2} \frac{d^2 y}{dt^2}, \quad (2.5)$$

where $a^2 = \frac{EI}{\rho A}$.

Since the beam is vibrating harmonically, the deflection of the beam at one of its natural modes can be expressed as

$$y = Y(x) [A \cos(\omega t) + B \sin(\omega t)]. \quad (2.6)$$

Now Eq. 2.5 becomes

$$\frac{d^4 Y}{dx^4} = p^4 Y, \quad (2.7)$$

where $p^4 = \frac{\omega^2}{a^2}$. Consider $Y = e^{sx}$, to satisfy this equation which leads to

$$e^{sx}(s^4 - p^4) = 0. \quad (2.8)$$

Therefore, we have four different values of s which are p , $-p$, ip , and $-ip$. So the mode shape of the beam for a particular mode can be written as [29]

$$\begin{aligned} Y(x) = & C_1 [\cos(px) + \cosh(px)] + C_2 [\cos(px) - \cosh(px)] \\ & + C_3 [\sin(px) + \sinh(px)] + C_4 [\sin(px) - \sinh(px)], \quad (2.9) \end{aligned}$$

with constants C_1 , C_2 , C_3 , and C_4 . For a simply supported beam, the displacement and bending moments at each of the two end points are zero. Using these boundary conditions, we have, $Y = \frac{d^2Y}{dx^2} = 0$ at $x = 0$, and at $x = L$.

From the first two boundary conditions, we have $C_1 = C_2 = 0$. From the third boundary condition, we have

$$C_3 (\sin pL + \sinh pL) + C_4 (\sin pL - \sinh pL) = 0. \quad (2.10)$$

Imposing the last boundary condition leads to

$$C_3 (-p^2 \sin pL + p^2 \sinh pL) + C_4 (-p^2 \sin pL - p^2 \sinh pL) = 0.$$

Factoring out p^2 we then have,

$$C_3 (-\sin pL + \sinh pL) + C_4 (-\sin pL - \sinh pL) = 0. \quad (2.11)$$

By adding Eq. 2.10 and Eq. 2.11 we obtain

$$2C_3 \sinh pL - 2C_4 \sinh pL = 0,$$

which gives the result $C_3 = C_4$.

Alternatively, we could subtract Eq. 2.11 from Eq. 2.10, to get

$$2C_3 \sin pL + 2C_4 \sin pL = 0,$$

which leads to

$$\sin (pL) = 0. \quad (2.12)$$

This is the expression for a particular mode. Similarly, for all possible n modes of the vibration, the above expression can be re-written as ,

$$\sin (p_n L) = 0. \quad (2.13)$$

The roots of this equation are $p_n L = n\pi$, where $n = 1, 2, 3, \dots$. So the angular frequencies of the beam are

$$\omega_n = p_n^2 a = \frac{n^2 \pi^2}{L^2} \sqrt{\frac{EI}{\rho A}}, \quad (2.14)$$

and the natural frequencies are,

$$f_n = \frac{n^2 \pi}{2L^2} \sqrt{\frac{EI}{\rho A}}. \quad (2.15)$$

2.1.1 Analytical theory of a simple beam with tensile stress

In this section, I discuss how the results of the previous section change when tensile stress is applied to the beam. If there is a tensile stress σ acting on a beam, then its deflection can be expressed as [29]

$$EI \frac{d^4 y}{dx^4} - \sigma \frac{d^2 y}{dx^2} + \rho A \frac{d^2 y}{dt^2} = 0. \quad (2.16)$$

Again, we consider a solution to this differential equation in the form of

$$y = X(A \cos \omega t + B \sin \omega t). \quad (2.17)$$

Now Eq. 2.16 becomes

$$EI \frac{d^4 X}{dx^4} - \sigma \frac{d^2 X}{dx^2} + \omega^2 \rho A \frac{d^2 X}{dt^2} = 0. \quad (2.18)$$

After rearranging, we then have

$$\frac{d^4 X}{dx^4} - \beta \frac{d^2 X}{dx^2} + k^4 \frac{d^2 X}{dt^2} = 0, \quad (2.19)$$

where $\beta = \frac{\sigma}{EI}$. For a simply supported beam, this equation can be solved to find the expression for angular frequencies corresponding to all possible vibrational modes of the beam as [29] ,

$$\omega_n = \frac{n^2 \pi^2 a}{L^2} \sqrt{1 + \frac{\sigma L^2}{n^2 EI \pi^2}}. \quad (2.20)$$

Corresponding natural frequencies are

$$f_n = \frac{n^2 \pi a}{2L^2} \sqrt{1 + \frac{\sigma L^2}{n^2 EI \pi^2}}. \quad (2.21)$$

2.1.2 Analytical theory of a beam with large tensile stress

Now let us consider a special case when the tensile stress is large in comparison to the Young's modulus. Then the first term in the Eq. 2.16 can be neglected to obtain [30]

$$-\sigma \frac{d^2 y}{dx^2} + \rho A \frac{d^2 y}{dt^2} = 0. \quad (2.22)$$

Again consider the solution of this equation in form of

$$y = Y(A \cos \omega t + B \sin \omega t). \quad (2.23)$$

Plugging this back to Eq. 2.22, we have

$$\frac{d^2 Y}{dx^2} + b^2 Y = 0, \quad (2.24)$$

where $b^2 = \frac{\sigma \omega^2}{\rho A}$.

Consider $Y = e^{nx}$, then above equation leads to

$$n^2 + b^2 = 0. \quad (2.25)$$

This equation has two roots, $n_1 = ib$ and $n_2 = -ib$. Hence we have the solution to Eq. 2.24 as

$$Y = C_1 \cos bx + C_2 \sin bx. \quad (2.26)$$

Imposing the boundary conditions, $Y = 0$ at $x = 0$ and $Y = 0$ at $x = L$. we find that $C_1 = 0$ and $\sin bL = 0$. This is true for a particular mode. It is possible to

extend this result to n modes of vibration of the beam. In this case, we can write

$$\sin b_n L = 0. \quad (2.27)$$

This equation is satisfied for all value of $b_n = \frac{n\pi}{L}$, where $n = 1, 2, 3, \dots$. Therefore the mode shapes of this stressed beam are

$$Y = C_2 \sin\left(\frac{n\pi x}{L}\right). \quad (2.28)$$

The angular frequencies for the various modes of the beam are the

$$\omega_n = \sqrt{\frac{b_n^2 \rho A}{\sigma}} = \sqrt{\frac{n^2 \pi^2 \rho A}{L^2 \sigma}} = \frac{n\pi}{L} \sqrt{\frac{\rho A}{\sigma}}. \quad (2.29)$$

Furthermore the natural frequencies are

$$f_n = \frac{n}{2L} \sqrt{\frac{\rho A}{\sigma}}. \quad (2.30)$$

This is exactly the expression one would expect for the mode frequencies of a tensed string. Therefore, a beam with large axial stress behaves like a string under high tension.

2.2 Proper calibration of a nanostring to find the resonance frequency and the quality factor

In this section, I will discuss how to determine resonance frequency and quality factor of my resonators. To do this, it is convenient to consider our resonator as a damped simple harmonic oscillator which is driven by an external force.

2.2.1 Free vibration of a mass in simple harmonic motion

Consider a mass, m , that is attached to an end of a spring . If the mass is constrained to move in only one direction, then this system can be considered as a one dimensional system. If the mass is displaced from the equilibrium position by

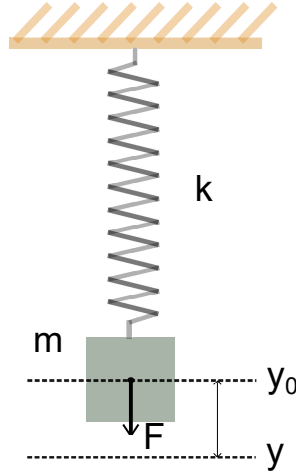


Figure 2.2: A diagram of a spring attached to a mass.

a small distance y , then the spring will exert a force $-ky$, where k is the spring constant of the spring. Furthermore, when released, the object will start to exhibit harmonic motion, with acceleration $\frac{d^2y}{dt^2}$. Assuming, there are no other forces acting on this system, we can write

$$m \frac{d^2y}{dt^2} = -ky. \quad (2.31)$$

After rearranging,

$$\frac{d^2y}{dt^2} + \omega_0^2 y = 0, \quad (2.32)$$

where $\omega_0 = \sqrt{k/m}$ is the angular frequency of the system.

The general solution of Eq. 2.32 is

$$y = A_1 \cos(\omega t) + A_2 \sin(\omega t). \quad (2.33)$$

By imposing initial conditions, it is possible to determine the value of the constants A_1 and A_2 . At $t = 0$, the object has an initial displacement y_0 and an initial velocity \dot{y}_0 . Inputting the first condition into Eq. 2.33, we have $A_1 = y_0$. Furthermore, from the derivative of Eq. 2.33 and the second condition, we have $A_2 = \dot{y}_0/\omega$.

Now the general solution for one dimensional free vibration becomes

$$y = y_0 \cos(\omega t) + \frac{y_0}{\omega} \sin(\omega t). \quad (2.34)$$

2.2.2 Free vibration with a damping force

In practice, there is always a damping force present for any system which is in simple harmonic motion. In this section, I will consider a simple viscous damping, where the damping force is $-c \frac{dy}{dt}$. The equation of motion with viscous damping can then be written as

$$m \frac{d^2 y}{dt^2} + c \frac{dy}{dt} = -ky, \quad (2.35)$$

where c is the coefficient of damping force. Re-arranging this equation, we have

$$\frac{d^2 y}{dt^2} + 2\gamma \frac{dy}{dt} + \omega_0^2 y = 0, \quad (2.36)$$

where $2\gamma = \frac{c}{m}$. The solution of this equation is of the form

$$y = Ae^{\lambda t}. \quad (2.37)$$

Plugging this into Eq. 2.36, we have

$$\lambda^2 + 2\gamma\lambda + \omega_0^2 = 0. \quad (2.38)$$

The roots of this equation are

$$\lambda_1 = -\gamma + \sqrt{\gamma^2 - \omega_0^2}, \quad (2.39)$$

and

$$\lambda_2 = -\gamma - \sqrt{\gamma^2 - \omega_0^2}. \quad (2.40)$$

Hence the general solution of a damped simple harmonic motion is [31]

$$y = e^{-\gamma t} \left[B_1 \cos \left(\sqrt{\omega_0^2 - \gamma^2} t \right) + B_2 \sin \left(\sqrt{\omega_0^2 - \gamma^2} t \right) \right]. \quad (2.41)$$

The constants B_1 and B_2 are solved by imposing the initial conditions from the previous section such that Eq. 2.41 becomes

$$y = e^{-\gamma t} \left[y_0 \cos \left(\sqrt{\omega_0^2 - \gamma^2} t \right) + \frac{\dot{y}_0 + \gamma y_0}{\sqrt{\omega_0^2 - \gamma^2}} \sin \left(\sqrt{\omega_0^2 - \gamma^2} t \right) \right]. \quad (2.42)$$

2.2.3 Forced vibration with viscous damping

After solving the damped harmonic oscillator, it is interesting to analyze this system with an applied external force. In general, a damped harmonic oscillator will die out after a certain period of time. But in practice, an external force can be applied to the system to keep the motion going. In this section, I will discuss the damped simple harmonic motion with an external periodic driving force. In this case, the equation of the motion of the system can be written as

$$m \frac{d^2 y}{dt^2} + c \frac{dy}{dt} + ky = f_p \cos(\omega t). \quad (2.43)$$

After re-arranging, this equation leads to

$$\frac{d^2 y}{dt^2} + 2\gamma \frac{dy}{dt} + \omega_0^2 y = F \cos(\omega t), \quad (2.44)$$

with $F = \frac{f_p}{m}$. One of the solutions of this equation is in the form of [29]

$$y = M \cos(\omega t) + N \sin(\omega t). \quad (2.45)$$

Putting this solution into Eq. 2.44 leads to

$$\begin{aligned} -M\omega^2 \cos(\omega t) - N\omega^2 \sin(\omega t) + 2\gamma [-M\omega \sin(\omega t) + N\omega \cos(\omega t)] \\ + \omega_0^2 [M \cos(\omega t) + N \sin(\omega t)] = F \cos(\omega t). \end{aligned} \quad (2.46)$$

After re-arranging, we have

$$(-M\omega^2 + 2\gamma N\omega + M\omega_0^2 - F) \cos(\omega t) + (-N\omega^2 - 2\gamma M\omega + \omega_0^2 N) \sin(\omega t) = 0. \quad (2.47)$$

To satisfy Eq. 2.47, we must have

$$-M\omega^2 + 2\gamma N\omega + M\omega_0^2 - F = 0, \quad (2.48)$$

and,

$$-N\omega^2 - 2\gamma M\omega + \omega_0^2 N = 0. \quad (2.49)$$

Solving Eq. 2.48 and Eq. 2.49, we find M and N to be

$$M = \frac{F(\omega_0^2 - \omega^2)}{(\omega_0^2 - \omega^2)^2 + 4\gamma^2\omega^2}, \quad (2.50)$$

and

$$N = \frac{2\gamma\omega F}{(\omega_0^2 - \omega^2)^2 + 4\gamma^2\omega^2}. \quad (2.51)$$

Therefore the total solution of Eq. 2.44 is [29]

$$y = e^{-\gamma t} \left[y_0 \cos\left(\sqrt{\omega_0^2 - \gamma^2} t\right) + \frac{y_0 + \gamma y_0}{\sqrt{\omega_0^2 - \gamma^2}} \sin\left(\sqrt{\omega_0^2 - \gamma^2} t\right) \right] + M \cos(\omega t) + N \sin(\omega t) \quad (2.52)$$

Alternatively, the Eq. 2.45 can be written as [29],

$$y = A \cos(\omega t - \theta), \quad (2.53)$$

where,

$$A = \sqrt{M^2 + N^2}.$$

and

$$\theta = \tan^{-1} \left(\frac{N}{M} \right) \quad (2.54)$$

Therefore,

$$A = \frac{F}{\sqrt{(\omega_0^2 - \omega^2)^2 + 4\gamma^2\omega^2}}, \quad (2.55)$$

and,

$$\theta = \tan^{-1} \left(\frac{2\gamma\omega/\omega_0^2}{1 - \omega^2/\omega_0^2} \right). \quad (2.56)$$

2.2.4 Resonance frequency

In the previous section, I discussed a vibrational system with an external applied force. In practice, most nanomechanical resonators (including nanostrings) behave like a damped harmonic oscillator with an external applied force. To define the resonance frequency it is convenient to re-write Eq. 2.55 for the amplitude as,

$$A = \frac{f_p/m}{\omega_0^2 \sqrt{\left(1 - \frac{\omega^2}{\omega_0^2}\right)^2 + 4\left(\frac{\gamma}{\omega_0}\right)^2 \omega^2}}. \quad (2.57)$$

Therefore,

$$A = \frac{A_0}{\sqrt{(1 - \lambda^2)^2 + 4\xi^2\lambda^2}}, \quad (2.58)$$

where $A_0 = f_p/m\omega_0^2 = f_p/k$ is the static displacement for the external force f_p , $\xi = \gamma/\omega_0$ is the damping ratio, and $\lambda = \omega/\omega_0$.

This amplitude reaches its maximum value when $\omega \approx \omega_0$ *i.e.* the frequency of the forced system is near to the frequency of the free vibration. In this case, the system is in resonance and the corresponding frequency of the system is known as the resonance frequency. Using the condition, $\frac{dA}{d\lambda} = 0$, it is possible to find the resonance frequency as [31],

$$\omega_n = \omega_0 \sqrt{1 - 2\xi^2}. \quad (2.59)$$

2.2.5 Quality factor

The quality factor (Q) of a nanomechanical system is defined as the ratio between the total energy of the system and the energy dissipated per cycle of the system.

Mathematically, this is given by [31]

$$Q = 2\pi \frac{E_0}{\Delta E_0}, \quad (2.60)$$

where E_0 is the total energy of the system and ΔE_0 is the energy lost during one cycle of the motion .

Considering a system vibrating at its resonance frequency ω_n , then the displacement of the system can be written as

$$y = A \sin(\omega_n t). \quad (2.61)$$

Now the total energy of the system is [31]

$$E_0 = \frac{1}{2} m \dot{y}^2 = \frac{1}{2} m A^2 \omega_n^2 \quad (2.62)$$

and the energy dissipated per cycle (over a period T) is

$$\Delta E_0 = - \int_0^T f_d \dot{y} dt, \quad (2.63)$$

where f_d is the damping force . Using $f_d = -c\dot{y} = cA\omega_n \cos(\omega_n t)$, we have

$$\Delta E_0 = \int_0^T c A^2 \omega_n^2 \cos^2(\omega_n t) dt. \quad (2.64)$$

Solving the integral and using $T = 2\pi/\omega_n$, we find

$$\Delta E_0 = \pi c A^2 \omega_n. \quad (2.65)$$

Therefore,

$$Q = 2\pi \frac{E_0}{\Delta E_0} = \frac{m\omega_n}{c}. \quad (2.66)$$

Now using the relation $2\gamma = c/m$ and $\xi = \gamma/\omega_0 \approx \gamma/\omega_n$, we find the relation between the Q and the damping ratio ξ as,

$$Q = \frac{\omega_n}{2\gamma} \frac{1}{2\xi} \quad (2.67)$$

2.2.6 Power spectral density

In this section I will review how we can derive the power spectral density (PSD) of a damped harmonic resonator to extract its resonance frequency and the quality factor.

In general, the motion of a resonator is detected as a voltage signal. The power spectral density (PSD) function for this signal is then defined as the square of the voltage signal divided by the measurement bandwidth. For a thermally driven resonator the PSD can be normalized by relating the resonator's time averaged motion to its thermal energy.

We start with the autocorrelation function $R_{yy}(t)$ [32] ,

$$R_{yy}(\tau) = \lim_{T_0 \rightarrow \infty} \frac{1}{T_0} \int_0^{T_0} y_n(t) y_n(t + \tau) dt, \quad (2.68)$$

which describes how the signal $y_n(t)$ is related to itself at a later time $t + \tau$. Then two-sided power spectral density function $P_{yy}(\omega)$ can be obtained from the Fourier transform of the auto-correlation function [30] as

$$P_{yy} = \int_{-\infty}^{\infty} R_{yy}(\Delta t) e^{i\omega\tau} d\tau. \quad (2.69)$$

Alternatively, the auto-correlation can be derived from the inverse Fourier transform

$$R_{yy}(\tau) = \frac{1}{2\pi} \int_{-\infty}^{\infty} P_{yy}(\omega) e^{-i\omega\tau} d\omega. \quad (2.70)$$

From Eq. 2.69 it is clear that $P_{yy}(\omega)$ spans all frequencies from $-\infty \rightarrow \infty$. However, there is no way to measure the negative frequency in practical. We then introduce a PSD $S_{yy}(\omega)$ such that $S_{yy}(\omega) = 2P_{yy}(\omega)$ [30].

Now the mean-square amplitude of the signal of our resonator can be written as [32]

$$\langle y_n^2 \rangle = \frac{1}{T_0} \int_0^{T_0} [y_n(t)]^2 dt. \quad (2.71)$$

Then we can find the relationship between the mean-square amplitude and PSD for $y_n(t)$ as [30]

$$\langle y_n^2 \rangle = \frac{1}{2\pi} \int_0^\infty S_{yy}(\omega) d\omega. \quad (2.72)$$

If $f_{th}(t)$ is the forcing function due to random thermal noise, then $S_{ff}(\omega)$ is defined as the PSD generated by this thermal force. Now it is possible to relate $S_{yy}(\omega)$ and $S_{ff}(\omega)$ as [32]

$$S_{yy}(\omega) = |H(\omega)|^2 S_{ff}(\omega), \quad (2.73)$$

where $H(\omega)$ is the frequency response function which is defined as [30]

$$H(\omega) = \frac{A_n(\omega)}{F(\omega)} = \frac{1}{m(\omega_n^2 - \omega^2 + i\omega_n\omega/Q_n)}, \quad (2.74)$$

where $A_n(\omega) = \mathcal{F}\{Y_n(t)\}$ and $F(\omega) = \mathcal{F}\{f_{th}(t)\}$ are the Fourier transforms of $Y_n(t)$ and $f_{th}(t)$. Plugging back Eq. 2.74 to Eq. 2.73, we obtain

$$S_{yy}(\omega) = \frac{\Gamma}{m^2 \left[(\omega^2 - \omega_n^2)^2 + (\omega_n\omega/Q_n)^2 \right]}, \quad (2.75)$$

where $\Gamma = S_{ff}(\omega)$, considering a constant thermal noise. Using Eq. 2.72 and Eq. 2.75, we have

$$\langle y_n^2 \rangle = \frac{1}{2\pi} \int_0^\infty \frac{\Gamma d\omega}{m^2 \left[(\omega^2 - \omega_n^2)^2 + (\omega_n\omega/Q_n)^2 \right]}. \quad (2.76)$$

Solving this equation leads to [30]

$$\langle y_n^2(t) \rangle = \frac{\Gamma Q_n}{4\omega_n^3 m^2}. \quad (2.77)$$

According to the equipartition theorem, each degree of freedom of a system possesses an average energy of $k_B T/2$ Boltzmann constant. Applying this theorem to a simple harmonic oscillator, it can be written as [33]

$$\frac{1}{2}m\omega_n^2 \langle y_n^2(t) \rangle = \frac{1}{2}k_B T. \quad (2.78)$$

From Eq. 2.77 and Eq. 2.78, we obtain

$$\Gamma = \frac{4k_B T \omega_n m}{Q_n}. \quad (2.79)$$

Finally we can write the PSD as [30, 34, 35]

$$S_{yy}(\omega) = \frac{4k_B T \omega_n}{mQ_n \left\{ (\omega^2 - \omega_n^2)^2 + \left(\frac{\omega \omega_n}{Q_n} \right)^2 \right\}}. \quad (2.80)$$

Alternatively, this PSD can be written in terms of natural frequency f as,

$$S_{yy}(f) = \frac{4k_B T f_n}{2\pi^3 m Q_n \left\{ (f^2 - f_n^2)^2 + \left(\frac{f f_n}{Q_n} \right)^2 \right\}}. \quad (2.81)$$

This is the expression for the PSD for a thermally driven resonator. However there are other sources of noise in an experimental system, which can be included in the experimentally measured PSD, $S_{vv}(f)$, as [30]

$$S_{vv}(f) = S_{vv}^\omega + \alpha S_{yy}(f), \quad (2.82)$$

where S_{vv}^ω is a constant representing the white noise of the measurement system and α is a conversion factor with units V^2/m^2 . The experimental PSD can be fit with the above Eq. 2.81 to extract the noise floor, the resonance frequency, the quality factor and the conversion factor.

2.3 Coupled string array

So far, I have only discussed a single resonator system. However, it is also interesting to study systems of multiple resonators. When these resonators are strongly coupled to each other, they exhibit hybridization of their mode frequencies. This array

system can be used in remote sensing applications as discussed in Chapter 6. For example, two cantilevers or beams can be coupled to each other through the overhang due to a wet etch [19, 22]. Similarly, two beams can be coupled to each other by the overhang [22]. The beauty of such a system is that the modes now become hybridized.

In this section, I am interested in the hybridization of a one dimensional string array formed by linear chains of strings. We start with the simple example of two coupled strings, as can be seen in Fig. 2.3(a), with the two strings connected to each other via a small pad in between them. Here, the coupling constant depends on the size of this connecting post. We can model this system using a simple spring mass system illustrated schematically in Fig. 2.3(b). Here we consider a spring, with a spring constant k_1 , that is connected to a mass m_1 and another spring, with spring constant k_2 , connected to a mass m_2 . Moreover, these two masses are inter-connected by a third spring with spring constant C . If we imagine displacing each of the masses m_1 and m_2 by an amount x_1 and x_2 , respectively. Then the equations of motion can be written as

$$m_1\ddot{x}_1 = -k_1x_1 - C(x_1 - x_2), \quad (2.83)$$

$$m_2\ddot{x}_2 = -k_2x_2 + C(x_1 - x_2). \quad (2.84)$$

Re-arranging above equations, we have

$$\ddot{x}_1 = -\left(\frac{k_1}{m_1} + \frac{C}{m_1}\right)x_1 + \frac{g}{m_1}x_2, \quad (2.85)$$

$$\ddot{x}_2 = -\left(\frac{k_2}{m_2} + \frac{C}{m_2}\right)x_2 + \frac{g}{m_2}x_1. \quad (2.86)$$

The solutions of these equations are

$$x_1 = A_1\cos(\omega t + \phi), \quad (2.87)$$

$$x_2 = A_2\cos(\omega t + \phi). \quad (2.88)$$

Note that it is assumed that both strings are vibrating at the same frequency and

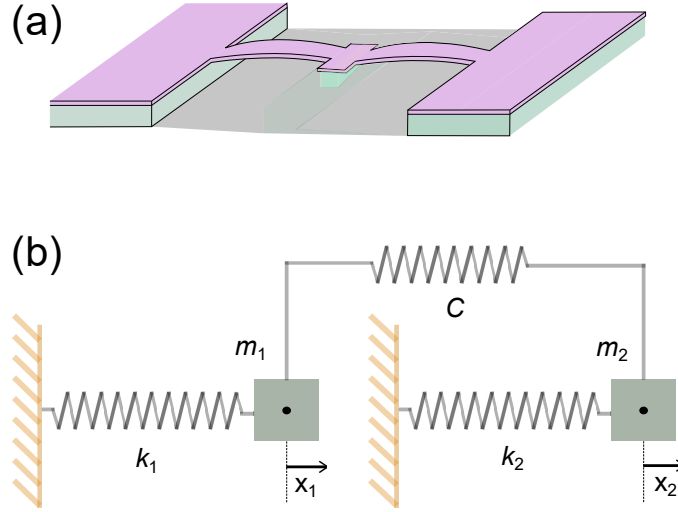


Figure 2.3: (a) Schematic of an array of two strings which are interconnected with a small post, and (b) spring mass model of the array.

in phase. After inserting these expressions into Eq. 2.85 and Eq. 2.87, we have

$$\omega^2 x_1 = \left(\frac{k_1}{m_1} + \frac{C}{m_1} \right) x_1 - \frac{C}{m_1} x_2, \quad (2.89)$$

$$\omega^2 x_2 = -\frac{C}{m_2} x_1 + \left(\frac{k_2}{m_2} + \frac{C}{m_2} \right) x_2. \quad (2.90)$$

In matrix form, these linear equations can be written as

$$\omega^2 \begin{pmatrix} x_1 \\ x_2 \end{pmatrix} = \begin{pmatrix} \frac{k_1}{m_1} + \frac{C}{m_1} & -\frac{C}{m_1} \\ -\frac{C}{m_2} & \frac{k_2}{m_2} + \frac{C}{m_2} \end{pmatrix} \begin{pmatrix} x_1 \\ x_2 \end{pmatrix}. \quad (2.91)$$

This matrix is equivalent to writing $\omega^2 X = \lambda X = AX$, where $\lambda = \omega^2$ eigenvalues, and

$$A = \begin{pmatrix} \frac{k_1}{m_1} + \frac{C}{m_1} & -\frac{C}{m_1} \\ -\frac{C}{m_2} & \frac{k_2}{m_2} + \frac{C}{m_2} \end{pmatrix},$$

and

$$X = \begin{pmatrix} x_1 \\ x_2 \end{pmatrix}.$$

We then determine the eigenvalues λ of A using

$$\begin{aligned} \det(A - \lambda I) &= 0 \\ \Rightarrow \begin{vmatrix} \frac{k_1}{m_1} + \frac{C}{m_1} - \lambda & -\frac{C}{m_1} \\ -\frac{C}{m_2} & \frac{k_2}{m_2} + \frac{C}{m_2} - \lambda \end{vmatrix} &= 0 \end{aligned}$$

Let us consider $\kappa_1 = k_1 + C$ and $\kappa_2 = k_2 + C$, then

$$\begin{vmatrix} \frac{\kappa_1}{m_1} - \lambda & -\frac{C}{m_1} \\ -\frac{C}{m_2} & \frac{\kappa_2}{m_2} - \lambda \end{vmatrix} = 0$$

which leads to

$$\lambda^2 - \lambda \left(\frac{\kappa_1}{m_1} + \frac{\kappa_2}{m_2} \right) + \left(\frac{\kappa_1 \kappa_2}{m_1 m_2} - \frac{C^2}{m_1 m_2} \right) = 0. \quad (2.92)$$

The roots of this quadratic equation are

$$\lambda = \frac{1}{2} \left[\left(\frac{\kappa_1}{m_1} + \frac{\kappa_2}{m_2} \right) \pm \sqrt{\left(\frac{\kappa_1}{m_1} + \frac{\kappa_2}{m_2} \right)^2 - 4 \left(\frac{\kappa_1 \kappa_2}{m_1 m_2} - \frac{C^2}{m_1 m_2} \right)} \right].$$

Rearranging this expression and plugging back $\lambda = \omega^2$ leads to the eigenvalues

$$\omega_{2,1}^2 = \frac{1}{2} \left[\left(\frac{\kappa_1}{m_1} + \frac{\kappa_2}{m_2} \right) \pm \sqrt{\left(\frac{\kappa_1}{m_1} - \frac{\kappa_2}{m_2} \right)^2 + \frac{4C^2}{m_1 m_2}} \right]. \quad (2.93)$$

This expression can be written in terms of natural frequency as

$$f_{2,1}^2 = \frac{1}{8\pi^2} \left[\left(\frac{\kappa_1}{m_1} + \frac{\kappa_2}{m_2} \right) \pm \sqrt{\left(\frac{\kappa_1}{m_1} - \frac{\kappa_2}{m_2} \right)^2 + \frac{4C^2}{m_1 m_2}} \right]. \quad (2.94)$$

For an array with two strings with same length and width, they will have $\kappa_1 = \kappa_2 = \kappa$ and $m_1 = m_2 = m$. Plugging these values of κ_1 , κ_2 and m_1 , m_2 back into Eq. 2.94, we have

$$\omega_{2,1}^2 = \frac{1}{m} [k \pm C].$$

This shows that splitting of frequencies of a hybridized system depends on the coupling constant between them. The spacing between coupled frequencies increases as the coupling constant of the system increases.

In similar fashion, if we form an array from N strings that are roughly the same size, then we expect hybridization to occur in bundles of N frequencies, each of which can be treated independently. The lowest possible modes, formed from the coupled fundamental frequencies of the N individual resonators, can be described by a matrix having the form

$$\begin{pmatrix} \frac{k_1}{m_1} + \frac{C}{m_1} & -\frac{C}{m_1} & 0 & \dots \\ -\frac{C}{m_2} & \frac{k_2}{m_2} + \frac{C}{m_2} & -\frac{C}{m_3} & \\ 0 & -\frac{C}{m_3} & \ddots & \\ \vdots & & & \frac{k_N}{m_N} + \frac{C}{m_N} \end{pmatrix}.$$

Therefore, this matrix can be solved to find N mode frequencies of an array made of N strings.

2.4 Frequency shift in response to added mass

Since we are going to concern ourselves with the mass sensing applications of nanostings, we must quantitatively determine the relationship between the mass adsorbed and the readout (*i.e.* the resonance frequency). In this section, I will discuss this relationship for a few simple mass distributions along a nanostring.

2.4.1 Frequency shift for a single string in response to added mass

We begin by considering the total mechanical energy of a string L vibrating in one of its normal modes:

$$E_0 = \int_0^L dx \mu(x) \omega_n^2 Y_n^2(x), \quad (2.95)$$

where x measures the distance along the string; ω_n and $Y_n(x)$ are the angular frequency and displacement profile of the n^{th} mode; and $\mu(x)$ is the mass per unit length at position x .

A small mass perturbation, arising from deposition of a distribution of mass on the surface of the string, leads to a modified mass distribution $\mu(x) \rightarrow \mu(x) + \delta\mu(x)$ and a corresponding frequency shift $\omega_n \rightarrow \omega_n + \delta\omega_n$. Now Eq. 2.95 becomes

$$\begin{aligned} E_0 &= \int_0^L dx \mu(x) \omega_n^2 Y_n^2(x), \\ &= \int_0^L dx [\mu(x) + \delta\mu(x)] [\omega_n + \delta\omega_n]^2 Y_n^2(x), \\ &= \int_0^L dx [\mu(x) + \delta\mu(x)] [\omega_n^2 + 2\omega_n \delta\omega_n + \delta\omega_n^2] Y_n^2(x). \end{aligned}$$

To leading order

$$\begin{aligned} \int_0^L dx \mu(x) \omega_n^2 Y_n^2(x) &= \int_0^L dx [\mu(x) \omega_n^2 + 2\omega_n \delta\omega_n \mu(x) + \delta\mu(x) \omega_n^2] Y_n^2(x), \\ \Rightarrow 0 &= \int_0^L dx 2\omega_n \delta\omega_n \mu(x) Y_n(x)^2 + \int_0^L dx \delta\mu(x) \omega_n^2 Y_n^2(x). \end{aligned}$$

Which leads to

$$-2 \frac{\delta\omega_n}{\omega_n} = \frac{\int_0^L dx \delta\mu(x) Y_n^2(x)}{\int_0^L dx \mu(x) Y_n^2(x)}. \quad (2.96)$$

Eq. (2.96) can be understood as a linear relationship $\delta\omega_n/\omega_n \propto \delta m/m$ between the relative frequency shift and the ratio of the mass added, $\delta m = \int_0^L dx \delta\mu(x)$, to that

of the original device, $m = \int_0^L dx \mu(x)$.

$$\begin{aligned} \frac{\delta\omega_n}{\omega_n} &\propto \frac{m}{M} \\ \frac{\delta\omega_n}{\omega_n} &= \zeta \frac{\int_0^L dx \delta\mu(x)}{\int_0^L dx \mu(x)} \quad (\text{where } \zeta \text{ is the proportionality constant}). \end{aligned}$$

Using Eq. 2.96, we obtain

$$-\frac{1}{2} \frac{\int_0^L dx \delta\mu(x) Y_n^2(x)}{\int_0^L dx \mu(x) Y_n^2(x)} = \zeta \frac{\int_0^L dx \delta\mu(x)}{\int_0^L dx \mu(x)}.$$

Therefore, the constant of proportionality

$$\zeta = -\frac{1}{2} \left(\frac{\int_0^L dx \delta\mu(x) Y_n^2(x)}{\int_0^L dx \delta\mu(x)} \right) \left(\frac{\int_0^L dx \mu(x)}{\int_0^L dx \mu(x) Y_n^2(x)} \right), \quad (2.97)$$

is unique to each mode and depends on how the resonator's own mass and the mass adsorbed on the surface are arranged.

A resonator can show different effects when mass impinges on it [36]. In devices whose vibrational modes are dominated by Young's modulus terms, a mass covering can induce surface stresses that significantly alter the bending stiffness of a resonator [37]. This is a detection technique for cantilever resonators [24, 38]. Additional mass can also provide a new pathway for energy dissipation, so that shifts in the resonant frequencies come about indirectly through changes in the mechanical quality factor. Neither of these effects is relevant to the nanostrings we are studying, since they are in the high-tension limit where the bending terms are negligible and the vibrational modes are almost perfectly harmonic. They also possess high mechanical quality factor (Q) that is quite robust to the presence of any molecular overlayer.

For a high-tension string, the mode shape is a sinusoid $Y_n(x) = (2/L)^{1/2} \sin(n\pi x/L)$, and hence

$$-2 \frac{\delta\omega_n}{\omega_n} = \frac{\int_0^L dx \delta\mu(x) \sin^2(n\pi x/L)}{\int_0^L dx \mu(x) \sin^2(n\pi x/L)}. \quad (2.98)$$

[The reflection symmetry of $Y_n^2(x)$ imposes the fundamental limitation that $\delta\mu(x)$ cannot be distinguished from $\delta\mu(L-x)$ using frequency shift measurements alone.] If the unperturbed string has a uniform mass distribution $\mu(x) = m/L$, then Eq. 2.98 can be written as

$$\begin{aligned} -2\frac{\delta\omega_n}{\omega_n} &= \frac{\int_0^L dx \delta\mu(x) \sin^2(n\pi x/L)}{(m/L) \int_0^L dx \sin^2(n\pi x/L)} \\ \Rightarrow -2\frac{\delta\omega_n}{\omega_n} &= \frac{\int_0^L dx \delta\mu(x) \sin^2(n\pi x/L)}{(m/L)(L/2)} \\ \Rightarrow -\frac{\delta\omega_n}{\omega_n} &= \frac{1}{m} \int_0^L dx \delta\mu(x) \sin^2\left(\frac{n\pi x}{L}\right). \end{aligned} \quad (2.99)$$

This result solely depends on the choice of mass distribution onto the string. For example, a string with a uniform mass deposition profile, with $\delta\mu(x) = \delta m/L$ leads to

$$-\frac{\delta\omega_n}{\omega_n} = \frac{\delta m}{2m}, \quad (2.100)$$

such that the added mass m can be determined from a *single* frequency shift measurement in any mode. However the scenario is completely different in the case of a point particle deposited at a particular position along the string. Let us consider a point mass δm deposited at position x_m on a string, then this leads to

$$-\frac{\delta\omega_n}{\omega_n} = \frac{\delta m}{m} \sin^2\left(\frac{n\pi x_m}{L}\right), \quad (2.101)$$

and hence there are two unknown quantities, δm and x_m . So we need at least two mode frequencies and hence two equations to solve these unknown parameters. Fig. 2.4 shows the variation of frequency shifts for the first and third harmonics of a string. The graph shows clear picture why one could use only the first mode to determine the effective mass of the added mass. However, it is necessary to demonstrate multimode analysis to get better accuracy to resolve the added mass.

Here I show the multimode analysis using mode 1 and 3 instead of mode 1 and 2.

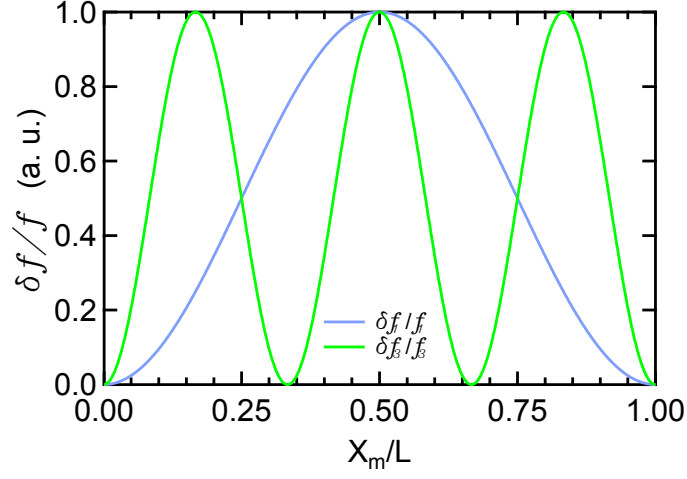


Figure 2.4: The response of the relative frequency shifts of first and third harmonics of a string with respect to the position of the added mass. The graph is produced using Eq. 2.101 for the first and third modes. The relative frequency shift is normalized to $\delta m/m$.

For mode 1, Eq. 2.101 leads to

$$\begin{aligned}
 -\frac{\delta\omega_1}{\omega_1} &= \frac{\delta m}{m} \sin^2\left(\frac{\pi x_m}{L}\right), \\
 \Rightarrow \sin^2\left(\frac{\pi x_m}{L}\right) &= \sqrt{-\left(\frac{\delta\omega_1}{\omega_1} \frac{m}{\delta m}\right)}, \\
 \Rightarrow \frac{\pi x_m}{L} &= \arcsin \sqrt{-\left(\frac{\delta\omega_1}{\omega_1} \frac{m}{\delta m}\right)}. \tag{2.102}
 \end{aligned}$$

Similarly for mode 3, Eq. 2.101 leads to

$$\begin{aligned} -\frac{\delta\omega_3}{\omega_3} &= \frac{\delta m}{m} \sin^2\left(\frac{3\pi x_m}{L}\right), \\ \Rightarrow -\left(\frac{\delta\omega_3}{\omega_3} \frac{m}{\delta m}\right) &= \sin^2\left(\frac{3\pi x_m}{L}\right), \\ \Rightarrow -\left(\frac{\delta\omega_3}{\omega_3} \frac{m}{\delta m}\right) &= \sin^2\left[3 \arcsin \sqrt{-\left(\frac{\delta\omega_1}{\omega_1} \frac{m}{\delta m}\right)}\right]. \end{aligned}$$

Using the trigonometric identity, $\sin(3\arcsin\theta) = 3\theta - 4\theta^3$

$$\begin{aligned} \Rightarrow -\left(\frac{\delta\omega_3}{\omega_3} \frac{m}{\delta m}\right) &= \left[3\left(-\frac{\delta\omega_1}{\omega_1} \frac{m}{\delta m}\right)^{1/2} - 4\left(-\frac{\delta\omega_1}{\omega_1} \frac{m}{\delta m}\right)^{3/2}\right]^2, \\ \Rightarrow -\left(\frac{\delta\omega_3}{\omega_3} \frac{m}{\delta m}\right) &= 9\left(-\frac{\delta\omega_1}{\omega_1} \frac{m}{\delta m}\right) - 24\left(-\frac{\delta\omega_1}{\omega_1} \frac{m}{\delta m}\right)^2 + 16\left(-\frac{\delta\omega_1}{\omega_1} \frac{m}{\delta m}\right)^3, \end{aligned}$$

which leads to the quadratic equation

$$\left(4\frac{\delta\omega_1}{\omega_1}\right)^2 \left(\frac{m}{\delta m}\right)^2 + \left(24\frac{\delta\omega_1}{\omega_1}\right) \left(\frac{m}{\delta m}\right) + \left(9 - \frac{\omega_1}{\delta\omega_1} \frac{\delta\omega_3}{\omega_3}\right) = 0. \quad (2.103)$$

The roots are

$$\frac{m}{\delta m} = \frac{-24\frac{\delta\omega_1}{\omega_1} \pm 24\frac{\delta\omega_1}{\omega_1} \sqrt{1 - \frac{1}{9}\left(9 - \frac{\delta\omega_3\omega_1}{\omega_3\delta\omega_1}\right)}}{32\frac{\delta\omega_1}{\omega_1}}.$$

Simplifying this equation leads to

$$-\frac{\delta m}{m} = \frac{\delta\omega_1}{\omega_1} \left[\frac{3}{4} \pm \frac{1}{4} \sqrt{\frac{\delta\omega_3/\omega_3}{\delta\omega_1/\omega_1}}\right]^{-1}. \quad (2.104)$$

Plugging this expression back into the Eq. 2.102 gives the analytical expression for

the particle position as

$$-x_m = \frac{L}{\pi} \arcsin \left[\frac{3}{4} \pm \frac{1}{4} \sqrt{\frac{\delta\omega_3/\omega_3}{\delta\omega_1/\omega_1}} \right]^{1/2}. \quad (2.105)$$

Eq. 2.104 and Eq. 2.105 are explicit solutions for a point mass deposited on a particular position of a nanostring using modes 1 and 3.

However, the practical mass sensing problem is not that straight-forward. Sometimes the adsorbed mass profile is not either uniform, or point like particle. Rather it has an arbitrary profile. We propose another model for mass sensing assuming the distributed mass is symmetric about its center, and relatively smooth and slow varying. The details of this model are described in Chapter 8.

2.4.2 Frequency shift for a coupled string in response to added mass

I would also like to show the frequency response of a coupled string-system, when a mass lands on the system. For example, for a strongly coupled system consisting of an array of two strings, as discussed in Chapter 6, the frequency demonstrates hybridization as a splitting of the two mode frequencies. As seen in Fig. 2.5, string #1 will be considered as the detection string and a small mass perturbation will be applied to string #2. My goal is to find an analytical expression to determine the deposited mass in terms of the spring constant and shifted mode frequencies of the system. Note that m_1 , k_1 and m_2 , k_2 are the mass and spring constants of string #1 and string #2, respectively. As in Chapter 6, the coupling constant of the connecting post is C . In this case, the hybridized mode frequencies can be expressed as Eq. 2.94.

If a small mass, δm , lands on string #2 (Fig. 2.5), then $m_2 \rightarrow m_2 + \delta m$. If the

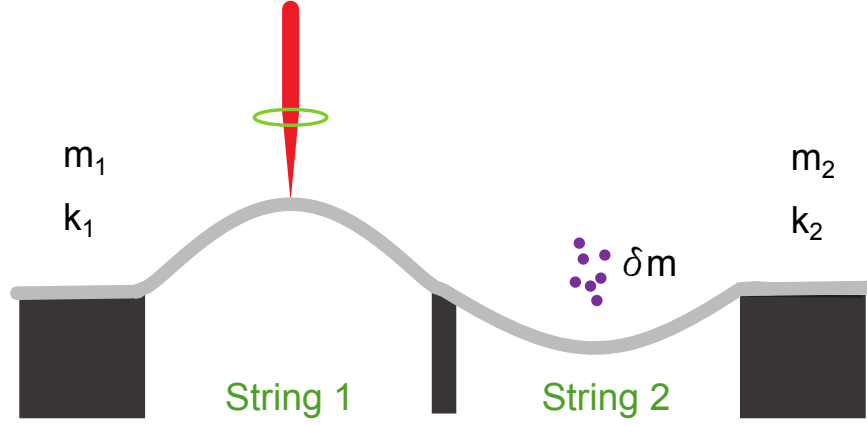


Figure 2.5: (a) Schematic of remote sensing of an array of two strings which are inter-connected with a small post. A small mass δm lands on string #2 and measurement performed on the string #1.

assumption is made that $m_2 \gg \delta m$, then

$$\begin{aligned} \frac{1}{m_2} &\rightarrow \frac{1}{m_2 + \delta m}, \\ &= \frac{1}{m_2 \left(1 + \frac{\delta m}{m_2}\right)}, \\ &= \frac{1}{m_2} \left(1 + \frac{\delta m}{m_2}\right)^{-1}. \end{aligned}$$

To leading order

$$\frac{1}{m_2} \rightarrow \frac{1}{m_2} \left(1 - \frac{\delta m}{m_2}\right). \quad (2.106)$$

$$(2.107)$$

Now $\omega_{2,1}^2$ is shifted to the new value of $\omega_{2,1}'^2$ and can be expressed from Eq. 2.94 as

$$\omega_{2,1}'^2 = \frac{1}{2} \left[\left\{ \frac{\kappa_1}{m_1} + \frac{\kappa_2}{m_2} \left(1 - \frac{\delta m}{m_2}\right) \right\} \pm \sqrt{\left\{ \frac{\kappa_1}{m_1} - \frac{\kappa_2}{m_2} \left(1 - \frac{\delta m}{m_2}\right) \right\}^2 + \frac{4c^2}{m_1 m_2 \left(1 - \frac{\delta m}{m_2}\right)}} \right].$$

Finally, we have

$$\omega_2'^2 + \omega_1'^2 = \frac{\kappa_1}{m_1} + \frac{\kappa_2}{m_2} - \frac{\kappa_2}{m_2} \frac{\delta m}{m_2}. \quad (2.108)$$

After rearranging the above equation, we get

$$\frac{\delta m}{m_2} = \left(\frac{\frac{\kappa_1}{m_1} + \frac{\kappa_2}{m_2}}{\frac{\kappa_2}{m_2}} \right) - \left(\frac{\omega_2'^2 + \omega_1'^2}{\frac{\kappa_2}{m_2}} \right). \quad (2.109)$$

This is the expression for a deposited mass on one string of a two string array. It is possible to find the value of δm from known values of spring constants and shifted new frequencies.

In this chapter, I have discussed the theoretical frameworks related to a doubly clamped beam. I have also reviewed an appropriate process to find the resonance frequency and quality factor of a thermally driven nanostring. Finally, the relationship between the frequency shift and added mass to a resonator, is discussed for different conditions. The theoretical results of this Chapter will be used to characterize our resonators in subsequent Chapters of this thesis.

CHAPTER 3

Fabrication process

It is challenging to fabricate a good nanomechanical resonator. There are many techniques to fabricate these kind of devices. Here, I will discuss briefly every step involved in our fabrication process. Schematic Fig. 3.1 shows the full fabrication process at a glimpse for a quick understanding.

3.1 Photolithography

Lithography is a process that is used to transfer a designed pattern onto a resist layer. This patterned resist is then used as a mask for a subsequent step such as etching or sputtering. I start by discussing optical lithography, as this is an easy and efficient patterning technique compared to other techniques, like electron-beam lithography (EBL). The major elements involved in the photolithography process are briefly described in this section.

3.1.1 Optical mask

A transparent substrate with a thin, opaque patterned layer is used to make the photomask for optical lithography. A transparent soda lime glass covered with a thin layer of chromium (opaque to UV rays) is used as a substrate to make a hard mask. I use a pattern generator software, like L-edit, to design my masks. Many devices of differing geometries and dimensions can be patterned into a single mask.

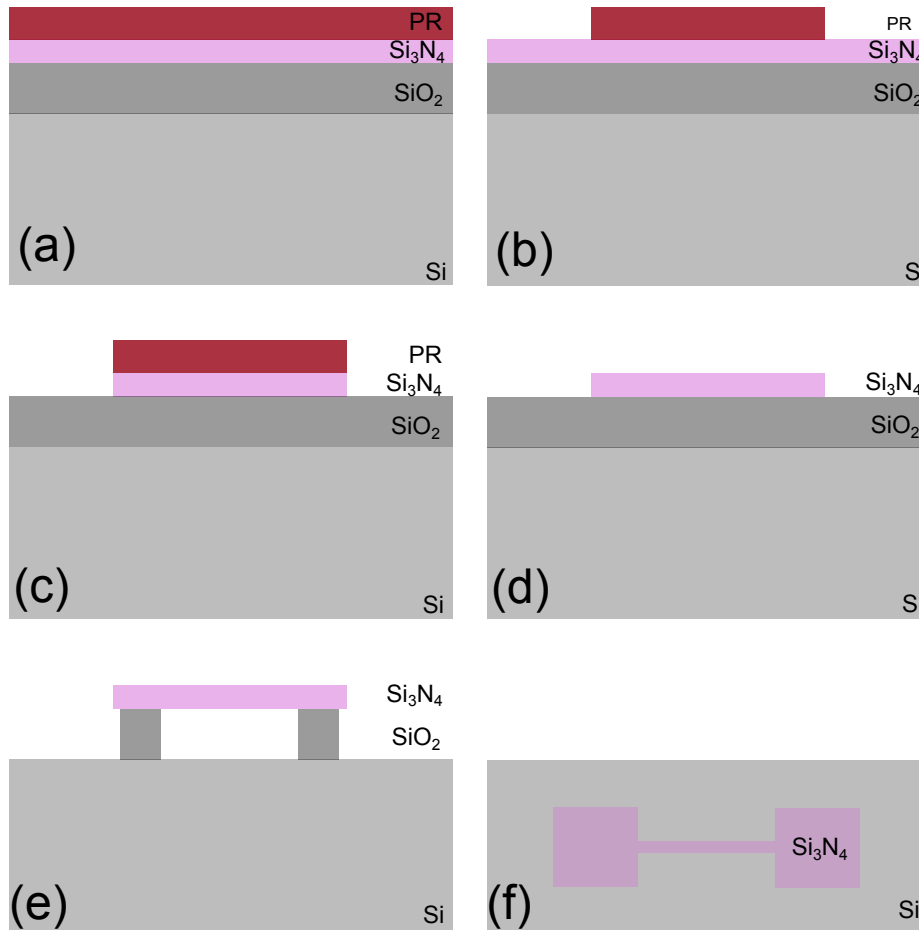


Figure 3.1: Drawing shows the side view (a-e) and top view (f) of device fabrication. (a) Silicon nitride wafer with photoresist (PR), (b) exposed and developed PR, (c) device after reactive ion etch (RIE), (d) device after the removal of PR, and (e) string is released by a wet etch . (f) Top view of a finished device

Fig. 3.2(a) shows an example of a mask designed using L-edit software. The exact pattern from the mask is then transferred onto a chromium layer using a direct write system in the NanoFab. A 5 inch by 5 inch patterned optical lithography hard mask generated using this process is shown in Fig. 3.2(b).

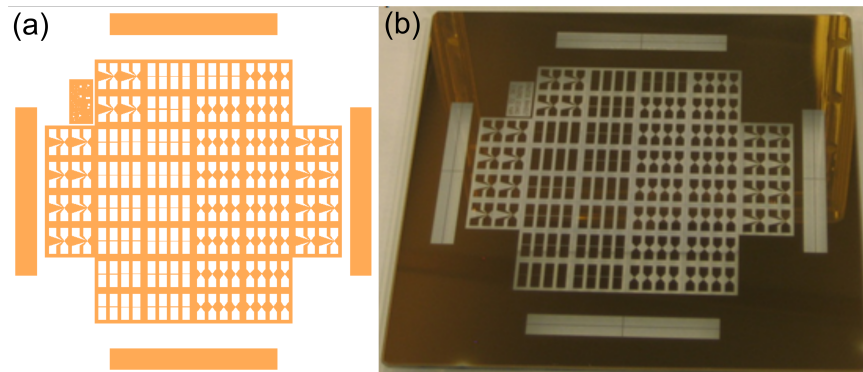


Figure 3.2: (a) An example of a mask designed using L-edit software, and (b) 5 x 5 inch hard mask with the same pattern as in (a).

3.1.2 Photoresist and substrate

The photoresist (PR) is a photosensitive organic film, containing a photoactive compound, a base resin and an organic solvent system. PR can be either positive or negative acting. Positive PR is only soluble in a developer if it is exposed to UV, whereas if a negative PR is exposed to UV, the exposed area is insoluble in a developer. The behavior of a PR depends on its sensitivity, contrast and spectral response. In general, the resolution of a positive PR is better than that of a negative PR [39].

It is also necessary to select the substrate on to which to fabricate my devices. I start with a 100 mm diameter wafer of 250 nm thick high stress silicon nitride on a

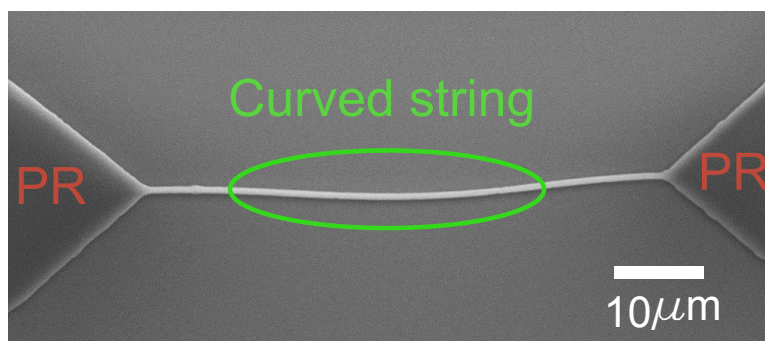


Figure 3.3: A patterned string onto HPR 504 on a silicon nitride substrate.

2 μm silicon dioxide sacrificial layer on a 0.5 mm silicon substrate, purchased from Rouge Valley Microdevices. Sacrificial thermal oxide layer is grown by wet process. The silicon nitride is deposited by low pressure chemical vapor deposition (LPCVD) technique at controlled temperature. This technique produces high internal stress which is ~ 0.8 GPa. Before starting the lithography process, I ensure that the wafer is clean. The standard process to clean a wafer is to use a piranha solution, a mixture of H_2SO_4 and H_2O_2 in a 3:1 ratio. This is a strong acid and extremely corrosive solution, hence it is important to be cautious while handling it. The wafer is dipped into the solution completely and kept submerged for at least 15 minutes, while the solution dissolves most of the organic impurities on the substrate. Then the wafer is cleaned by DI water thoroughly. Finally the wafer is dried in a spin rinse dryer. In this tool, the wafer is rinsed by DI water followed by heated N_2 flow. After cleaning, the wafer is ready for further processing.

In general, it is necessary to have an extra layer of hexamethyldisilazane (HMDS) for Si, SiO_2 and Si_3N_4 substrates which acts as an adhesion layer between the PR and the substrate. As seen in Fig. 3.3, without the HMDS layer, the string can become curved during optical lithography process due to loose bond of PR with the substrate. However, metallic layers, such as gold, can be sputtered onto silicon nitride substrate with chromium as an adhesion layer in between them. In this case there is no need for an extra HMDS layer on the top of metallic layer.

Once a wafer has been cleaned and coated with HMDS, it is held in a vacuum chuck on a spinner and 5–10 mL of a clean PR is poured into the center of the wafer. Two positive PRs called HPR 504, and HPR 506, have been used in this thesis. The PR thickness and uniformity depend on the rotation speed of the chuck. Fig. 3.4 shows the variation in the thickness of HPR 504 depending on the rotation speed of the chuck. The film thickness decreases rapidly with increasing rotation speed up to 3500 RPM, while the thickness varies slowly from 3500 to 5000 RPM. I find the optimal thickness is obtained for a rotation of 4000 RPM applied for 40 s. I also add a preliminary rotation step of 500 RPM for 10 s to spread the PR over the whole wafer. The wafer is then soft baked at 120 $^\circ\text{C}$ for 90 s on a hot plate to drive off any extra solvent. This recipe generates an approximately 1.25 μm uniform film thickness of HPR 504 photoresist on a clean wafer.

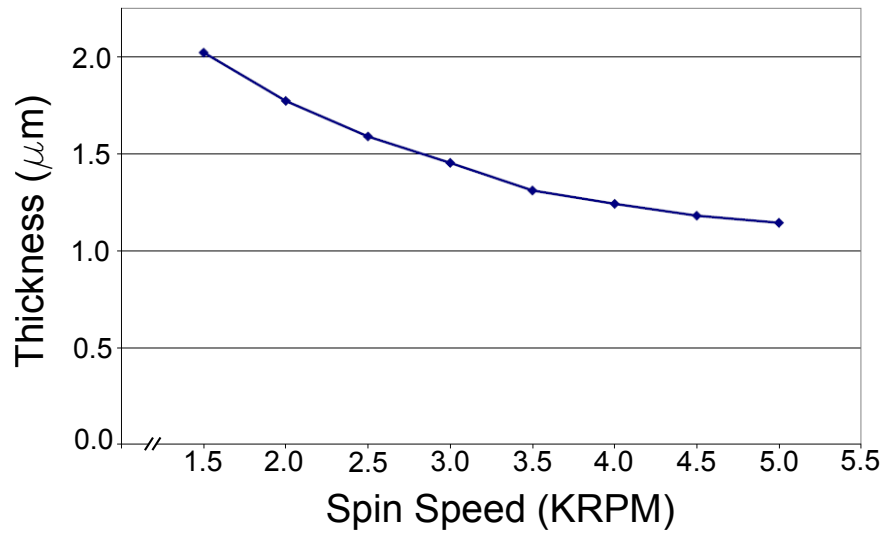


Figure 3.4: The variation of HPR 504 film thickness with respect to the spinner rotation speed. The data is taken from nanoFab SOP for HPR 504.

3.1.3 Sources

Sources used for optical lithography are monochromatic, intense, and short wavelength. Generally the I line (365 nm) of a mercury vapour bulb is used to produce ultraviolet (UV) rays [39]. It is also possible to use deep UV (DUV) rays using KrF (248 nm) or ArF (193 nm) sources, but these systems are expensive and generally commercial use only .

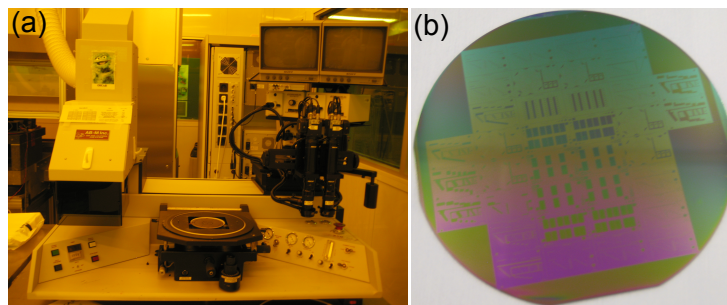


Figure 3.5: (a) Mask aligner with UV source, and (b) a patterned PR on a 100 mm diameter wafer

There are three different exposure methods: contact, proximity and projection. In the contact method, frequently used in research and development environments, both the mask and wafer are held in intimate contact by vacuum. Careful alignments are necessary for this method, so we use a split-field microscope for the alignment. In the proximity method, there is a small gap ($\sim 10\text{-}20\ \mu\text{m}$) between the mask and the wafer. The resolution ($\sim 2\ \mu\text{m}$) of this method is limited by diffraction and divergence. Finally, in the projection method, after UV illumination through the mask, a reduced image of the mask is focused onto the wafer by an optical system [40]. For my devices, I use the contact method with an optical mask alignment system in the NanoFab, which has a UV source, mask aligner, wafer chuck and mask holder as shown in Fig. 3.5(a).

Once mounted, the PR-coated wafer must be exposed to the UV source and then developed, to transfer the pattern to the PR layer. It is necessary to find the appropriate exposure time for a particular PR thickness to get accurate features. To this end, we use the relationship,

$$\text{Exposure time} = \frac{\text{Exposure energy}}{\text{Exposure factor}}, \quad (3.1)$$

where the unit of the exposure factor is mW/cm^2 . Since the exposure energy is constant for a known thickness of a specific PR, the exposure time (ET) depends on the exposure factor of the UV system. At a particular exposure factor, it is recommended to tune the ET to find the appropriate ET for proper exposure of that PR. After getting the proper ET at that exposure factor, the exposure energy can be easily calculated. Usually the exposure factor decreases over time for a UV system. Therefore, a new ET time can be easily determined from Eq. 3.1 since the exposure energy is constant for that UV system.

If the PR coated wafer is exposed longer than the appropriate ET then the PR is over exposed and corners of a feature on the PR are broken as shown in Fig. 3.6(a). Fig. 3.6(b) shows the opposite, when the wafer is exposed to UV less than the exact ET and the PR is underexposed. An underexposed PR will remain on the substrate even after developing for a long time. I found 1.8 s as the optimized ET for a $\sim 1.25\ \mu\text{m}$ thick HPR 504 photoresist film on a silicon nitride wafer for an exposure factor at $66.2\ \text{mW}/\text{cm}^2$. The exposed wafer is then developed in a PR developer called 354 for 19 s.

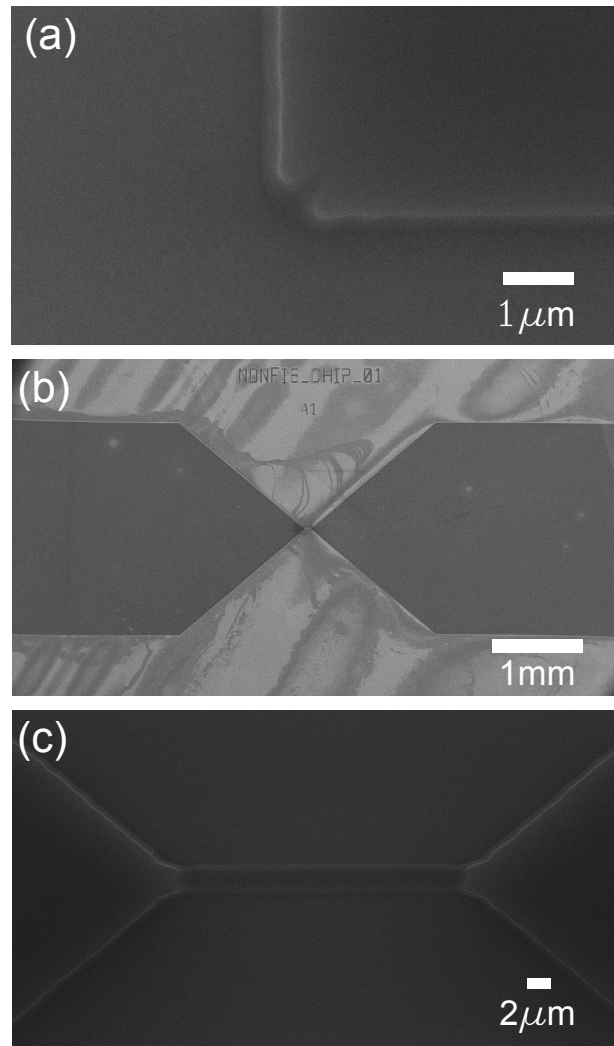


Figure 3.6: Patterned devices on PR with (a) over exposed, and (b) under exposed to UV sources. (c) A device with a trench in the middle.

Aside from the tuning the exposure time, it is also necessary to make a good contact between the hard mask and wafer. Specifically for a feature of small dimensions, good contact is crucial for a defect free device. Any small gap generates a ditch in the middle of the device due to the scattering of the light at the edge of the hard mask. As is seen Fig. 3.6(c), bad contact between the hard mask and wafer generates a trench in the middle of a 20 μm long, 2.5 μm wide beam. A device shown in Fig. 3.7 made with optimized parameters and with a good contact. Sharp

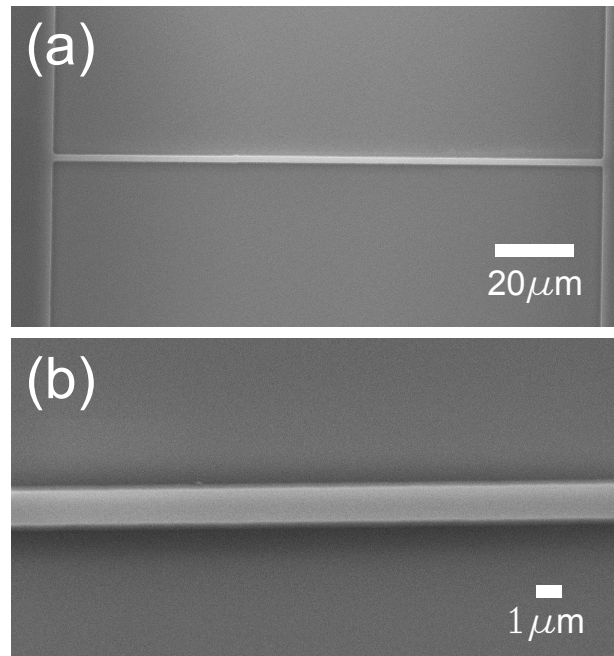


Figure 3.7: (a) A $125 \mu\text{m}$ long device patterned on PR, and (b) zoom in image of a portion of the string.

edges and no defects show the signature of a good device. This patterned PR, which exactly matches the pattern of the hard mask, will be used as a mask for subsequent processes.

At the end of the lithography process, the mask is cleaned using soap and deionized (DI) water to remove residual PR. Sometimes it is also necessary to clean the hard mask using cold piranha to remove hard residue of PR and other particles.

3.2 Electron beam lithography

The resolution of the optical lithography system in nanoFab is $\sim 1.5 \mu\text{m}$. Therefore it is necessary to replace the optical lithography process to make a device with dimensions less than $1 \mu\text{m}$. The electron beam lithography (EBL) system is one of the alternative instruments and EBL is mostly used in nanomechanics community. In our nanoFab, we have a 30 kV EBL system named Raith-two EBL. The basic difference with optical lithography is that there is no hard mask needed for EBL

processing, the pattern is designed in a designated software. In addition, the EBL pattern is written by electron beams which is not limited by diffraction—in contrast to the optical lithography system.

There are both positive and negative EBL resists similar to optical lithography system. These resists are sensitive to the exposure of electron beam. The positive resist is washed away after exposure where as the negative resist is stayed after exposure. The most commonly available positive EBL resists are ZEP 520A and PMMA. However, the ZEP is used mostly for this thesis. After thoroughly cleaning of the substrate, ZEP is spun on the substrate then the chip is baked at 180 degree Celsius for 20 minutes. Then the chip is mounted onto the EBL substrate holder and pumped down. The very beginning task is to find the proper area dose for a particular feature size with a particular EBL resist. It is worth mentioning that the area dose also depends on the aperture and voltage of the EBL system. To make small features in ZEP, 30 kV and 10 μm aperture are used in this thesis. The proper area dose for this resist is found to be $\sim 310 \mu\text{C}/\text{cm}^2$. However it will take long time to write a relatively large feature with these parameters which might not be suitable for a user. In that case, it is easier to use large aperture (for example 60 or 120 μm apertures) which will produce high current. The current will be at least a couple of orders of magnitude higher than before and it will help to write big features in relatively less time.

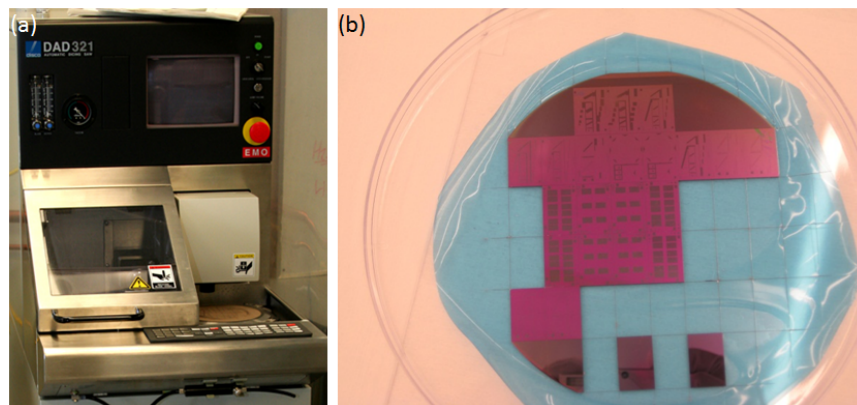


Figure 3.8: (a) Dicing saw (Disco DAD 321) in the NanoFab, and (b) a diced wafer using this dicing saw.

After writing a feature in EBL system, the chip is developed in a developer. ZED

N-50 is used as a developer for the EBL resist ZEP. The development process can be done either in room temperature or at lower temperature (-10 degree Celcius). One would prefer to process the cold development for a small feature with nice vertical side walls. However, the area dose is almost three times higher for the cold development compared to the room temperature development.

3.3 Dicing

Dicing is an important step in the fabrication process. My experimental setup will not fit the entire wafer so we need to dice the wafer into suitable small pieces.

The wafer can be diced either immediately after the lithography process or before the releasing step. I dice my wafer into small pieces with dimensions of 10 mm by 15 mm each using a dicing saw (Disco DAD 321) (Fig. 3.8 (a)) after the lithography process. Fig. 3.8 (b) shows a diced wafer; a few of the resulting chips have been used for the following steps.

3.4 Etching

After transferring a pattern from the hard mask to the PR layer we need to transfer this pattern to the underlying material. This can be done through either a lift-off method or an etching technique. We use the latter technique to transfer patterns on photolithographically processed chips. There are two types of etching: dry (plasma) etching and wet etching. We briefly discuss each process here.

3.4.1 Dry (plasma) etch

Dry etching involves etching in a low pressure plasma and is carried out in a vacuum environment. The most common type of plasma etch is a reactive ion etch (RIE) which uses both reactive and non-reactive gases. Both gases can cause sputter damage and ablate material from the sample surface, so the plasma voltage is kept low enough to minimize the ablation process. Then, a radio frequency (RF) voltage is applied across a pair of parallel electrodes to drive the plasma. The sample, sitting on an electrode, is exposed to the accelerated ions when the voltage of that

electrode is below the plasma voltage. Intermediate volatile species are formed due to a chemical reaction between ionized gas and sample surface which are then desorbed or ablated by low voltage impact ions. This RIE process yields highly anisotropic etching at low pressure [40]. We can control the RIE by pressure, flow rate of gases and radio frequency (RF) power. Moreover, the etch rate is different for each PR type. If the PR layer is too thin, then RIE can etch the PR and start to etch the substrate resulting a bad quality device. Hence, it is better to use a thick layer of PR as a mask to protect the underlying material. A profiler can be used to measure the remaining PR thickness to ensure that the devices were protected by PR. Proceeding with a single chip instead of the whole wafer facilitates a cost effective process of determining a suitable recipe.

I have used the RIE (Trion) machine in the nanoFab to etch high stress silicon nitride. I optimized the process, and I have found the following optimal parameters: pressure 75 millitorr, RF power 300 W, and 45 sccm of SF₆. The high power and low pressure generates straight device side walls. This recipe produces ~ 4 nm/s etch rate of silicon nitride substrate and ~ 6.5 nm/s etch rate of HPR 504 PR. According to this etch rate 63 s is enough to etch 250 nm thick silicon nitride. But to be assured of a complete silicon nitride etch, we usually run a 90 s long etch time. Since the HPR 504 thickness is ~ 1.25 μm so it still works as protective layer on the top of the silicon nitride substrate.

However, this recipe does not work on a Au and Cr coated silicon nitride wafer, where Cr has been used as an adhesive layer between Au and a silicon nitride wafer. After wet etching the Au and Cr, the same RIE recipe was attempted but it failed to etch the silicon nitride as shown in Fig. 3.9(a). It was noticed that the color of silicon nitride changed, which was visible optically even after completely etching the Au and Cr layers. This observation confirms that Cr undergoes a chemical reaction with the high stress silicon nitride to make a thin film over the surface of the substrate. Further investigation could be done to determine the chemical properties of that surface. After a rigorous tuning of RIE parameters, it is found that the same recipe starts to work with a presence even a small amount of O₂ (5 sccm) which is visible in Fig. 3.9(b). But the edge of the device is not that great with only a small amount of O₂. Eventually the optimized parameters are found as the following: pressure 75 m Torr, RF power 300 W, 45 sccm of SF₆, 60 sccm of O₂. It was also noticed that adding O₂ enhances the etch rate of the PR. So

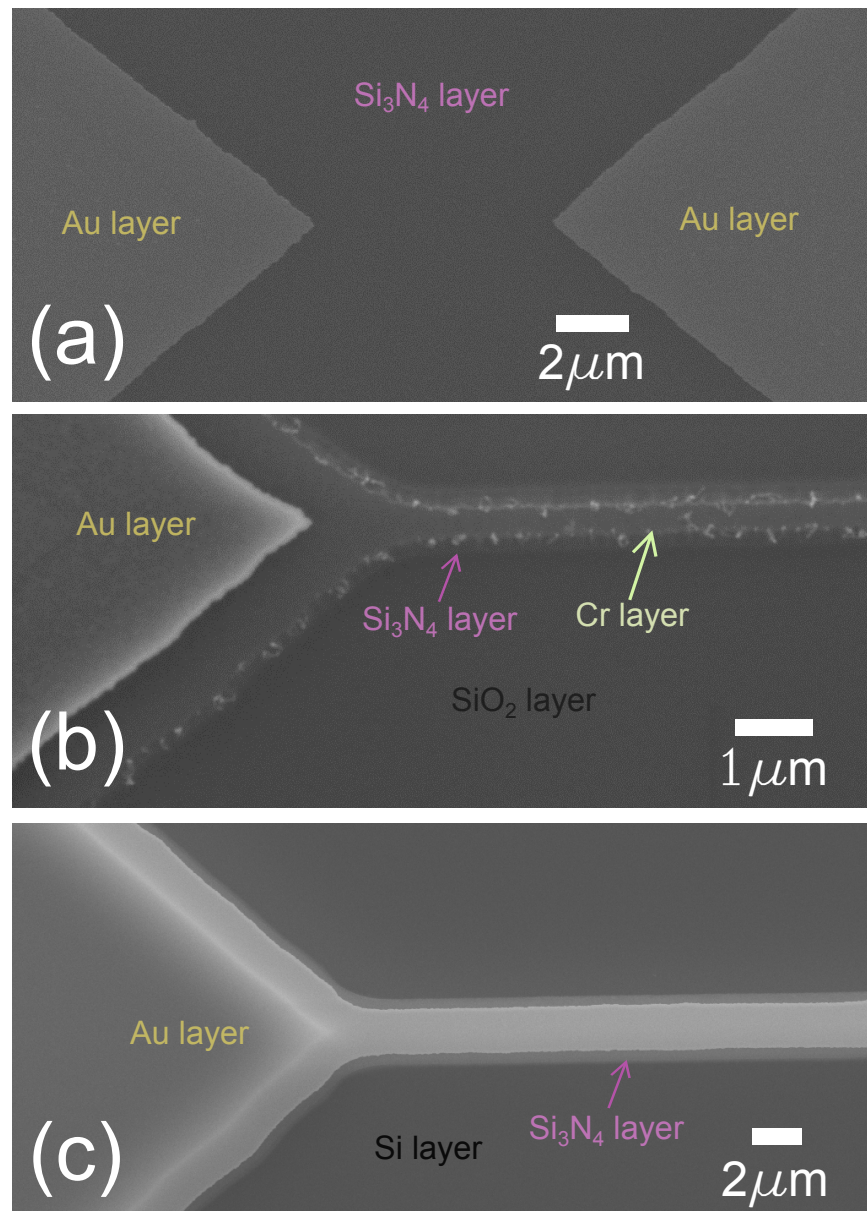


Figure 3.9: RIE processed on Au and Cr coated silicon nitride chips with (a) no O₂, (b) with 5 sccm of O₂, and (c) with 60 sccm of O₂.

I used a thick PR (2.5 μm) instead of a thin PR (1.25 μm) for a long etch time used here. A gold and silicon nitride bi-layer device processed with this recipe is shown in Fig. 3.9(c) after PR removal. Acetone and isopropyl alcohol (IPA) have

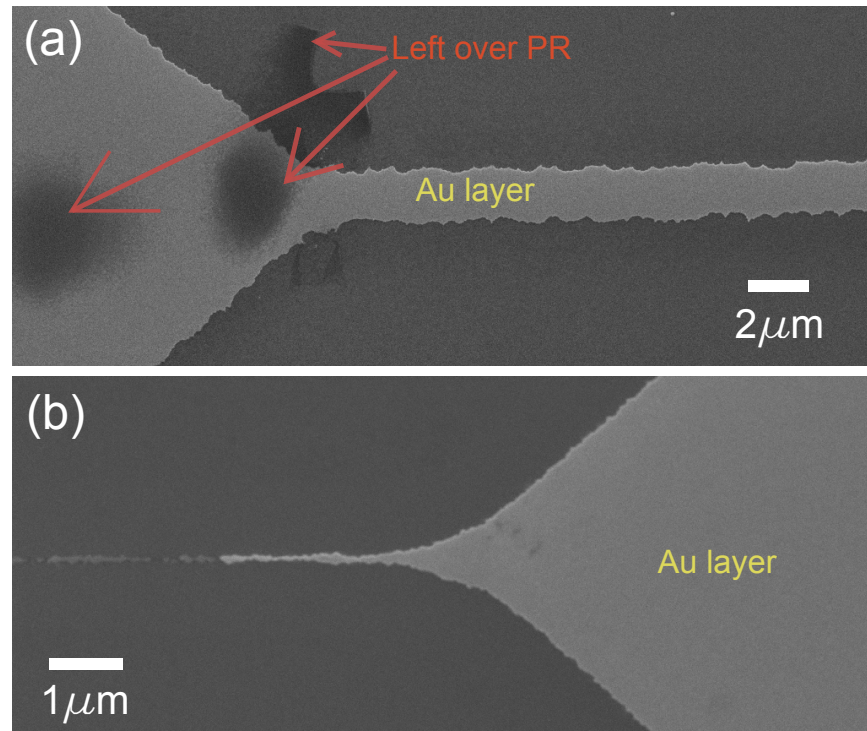


Figure 3.10: (a) A device after the gold etch, and (b) uncontrolled gold etching of a device.

been used to remove remaining PR after the RIE process. Further dry etching can be done with different recipe (400 millitorr pressure, 100% O₂ and 33 % RF power) with different instrument called RIE (μ Etch) if any PR residue is left over. It is also possible to do a piranha cleaning to remove any remaining PR residues. If there is a metallic layer on the device, then we must have to check whether this metal is etched by piranha solution or not. For example, aluminum (Al) is etched in piranha solution.

3.4.2 Wet etching

Wet etching is performed by dipping our wafers or chips into aqueous acids or bases which preferentially removes the exposed material. Wet etch, in general, is highly selective so we must use different etchants to remove different materials. Furthermore, wet etching is usually isotropic and leaves an undercut.

Once the bare silicon nitride has been patterned, the chip is ready to remove the underlying sacrificial layer of SiO_2 by wet etch immediately after the RIE step. The order of the wet etch and dry etch depends on the process flow and device materials involved in the fabrication process. For a metal coated wafer (I have gold and chromium on the top of silicon nitride wafer, here chromium works as an adhesive layer), it is necessary to do the wet etch of the metal before the RIE process. Then another wet etch is followed by the RIE step to remove sacrificial layer of SiO_2 .

The gold etchant used in nanoFab is a solution of potassium iodide, iodine and water, and has a etch rate of 5.3 nm/s, quite fast for a thin gold layer. This aggressive chemical reaction left rough edges after the etch, as seen in Fig. 3.10(a). I also noticed that sometimes it is not possible to control the etch time properly due to fast etch rate and as a result, most of the Au is etched away as shown in Fig. 3.10(b). So it is better to reduce the etch rate to get better result for a thin Au layer. To this end, I have made a solution of the existing Au etchant and DI water in a 1:3 ratio. This generates a slower etch rate of ~ 2 nm/s, which produces relatively smooth gold edges as seen in Fig. 3.9(c). It is worth noting that the etch rate of this solution degrades rapidly over time. Therefore, it is recommended to replace the solution every month. Similarly, a Cr etchant used in the nanoFab is a mixture of ceric ammonium nitrate, nitric acid and water. The etch rate of this etchant is reduced by adding DI water in a ratio of 1:1. This new solution has a etch rate of ~ 1.5 nm/s, which allows better control while etching a thin layer of Cr.

I use a buffered oxide etch (BOE), which is a mixture of ammonium fluoride and hydrofluoric acid, which etches the sacrificial SiO_2 layer to release my strings. The BOE used in the NanoFab has a etching rate of 55 nm/s, which translates to approximately 38 minutes for the removal of a 2 μm thick silicon dioxide layer. We need to take extra care when working with this type of material on a drop/wet deck since BOE is extremely harmful.

Drying the chip in air risks causing the nanostring to stick to the substrate, so I use either a solvent to release the device or a critical point dryer. I prepare five different solutions of pentane and IPA for solvent release: 100 % IPA, 75% IPA + 25% pentane, 50% IPA + 50% pentane, 25% IPA + 75% pentane and 100% pentane. The wafer/chip is dipped into each solution for 40 sec which starts with 100% IPA and ends with 100% pentane. A released device is shown in Fig. 3.11.

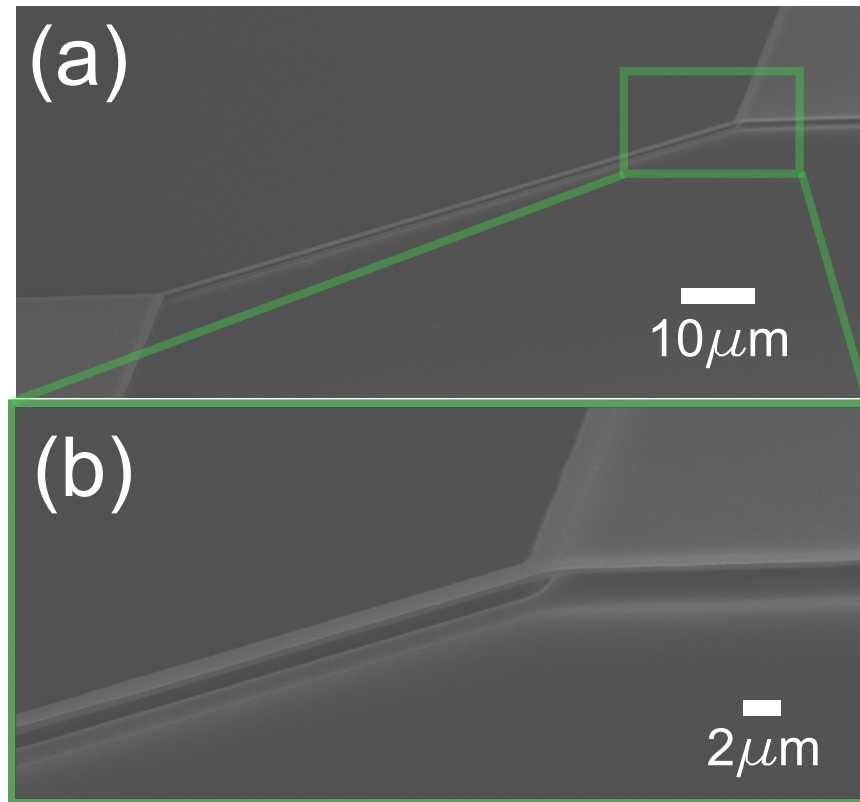


Figure 3.11: (a) A $210\mu\text{m}$ long released string, and (b) zoom in image of a portion of the string and an anchor pad .

3.5 Characterization

Characterizing the various steps involved in the nanofabrication process is essential. In this section, various instruments are described which are used in this thesis.

3.5.1 Alpha-step IQ

In general, a profilometer is used to measure surface roughness, profile, and step height at the resolution of sub-nanometer. I used a profilometer named Alpha-Step IQ (as shown in Fig. 3.12(a)) in the nanoFab to measure the thickness of HPR 504 and HPR 506. This instrument can produce two-dimensional surface topography with a sub-angstrom step height using diamond stylus of the radius $6\mu\text{m}$. However,

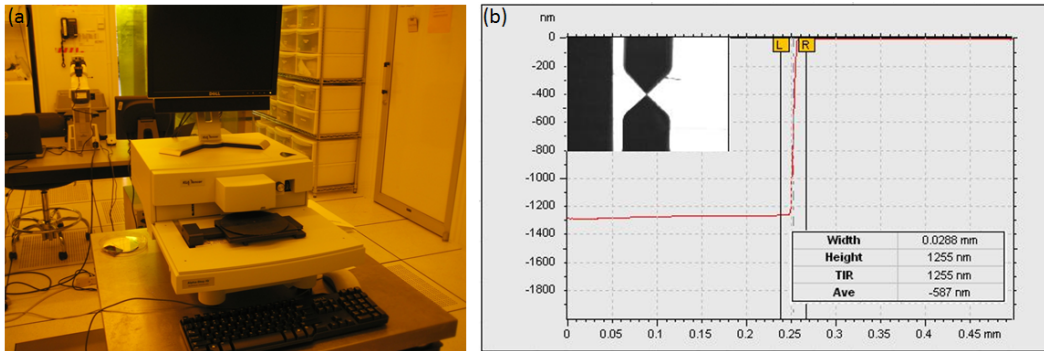


Figure 3.12: (a) A contact profilometer in the nanoFab, and (b) step height of HPR 504 measured by this profilometer.

this is a contact profilometer where the stylus scans physically over the surface of a sample. Fig. 3.12(b) shows measurement of the thickness of HPR 504 photoresist on a sample by this instrument.

3.5.2 Optical microscopes

Optical microscopes in the clean room play an important role for successful fabrication. There are four optical microscopes inside the nanoFab clean room. I mostly use the Leica INM-100, which has up to 100x objectives. It is an important habit to always inspect before and after each fabrication step, especially in the optical lithography process. If any patterned feature is unsatisfactory then it can be re-done in lithography process. Moreover, there is an optical microscope in our lab as shown in Fig. 3.13(a). We can install CCD Camera on this optical microscope which gives us opportunity to capture optical images of my devices. Optical imaging is also useful for those devices which can not be processed in an electronic microscope system. For example, after deposition of explosive molecules on a resonator, it is convenient to take images under optical microscope right before mounting in the experimental chamber. Fig. 3.13(b) shows an optical image which is taken by the optical microscope stationed in our lab.

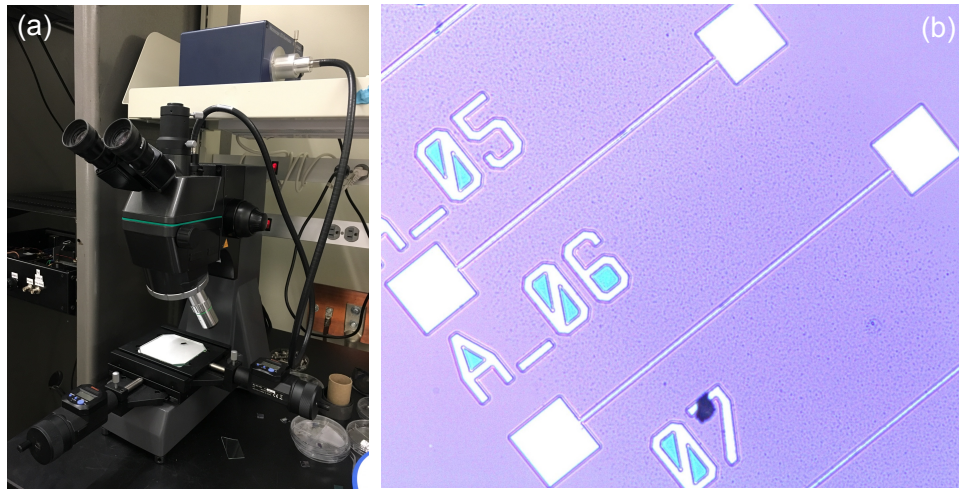


Figure 3.13: (a) An optical microscope in our lab, and (b) an image taken by this microscope after the deposition of explosive molecules called RDX.

3.5.3 Scanning electron microscope

Imaging the device is an important diagnostic step, but optical imaging is limited by diffraction to a resolution of ~ 200 nm. Therefore, I instead use a scanning electron microscope (SEM) to image my devices. SEM is a type of electron microscope which use a focused electron beam to produce images of a sample. The electron beam loses energy when it interacts with the atoms in a sample. There are varieties of ways to radiate this lost energy such as heat, low-energy secondary electrons, high-energy backscattered electrons, and X-ray emission. All of these signals provide information about the surface topography and composition of the sample. The most common type of SEM imaging is to construct an image from the secondary electron beam emitted from the sample.

Fig. 3.14(a) shows one of the scanning electron microscopes in the nanoFab called the Zeiss EVO MA10. It has a thermal emission firing unit with 300 V to 30 kV accelerating voltage. It also has three axes of translational movement, along with rotational and tilt stage control. The detectors of this SEM are solid state secondary electron detectors and back-scattered electron detectors.

It is recommended to take an image after each step of the fabrication process to ensure the quality of the device. SEM is the best way to take images of a device, as

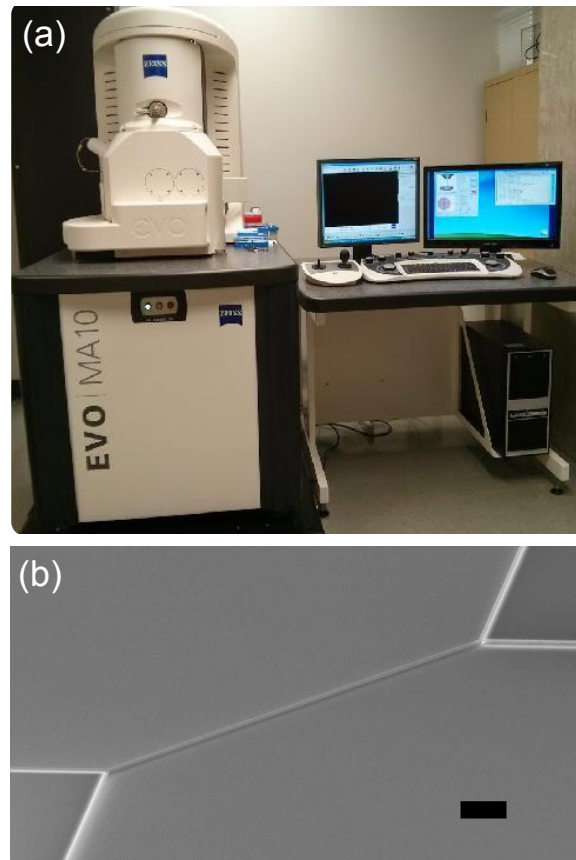


Figure 3.14: (a) A scanning electron microscope in the nanoFab and (b) an SEM image of a $215 \mu\text{m}$ long silicon nitride nanostring. The scale bar is equivalent to $20 \mu\text{m}$ long.

if provides a detailed topography of a sample. We can thus see whether the device has been released or stuck or if there are any defects. Fig. 3.14(b) shows a SEM image of a released nanostring after the full fabrication process.

CHAPTER 4

Experimental setup

Apart from the device fabrication process, the device characterization and application is performed in our lab. Therefore, we built an experimental set-up suitable for my devices. The set-up is based on optical interference technique as the schematic shown in Fig. 4.1. A HeNe laser is focused on a device. A portion reflects from the string and the rest reflects from the substrate. These two beams interfere with each other and this interferometric optical signal is transferred into a voltage signal by a detector. The devices are mounted onto a piezoelectric buzzer, which can provide mechanical actuation when excited by a lock-in amplifier (Zurich Instruments HF2LI). Interferometric detection can be performed with or without a voltage applied to the piezobuzzer. The experiment is housed in a vacuum chamber which has a glass window.

4.1 Detection laser and collimator

It is very important to pick a detection laser for our system that will work properly. Most of my devices have silicon nitride layer on top of a silicon substrate. The silicon nitride is mostly transparent to the red laser. Therefore, a HeNe laser of 632.8 nm is chosen for our experimental setup as shown in Fig. 4.2(a). A little portion of red light (11 %) reflects from this layer and rest of the light reflects from the silicon surface interfere to each other and provide the required signals. The maximum output power of this laser source is 5 mW. However, the laser is coupled through a single mode FC/APC connectors fiber optic patch cable to guide it to our devices.

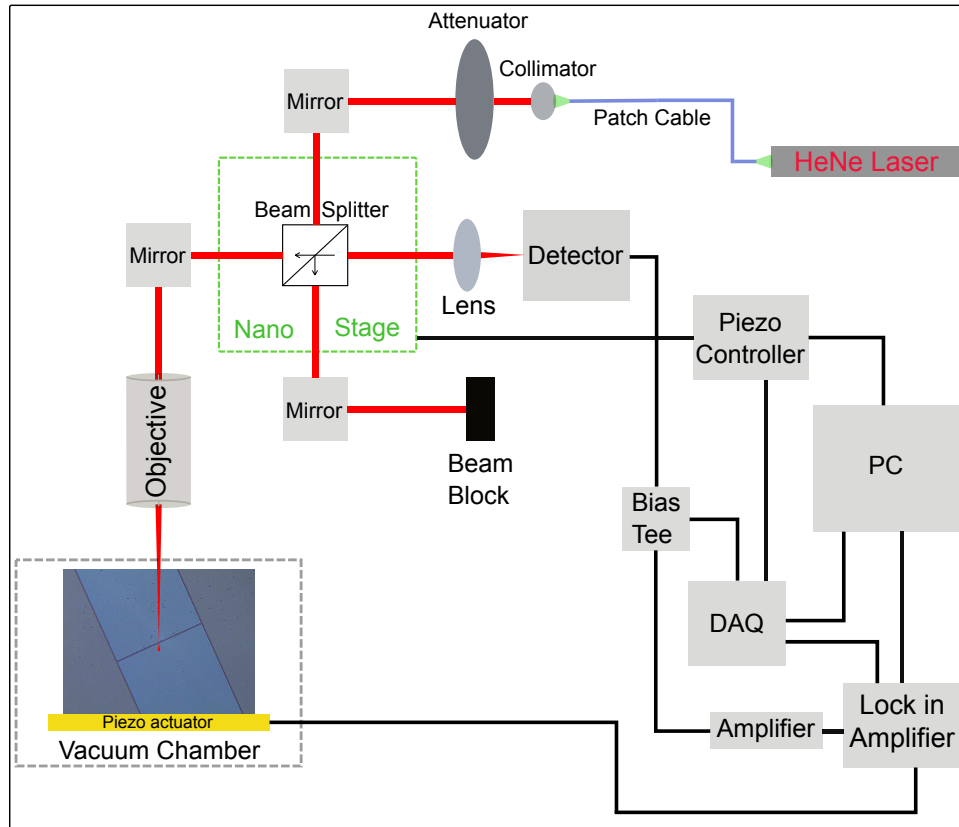


Figure 4.1: Schematic of our experimental setup with major components. Here, DAQ stands for data acquisition cards and PC stands for a computer.

It is noticed that the maximum power coming from the output of the patch cable is approximately 1.5 mW. This power is more than enough for the experiments done in this thesis. The most of the power loss is observed at the connection between the laser head and the patch cable due to the coupling. In general, light diverges from a source as it travels away from the source and it is observed for our red laser as well. But it is convenient to have a collimated light rays in our experimental set-up. Therefore, the output of the patch cable is attached to a collimator which makes the light rays parallel to each other. A convex lens is an example of a simple collimator as shown in Fig. 4.2(b). Divergent light rays are coming from a point source and incident on a convex lens. The light rays become parallel to each other after passing through the convex lens due to the refraction of light.

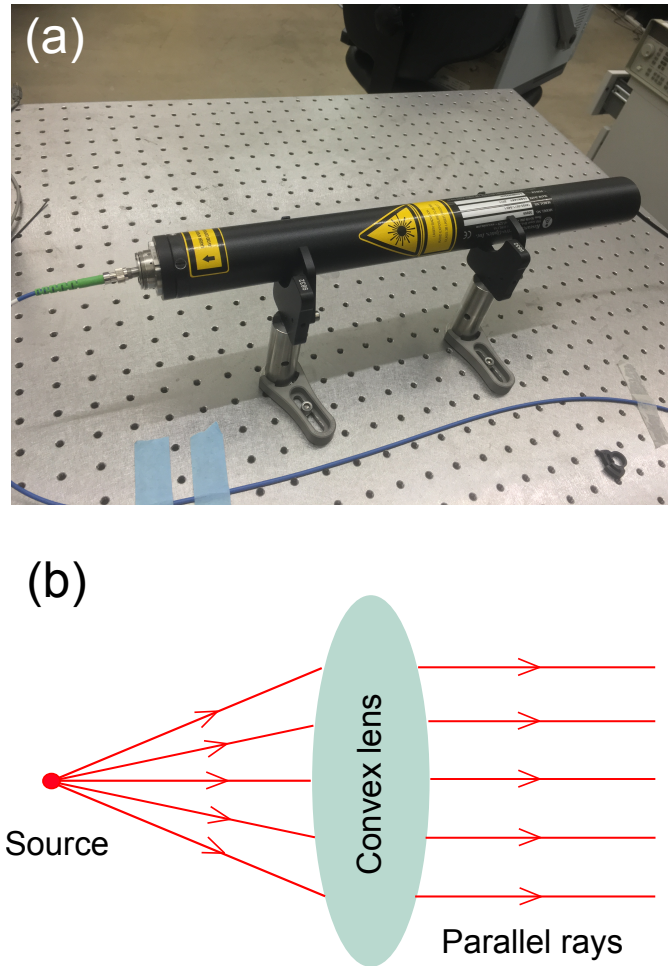


Figure 4.2: (a) A HeNe laser head, and (b) laser controller.

4.2 Attenuator

It is necessary to control the laser power of an experimental set-up. Our set-up can be used for different types of devices such as silicon nitride nanostring and gold coated silicon nitride nanostring. However the absorption coefficients are different for these devices for a particular detection laser. Therefore an attenuator is introduced in this system to reduce the power label of the red laser as shown in 4.3. This attenuator works based on the absorption of light. This is coated with a special film with varying thickness which absorbs light of different intensity. Therefore, it



Figure 4.3: An optical attenuator.

is set to an angular position such that it passes the desired optical power such as low optical power ($\approx 13 \mu\text{W}$) is expected for a gold coated string to minimize the laser heating effect.

4.3 Beam splitter and nano-stage

One of the major components of this set-up is a beam splitter. A partially reflected mirror can be used as a beam splitter. When light is incident on a beam splitter, one part of the light reflects at 90 degree and remaining part passes through the beam splitter. The splitting ratio depends on the reflection coating. In our experiment, we have used a 50:50 beam splitter, shown in Fig. 4.4, which divides the light into two equal portions. Mounting the splitter is important as indicated in Fig. 4.1 to get the light in the desired direction.

Another major part of our set-up is a positioning-stage on which all optical accessories are mounted. This is a 3-axis flexure stage from thorlab that has 4 mm travel capability for all x, y, and z direction. The closed-loop piezo control of the stage provides a positioning resolution of less than 20 nm. This provides us the

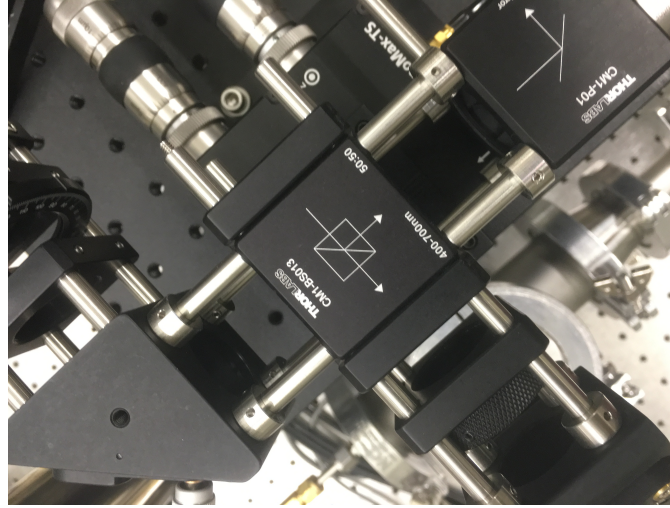


Figure 4.4: A 50:50 beam splitter.

opportunity to do laser alignment with the objective and the photo-detector with a better accuracy. Since the whole system is moving with the stage so no disturbance occurred for the internal alignment.

4.4 Objective

The half reflected at 90 degree angle from the beam splitter, passes through an optical objective to focus on our device. Other half passes straight through the beam splitter and a beam blocker is placed at the end to stop that light. The objective has a long working distance, which is 17 mm. This distance is preferable to have a good clearance in between the objective and the vacuum chamber. There are numerous objectives with different zooming factors. However, there is no major difference in signal amplitudes acquired by a 20x, 50x and 100x objectives as discussed in Appendix C. We mostly use a 50x objective in our system to get better view of our small devices. For the initial laser alignment to the device, it is convenient to see the image on a white paper placed in front of the convex lens (Fig. 4.1). This is the another benefit to use the red laser instead of any near IR laser or near UV laser. It provides us the opportunity to see the laser light and hence alignment with our string. Therefore, the incident collimated light on the lens is focused at the pinhole of the photodetector by this convex lens. However, fine tuning is performed



Figure 4.5: An optical photo-detector.

by another step to get optimized signal from the system.

Assuming the red laser incident on the string, then a small part reflected from the string and rest of the light reflected from the substrate. Then they interfere and this light signal is again collected through the objective. Now when the light is going back to the beam splitter, it permits to pass half of that returned light through it. A convex lens is used to converge these collimated light rays to a single point and then a photodetector is mounted at that place to receive maximum light rays.

4.5 Detection and data acquisition

The photo-detector turns the optical signal into an electrical signal. This electrical signal is composed of both DC and AC signals. Therefore, it is essential to separate them before sending to the network analyzer. A bias tee is used in this case to separate them from each other as shown in Fig. 4.1. The AC signal is transferred to a pre-amplifier to increase the signal amplitude and attached to the input of a network analyzer. In our set-up, a Zurich high frequency lock-in amplifier is used as a network analyzer in this case. The output of the network analyzer is connected to a piezobuzzer underneath the device. This shakes the device and when it matches the frequency of the device, it amplifies the signal amplitudes which is easily observable in spectrum analyzer.

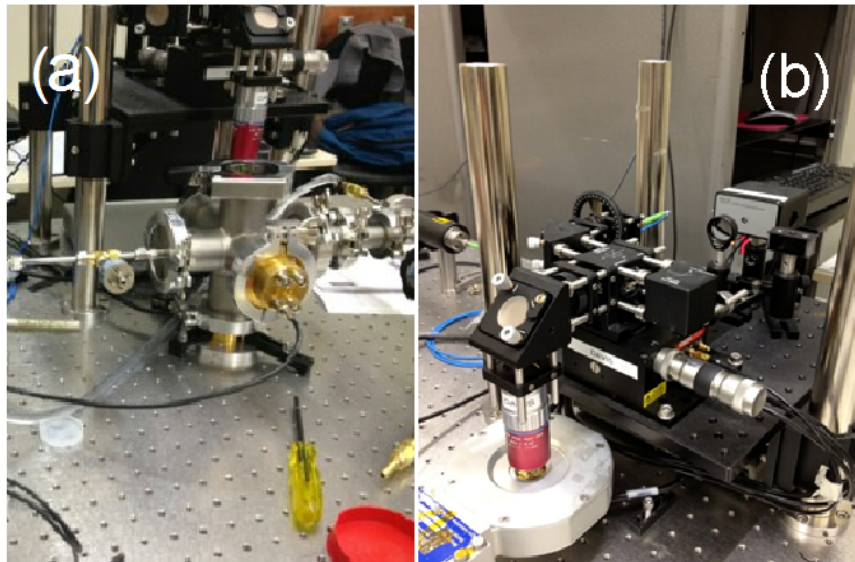


Figure 4.6: Photograph of our (a) home made vacuum chamber, and (c) cryogenic vacuum chamber.

4.6 Vacuum chamber

We have performed our initial experiment in a cryogenic vacuum chamber, shown in Fig. 4.6 (b). This chamber is therefore capable to cool down its temperature. There is also a heater in the chamber to control its temperature. It is not easy to flow gas (such as IPA, methanol) through this chamber. Moreover it is difficult to clean the chamber after gas flow. Therefore we have made a new vacuum chamber with help of one of our summer students Alberto Palomino as shown in Fig. 4.6(a). This chamber also has a glass window to detect optical signals but it has more electronic feed throughs as compared to the previous one. In addition, this chamber can be cleaned easily after flowing gas such as acetone through the chamber.

CHAPTER 5

Dissipation mechanisms in high stress silicon nitride nanostrings ¹

Silicon nitride nanostrings have generated a great deal of excitement in the nanomechanics community for their extremely high values of mechanical Q . These devices can be used as sensors in various applications such as mass sensing [1], temperature sensing [41], and optomechanics [42, 43, 44]. In this Chapter, we demonstrate thermomechanically limited detection of up to six modes of high stress silicon nitride nanostrings. We also present a set of devices in which all harmonics fall upon a single curve of calibrated peak displacement versus frequency.

5.1 Dissipation in high stress materials

The large internal stress of silicon nitride devices produces large stored elastic energy and correspondingly large mechanical Q [11]. In addition to causing the high Q , the tension compels the devices to behave like strings rather than doubly clamped beam. The harmonics of a string are at integer multiples of the fundamental frequency [12] and the mode frequency does not depend on the width or the thickness of the string; it only depends on the length. This is in contrast to low-stress silicon nitride devices which behave like doubly clamped beams and possess more complicated harmonics [45, 46]. In addition, high Q s are revealed in nanostrings of various

¹A version of this chapter has been published in Applied Physics Letters. A. Suhel *et al.*, *Appl. Phys. Lett.* **100**, 173111 (2012)

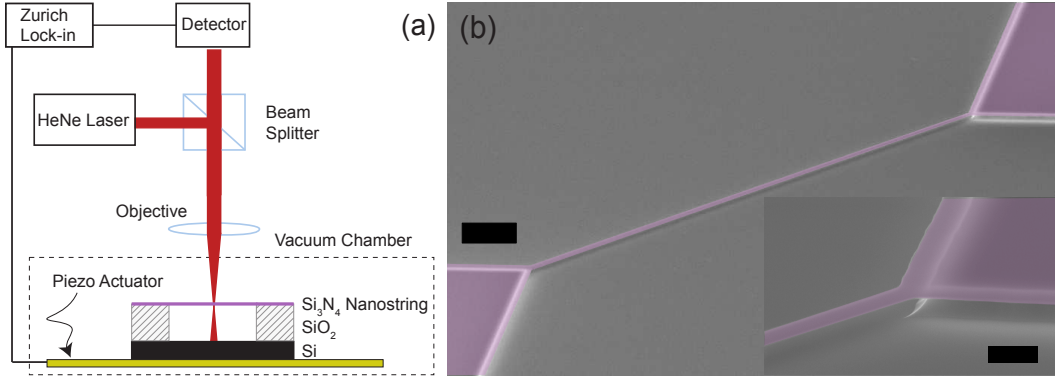


Figure 5.1: (a) Schematic of experimental setup and (b) Scanning electron micrographs with false color of the 215 μm long silicon nitride nanostring, with scale bars in the main image and inset of length 20 μm and 3 μm , respectively

materials which are under tension, including the polymer SU-8 [4], aluminum [5, 41], and AuPd [6]. This observation strongly suggests that the high Q is not a special material property of the silicon nitride itself but rather the tension.

Nanostrings can be calibrated accurately [47] and hence they are good candidates for sensing applications [48]. Here, the absolute displacement of a nanostring is determined from measurements of its thermal fluctuation. Since the fundamental mode has the largest amplitude, this procedure is often restricted to this mode. However, we are able to resolve the thermomechanical motion of up to six harmonics for our longest strings. This is only possible because of their high Q s. This multimode calibration reveals important information about the dominant dissipation processes in nanostrings.

5.2 Experiment details to detect resonance frequencies of high stress silicon nitride nanostrings

Silicon nitride nanostrings are fabricated from stoichiometric silicon nitride deposited onto silicon dioxide on a silicon handle using LPCVD. Standard optical lithography processes have been performed followed by RIE. The devices are released by a buffered oxide etch of the 2 μm thick silicon dioxide layer. Details of a

device fabrication process are described in the chapter 3. The released devices are shown in Fig. 5.1(b). These devices are mounted onto a piezobuzzer inside a vacuum chamber. The piezobuzzer can provide mechanical actuation when excited by the lock-in amplifier (Zurich Instruments HF2LI). The vacuum chamber is pumped down to a high vacuum of $\sim 2 \times 10^{-6}$ torr which is sufficiently low to eliminate pressure related damping [9]. It is also worthy to mention that we expect to observe the effect of free molecular flow damping at around 1 mTorr for the width of our device [9]. The displacement of the nanostring is measured via optical interferometric technique as shown in Fig. 5.1(a). Details of this setup are described in chapter 4. The maximum optical power impinging on the string is ~ 100 μ W. It is shown in Appendix A that there is no resonance frequency shift as a function of optical power. Interferometric detection can be performed with or without a voltage applied to the piezo-buzzer. Signal amplitudes (V_{rms}) of a 105 μ m long string are shown in Fig. 5.2(a) at different drives applied to the piezo. The device response shows linear Lorentzian shapes in linear regime up to a 1 mV drive. Beyond this drive it starts to show a little nonlinearity which is visible at 3 mV and 5 mV drives. The resonance frequency in the linear regime does not depends on actuation drives. This is also confirmed from the phase response of the device as shown in Fig. 5.2(b). Phase shifts for all drives overlap on top of each other, except for those drives which make the signals nonlinear.

In this section, we are interested in showing proper calibration of thermomechanical motion of the devices to reveal important information about their dissipation mechanisms. To perform the measurement of thermomechanical motion, we remove the voltage applied to the piezo. In this case, the HF2LI acts as a spectrum analyzer with a user-controlled measurement bandwidth. We chose the bandwidth of 1 Hz to measure the high Q s of our devices. This bandwidth is identified by verifying that the Q measured via thermomechanical actuation is consistent with the driven Q , as well as with a ringdown measurement versus time as shown in Appendix B.

5.3 Theoretical framework for dissipation mechanism

Let us consider a string of a natural length L . In a simple model, the vertical displacement of the string is described by $z(x, t)$, which is a function of the horizontal position x along the string and the time t , with boundary conditions $z(0, t) =$

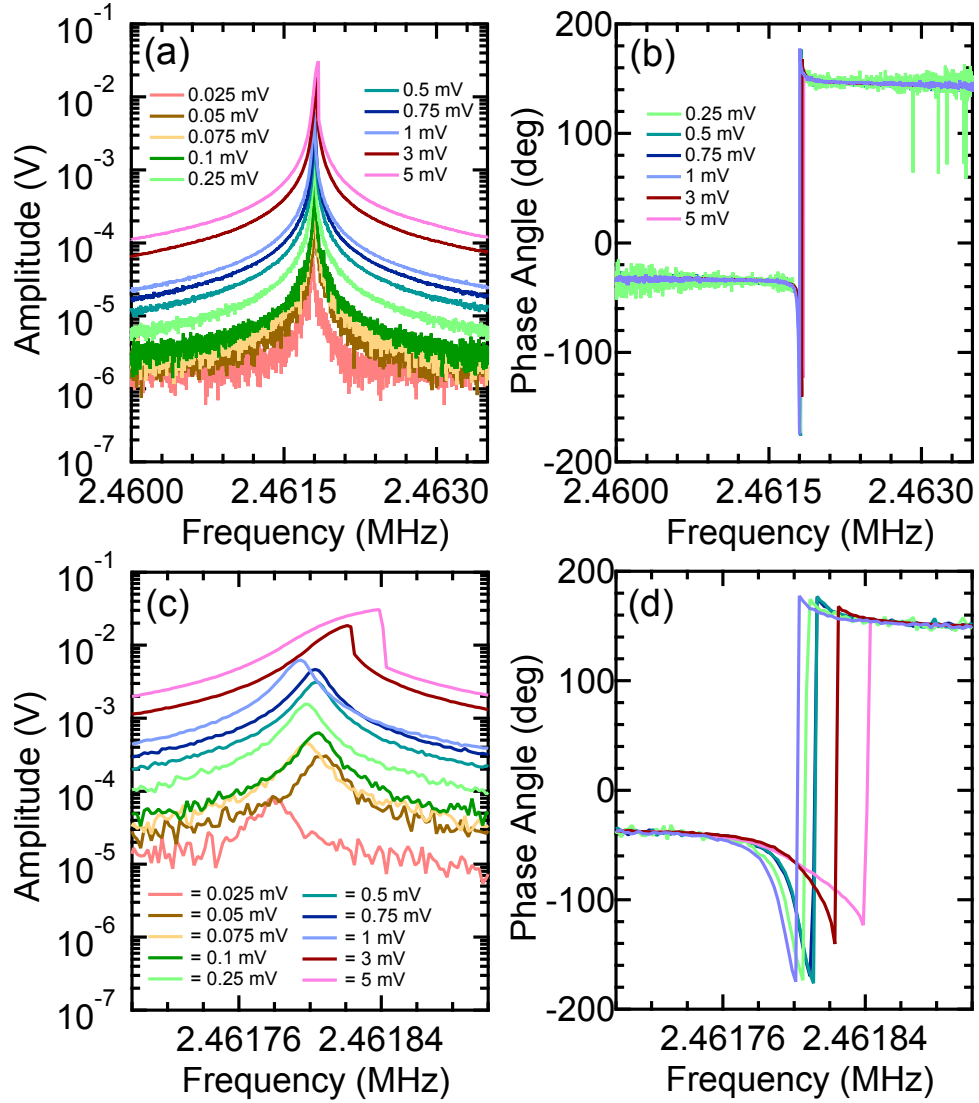


Figure 5.2: (a) Voltage signal of a 105 μm long string for various drive voltages. (b) Phase response of the string at corresponding drive voltage. Data are not included for low drive voltages 0.025, 0.05, 0.075 and 0.1 mV. (c) Zoomed in graph, to show how the frequency shifts to the higher value at non linear regime, and (d) zoomed in graph to show the corresponding phase shifts.

$z(L, t) = 0$. In the linear regime, the length of the string deviates from L by an amount $\int_0^L dx z_x^2$, (here $z_x = \partial z(x, t)/\partial x$ denotes the partial derivative). The silicon

nitride string has a very large internal stress σ , such that any stretch in the string produces a strong restoring force. Hence the modified wave equation for the string can be written as $\rho z_{tt} = \sigma z_{xx} - D[z(x,t)]$, where the functional D encodes the various dissipative processes of the device.

The motion of the string can be decomposed into its normal modes as

$$z(x,t) = \sum_n a_n(t) \sin\left(\frac{n\pi x}{L}\right), \quad (5.1)$$

where n is the mode number. The first six mode shapes are shown in Fig. 5.3. In linear regime, each mode acts as a damped harmonic oscillator and is governed by

$$m \frac{d^2 a_n}{dt^2} + \gamma_n \frac{da_n}{dt} + m\omega_n^2 a_n = f_n(t). \quad (5.2)$$

Here, m , ω_n , γ_n , and $f_n(t)$ are the geometric mass, the angular frequency, the damping coefficient and the forcing term of the nanostring, respectively, with the damping coefficient defined as $\gamma_n = m\omega_n/Q_n$. The resonance frequencies of the nanostring are given by

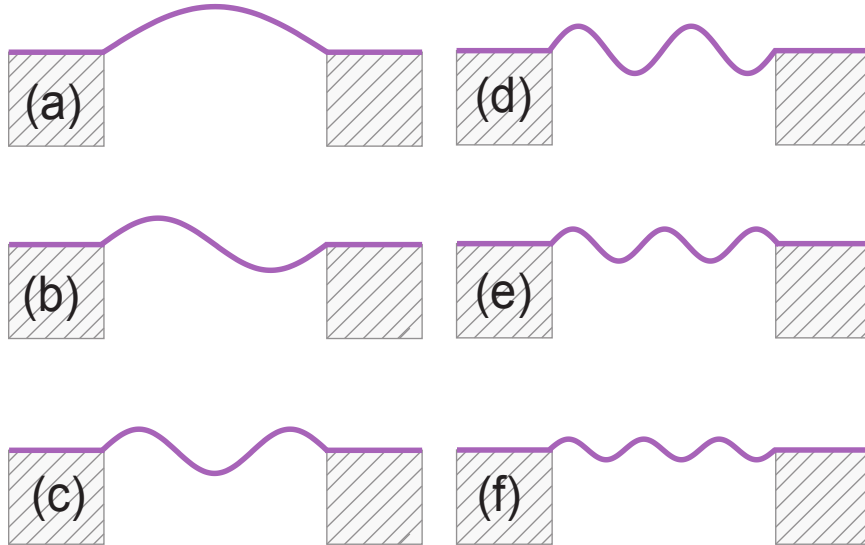


Figure 5.3: Cartoons showing the mode shapes of the first six harmonics of a nanostring.

$$f_n = \frac{\omega_n}{2\pi} = \frac{n}{2L} \sqrt{\frac{\sigma}{\rho}}. \quad (5.3)$$

Eq. (5.3) shows that the resonance frequencies depend only on the intrinsic tensile stress, density ρ , and device length. The density of the device is estimated from our measured values of frequency and length of the string along with the tensile stress reported by the manufacturer, $\sigma = 0.8$ GPa. Our estimated value of density is 3000 kg/m^3 which is consistent with other reported values [49].

We now briefly discuss the form of the damping coefficient. Since the experimental chamber is evacuated to $\sim 2 \times 10^{-6}$ torr, the dissipation cannot have a substantial contribution from any viscous term z_t that depends on the absolute motion of the string [9]. Instead, the leading order contribution from internal material processes must go as $z_{xx,t}$, which describes how fast a volume element in the string is moving with respect to neighboring ones. The exception is in the vicinity of the end points, where dissipation can depend on the time rate of change of the angle that the string makes with respect to its connection point ($z_{x,t}$). By this reasoning it is convenient to consider that the total dissipation γ_n comes from three major contributions.

Hence, the effective Q for each mode of a nanostring is

$$\begin{aligned} Q_n &= \frac{m\omega_n}{\gamma_n} \\ &= \frac{m\omega_n}{\gamma_n^{\text{visc}} + \gamma_n^{\text{anchor}} + \gamma_n^{\text{bulk}}}, \end{aligned}$$

as calculated in [10].

Here, we consider viscous damping γ_n^{visc} , damping at anchor points γ_n^{anchor} , and damping due to bulk bending γ_n^{bulk} . Let us define $\gamma_n^{\text{visc}} = \tilde{\gamma}^{\text{visc}}$, $\gamma_n^{\text{anchor}} = \tilde{\gamma}^{\text{anchor}}\omega_n \sim \sigma^{-1/2}\omega_n$, and $\gamma_n^{\text{bulk}} = \tilde{\gamma}^{\text{bulk}}\omega_n^2 \sim \sigma^{-1}\omega_n^2$. The tilde-decorated quantities are material constants that have had their leading order ω_n dependence factored out. Hence,

$$Q_n \approx \frac{m}{\tilde{\gamma}^{\text{visc}}\omega_n^{-1} + \tilde{\gamma}^{\text{anchor}} + \tilde{\gamma}^{\text{bulk}}\omega_n}. \quad (5.4)$$

Note that there is a characteristic mode number dependence to each contribution. In particular, Q values that are roughly constant across modes are indicative of

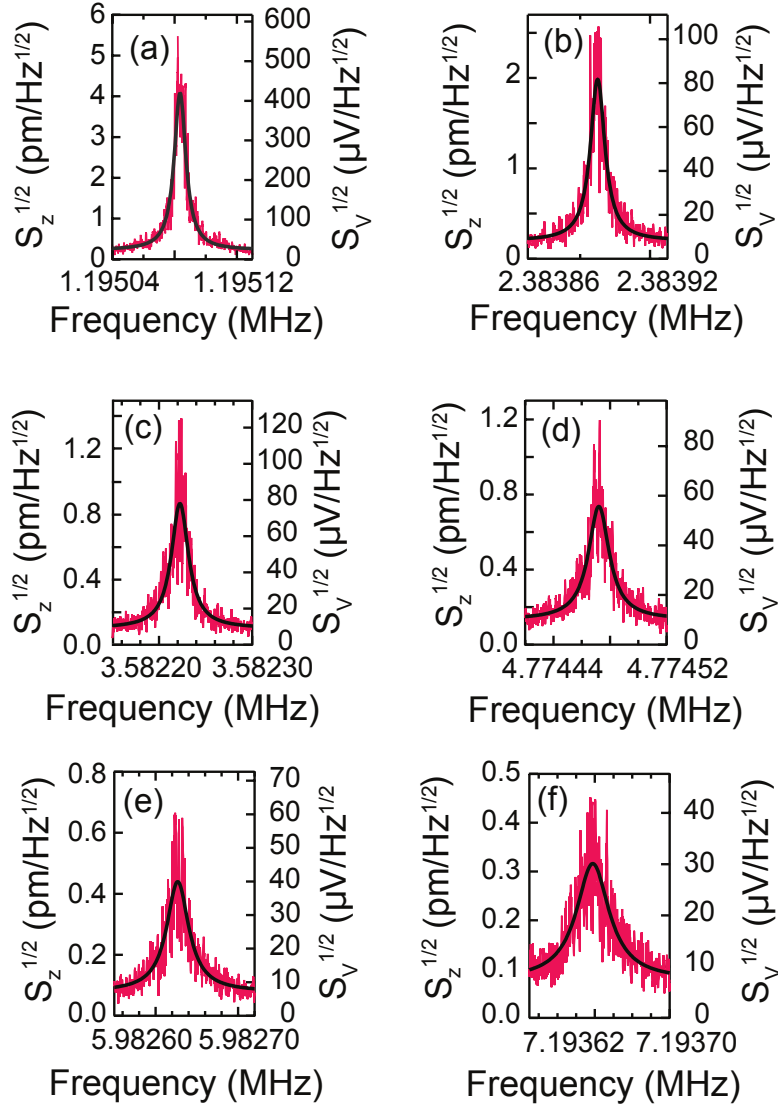


Figure 5.4: The post-processed (a sliding average over five points) thermo-mechanical spectra of the first six harmonics. The data is calibrated by fitting to an analytical expression for the power spectral density function.

dominant dissipation at anchor points. This is consistent with our understanding that the relative contribution $\tilde{\gamma}^{\text{bulk}}/\tilde{\gamma}^{\text{anchor}} \sim 1/\sqrt{\sigma}$ is likely to be small in high stress materials.

5.4 Thermomechanical calibration and peak displacements

Once a thermally driven spectrum is acquired, as in Fig. 5.4, we calibrate the voltage signal to an absolute displacement via the equipartition theorem. This calibration gives us the quantitative comparison of different loss channels. The calibration is performed by fitting the power spectral density (PSD) of the resonator as discussed in Chapter 2. The experimental PSD is determined by the square of the voltage signal divided by the measurement bandwidth. The fitting gives four parameters: the displacement noise floor, the Q , the resonance frequency, and the factor α (having units m^2/V^2) that converts between the voltage signal and the displacement spectrum. The only input parameter is the effective mass of the nanostring, which we compute from the geometrical mass (M_{geo}) of the string as $m = \frac{1}{2}M_{geo} = \rho Lwt$ [30]. The thickness $t = 250$ nm is the same in all devices, whereas the width w varies. Therefore accurate knowledge of the density and geometry is important for this calibration.

The peak displacements and the quality factors Q_n of the beam at the resonance frequencies are shown in Fig. 5.5(a) and Fig. 5.5(b), respectively. Calibration is repeated for each measurement of a resonance spectrum, since α varies with the location of our laser spot. Fig. 5.5(a) shows that the peak displacement has degeneracies between certain modes of different nanostrings. The second mode of the 215 μm device and the first mode of the 102 μm device are nearly identical. Similarly the 6th mode of the 215 μm device, the third mode of the 102 μm device and the second mode of the 74 μm device are nearly identical. This is the consequence of n/L dependency of frequency in Eq. (5.3). The width of the nanostring has been shown to be important when $w > 3 \mu\text{m}$, [11] but when $55 \text{ nm} < w < 1.5 \mu\text{m}$ the Q is independent of w at low pressures [9]. Note that the mode shapes and peak displacements of the higher harmonics of a longer string are similar to that of a shorter string with identical frequencies but different Q s (Fig. 5.5). From thermomechanical calibration we can show that they have identical peak displacements with identical local curvatures. Hence the Q s can not be limited by dissipation due to bulk bending. The only difference in Q arises from the ratio of anchor points (two) to the number of lossless nodes ($n-1$). This ratio is smaller for higher harmonics of a longer string than the modes of a smaller string with identical frequencies, which

means that dissipation is dominated by the anchor points. This dissipation occurs either through local curvature at anchor points [11, 12] or the tunneling of phonons [13, 14], which could not be differentiated by this experiment.

We are also able to find quantitative information about the dissipation from the peak displacement versus frequency curve. This analytical result can be found from the expected frequency dependence for the peak displacement of the nanostring.

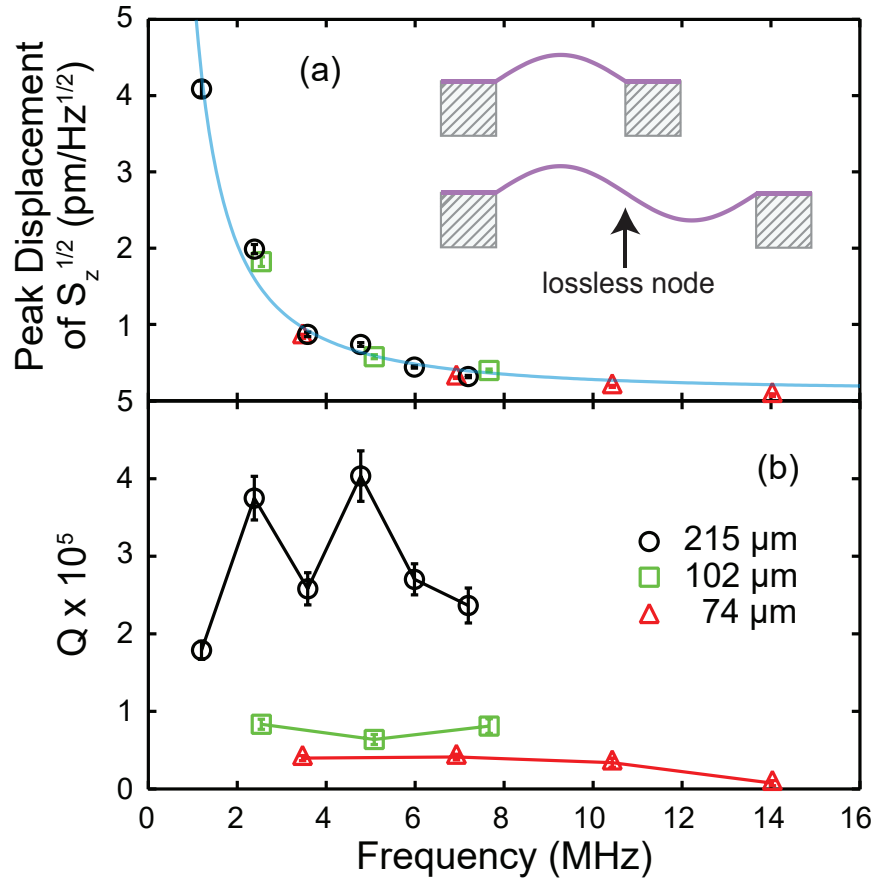


Figure 5.5: (a) Peak displacement and (b) Q from thermomechanical calibration of three devices, all 250 nm thick. Black circles are for a string 215 μm long and 2.1 μm wide, green squares for 102 μm long and 1.1 μm wide, red triangles for 74 μm long and 1.2 μm wide. The blue curve in (a) is a fit to Eq. 5.6

The spectral density of the squared displacement is [10]

$$S_n(f_n^{\max}) = \frac{Q_n k_B T}{m\pi^3(1 - \frac{1}{4Q_n^2})f_n^3}; \quad (5.5)$$

the corresponding displacement $\Delta z = \sqrt{S_n(f_n^{\max})\Delta f}$ over an arbitrary frequency interval Δf goes as

$$\begin{aligned} \frac{\Delta z}{\sqrt{(\Delta f)}} &= \sqrt{S_n(f_n^{\max})} \sim \sqrt{\frac{Q_n}{f_n^3}} \\ &\sim \frac{1}{f_n^{3/2}} \sqrt{\frac{m}{\tilde{\gamma}^{\text{anchor}} + \tilde{\gamma}^{\text{bulk}}\omega_n}} \\ &\sim \frac{1}{f_n^{3/2} \sqrt{\tilde{\gamma}^{\text{anchor}} \sqrt{1 + (\tilde{\gamma}^{\text{bulk}}/\tilde{\gamma}^{\text{anchor}})2\pi f_n}}} \\ &\sim \frac{1}{f_n^{3/2} + \tau f_n^{5/2}}. \end{aligned} \quad (5.6)$$

Fitting of this equation to the data in Fig. 5.5(a) gives a value of $\tau = \pi\tilde{\gamma}^{\text{bulk}}/\tilde{\gamma}^{\text{anchor}} = (-0.3 \pm 2.5) \times 10^{-7}$ s which is effectively zero within measurement error. This limit, $\tau^{-1} \gg f_n$ for all measured n , confirms that the dissipation due to bulk bending is negligible when compared to the dissipation at anchor points. Fig. 5.5(b) shows weak variation of Q with respect to mode number which comes from an additional even/odd effect related parity of the mode shape due to phonon tunneling through anchor points [14]. We note that characteristics of dissipation is strongly controlled by the design of the junction between the string and the support. Fitting the calibrated peak displacement versus frequency of the thermomechanical motion could be a straightforward test of the dominant dissipation and can be applied to other designs.

Identification of the anchor points as the major source of dissipation provides a path for further increasing the Q of nanostrings under tensile stress. Specifically, one could design clamping points at the ends of the beams that either carefully suspend the device [50], or reflect phonons back into the string instead of allowing them to leak into the substrate. This has been achieved in part in Ref. [51] by clever fabrication of the nanostrings and sample mounting. The ultimate scheme to eliminate clamping loss would be to design clamping points with complete phononic bandgaps at the frequencies of the mechanical modes of the nanostrings. This was

accomplished for very high frequency modes (> 3 GHz) [52, 53].

In conclusion, I have fabricated high Q silicon nitride nanostrings that enable multimode thermomechanical calibration. One set of devices fall upon a single curve of peak displacement versus frequency, even though the mechanical Q of these devices do not. Different modes on different strings, with identical frequency and identical peak displacement but different Q s, eliminates the possibility of bending and intrinsic loss mechanisms as dominant. Instead, clamping loss mechanisms dominate in high stress nanostrings. Engineering of the clamping dissipation promises to increase further the possible applications of nanostrings.

CHAPTER 6

Remote Sensing in Hybridized Arrays of Silicon Nitride Nanostrings¹

After exploring the dissipation mechanisms of high-stress silicon nitride nanostrings in Chapter 5, we now know most of the dissipation is at the anchor points due to bulk bending or phonon leaking [10]. In this chapter we explore a design of the anchor points at the ends of the string to increase Q . We design our strings in such a way that it could reflect the phonon back into the string at anchor points. We make arrays of strings by attaching one string after another to make both linear and circular arrays. The linear array will help to reduce the out-of-plane phonon leaking through anchors and the circular array will help to reduce both in-plane and out-of-plane phonon leaking. As we will explain, instead we find hybridized modes provide remote sensing mechanism for a strongly coupled system.

6.1 Mode shapes and eigenfrequencies of a hybridized array

We make arrays of strings by attaching one string after another to make both linear and circular arrays. The linear array will help to reduce the out-of-plane phonon leaking through anchors and the circular array will help to reduce both in-plane and out-of-plane phonon leaking. As we will explain, instead we find hybridized modes provide remote sensing mechanism for a strongly coupled system.

¹A version of this Chapter has been published. Biswas *et al.*, *Nano Lett.* **4**, 2541 (2014)

Fig. 6.1(a) shows SEM images of single string, two-string and three-string arrays made from high-stress silicon nitride. Each string is $50 \mu\text{m}$ long, $2.4 \mu\text{m}$ wide and 250 nm thick. The strings are connected internally by a tiny post and the boundaries are fixed by heavier posts at the ends in an array. An enlarged SEM image of a connecting post is shown in Fig. 6.1(c). The coupling between these strings depends on the post size which can be tuned by etching during fabrication. The chip is mounted on a piezo actuator inside an optically accessible vacuum chamber.

Fig. 6.2(c)–(d) shows the thermomechanical signal amplitudes for the two-string array. Interestingly each string shows two ‘fundamental’ resonance frequencies corresponding to two different modes. This confirms that two strings coupled to each other in this way form a hybridized system. The system has a resonant peak at $\approx 5.2054 \text{ MHz}$ and another resonant peak at $\approx 5.2646 \text{ MHz}$. The spacing in frequency between modes is determined by the coupling strength of the hybridized system [20]. There is a small difference in the amplitudes of two strings at each resonant frequency due to the imperfection of fabrication process, which leads to slight differences in the effective length and hence the relative displacement amplitudes.

In addition to thermomechanical signal, we can drive our device externally, using a piezo buzzer in our case. This helps to detect the mode shapes of the resonance

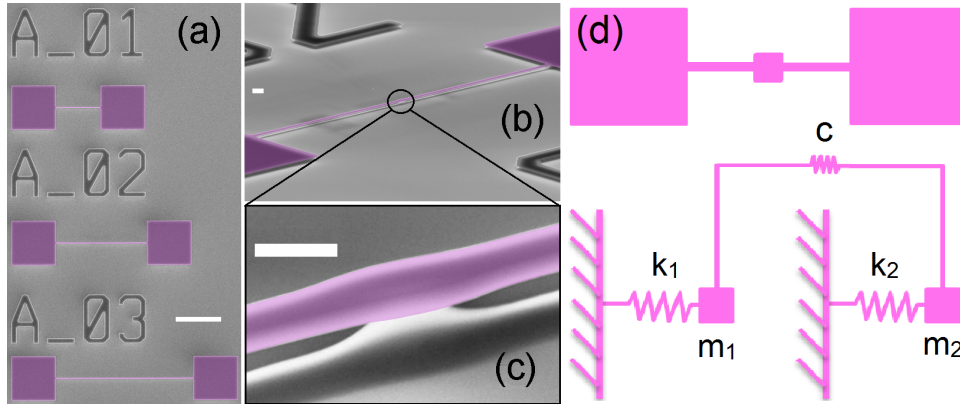


Figure 6.1: Scanning electron microscope (SEM) image of the $50 \mu\text{m}$ long string arrays with false color. (a) Several arrays with different numbers of strings (scale bar $100 \mu\text{m}$), (b) tilted SEM image of two-string array (scale bar $2 \mu\text{m}$) and (c) tilted and zoomed SEM image of a connecting post (scale bar $2 \mu\text{m}$).

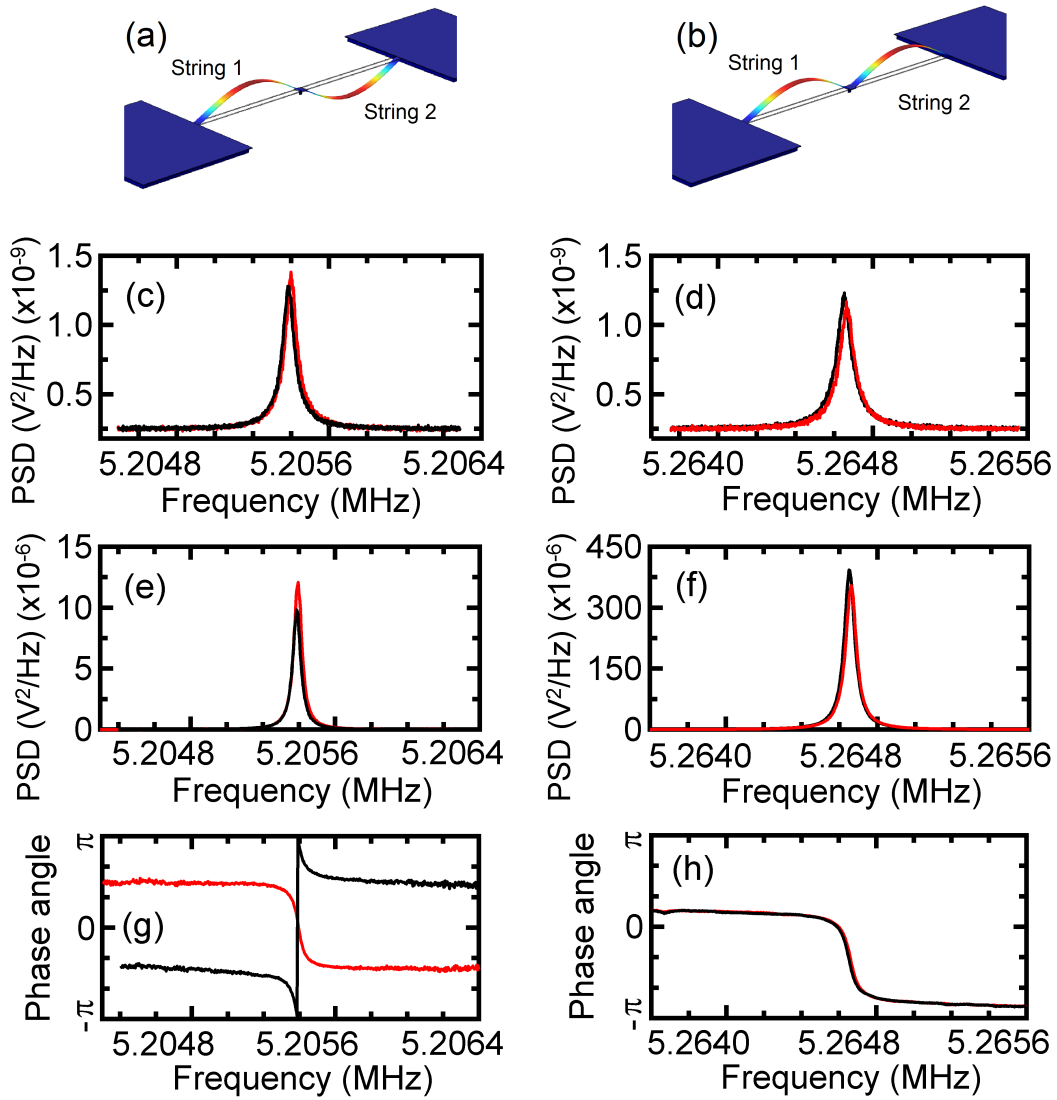


Figure 6.2: (a)–(b) antisymmetric and symmetric mode shapes for two-string array using FEM simulation, (c)–(d) thermomechanical signals, (e)–(f) driven signals with 1 mV piezoelectric drive voltage and (g)–(h) phase shift for antisymmetric and symmetric modes. Red and black lines represent the data for strings 1 and 2 in the array respectively. The Q s associated with the symmetric and antisymmetric modes are $\approx 7.6 \times 10^4$ and $\approx 10.4 \times 10^4$.

frequencies of the coupled strings. A 10 mV AC signal is applied across the piezo buzzer and the corresponding driven string phase angle is shown in Fig. 6.2(g)–(h).

It confirms that two strings are in phase at the higher frequency and out of phase at the lower frequency. This indicates that the lower frequency has anti-symmetric mode shape and the higher frequency has symmetric mode shape. Fig. 6.2(e)–(f) show the amplitude for both strings when the strings are actuated externally. The amplitude of the higher frequency mode is ~ 30 times higher than that of the lower frequency mode. This is because the external force acts in phase on both strings resulting in a reduction in amplitude for antisymmetric mode compared to symmetric mode, justifying our identification of symmetric and antisymmetric modes. In contrast, for both cantilevers [20] and beam-like resonators [22] coupled by an overhang, the symmetric mode has a lower frequency than the antisymmetric mode. This is due to the twisting of the overhang in the antisymmetric mode, which costs more energy. In our system, two $50\ \mu\text{m}$ strings are mechanically coupled by a small connecting post (top area $\sim 450\ \text{nm} \times 1\ \mu\text{m}$) as shown in Fig. 6.1(b). In this case, the bending in the vicinity of the post is more energy-consuming in the symmetric mode. As a result, the antisymmetric mode has lower frequency than the symmetric mode. Furthermore, FEM based COMSOL simulations (Fig. 6.2(a)–(b)) also confirm that the symmetric mode shape is associated with higher frequency and the anti-symmetric mode shape is associated with lower frequency.

It is also possible to solve for the eigenfrequencies and their corresponding mode shapes analytically using a simple spring model. We can model the system by undamped simple harmonic oscillators due to their high Q s. According to this model, each string can be considered as a separate spring and they are connected with another spring (Fig. 6.1(d)). Let us consider that one string has spring constant k_1 and effective mass m_1 and another string has spring constant k_2 and effective mass m_2 . In that case, the system matrix can be written as

$$\omega^2 \begin{pmatrix} x_1 \\ x_2 \end{pmatrix} = \begin{pmatrix} \frac{k_1+c}{m_1} & \frac{c}{m_1} \\ \frac{c}{m_2} & \frac{k_2+c}{m_2} \end{pmatrix} \begin{pmatrix} x_1 \\ x_2 \end{pmatrix}, \quad (6.1)$$

where c is the coupling spring constant. After solving this system matrix and using the approximation $m_1 \approx m_2 \approx m$, it is possible to find eigenfrequencies for the coupled system,

$$\omega_{2,1} = \frac{1}{2m} \left[k_1 + k_2 + 2c \pm \sqrt{(k_1 - k_2)^2 + 4c^2} \right]. \quad (6.2)$$

This equation shows two eigenfrequencies for a coupled two-string array. Thus the simple model qualitatively shows that the system of N coupled nanostrings becomes hybridized and it shows N different eigenfrequencies.

The coupling for a three-string array is also of interest. Fig. 6.3(a) shows three fundamental mode shapes with corresponding frequencies using FEM based COMSOL simulations. It is also possible to draw a schematic of a mode shape of a corresponding frequency from thermomechanical amplitudes and driven phases of different strings at that particular frequency. The thermomechanical signal amplitudes of the three different modes for each string are shown in Fig. 6.3(b). It reveals that the array has a resonant peak at ~ 5.079 MHz, where the middle string oscillates strongly. The next two higher resonant frequencies are found at ~ 5.2206 MHz and ~ 5.2485 MHz. For the second mode, two end strings have similar amplitudes of vibration and the third string vibrates strongly in the third mode. This behavior mainly comes from the imperfection of fabrication process which produces different effective lengths and spring constants for the strings. The middle string oscillates significantly in the lowest mode, which is possible if the effective length of L_2 is bigger than L_1 and L_3 .

Figure 6.3(c) shows the driven signal amplitudes of three fundamental modes for the array. The two end strings are in phase in the lowest mode, ~ 5.079 MHz, while the middle string is out of phase. The end strings are out of phase with each other in the next mode, ~ 5.2206 MHz. The middle string is in phase with the first string and out of phase with third string. The highest mode has resonant frequency ~ 5.2485 MHz with all three strings in phase. It is interesting to note that the driven amplitude of each string at the highest fundamental mode (all strings are in phase) is not larger compared to that of two other modes. This is opposite to the case of two-string array where both strings show higher driven amplitudes at higher frequency (strings are in phase). This suggests that the dissipation mechanism in two string array is different than that in three string array.

6.2 Q -enhancement in coupled arrays

In addition, thermomechanical voltage signal can be converted to a PSD. Fitting to a theoretical PSD allows us to extract four parameters including the Q of a

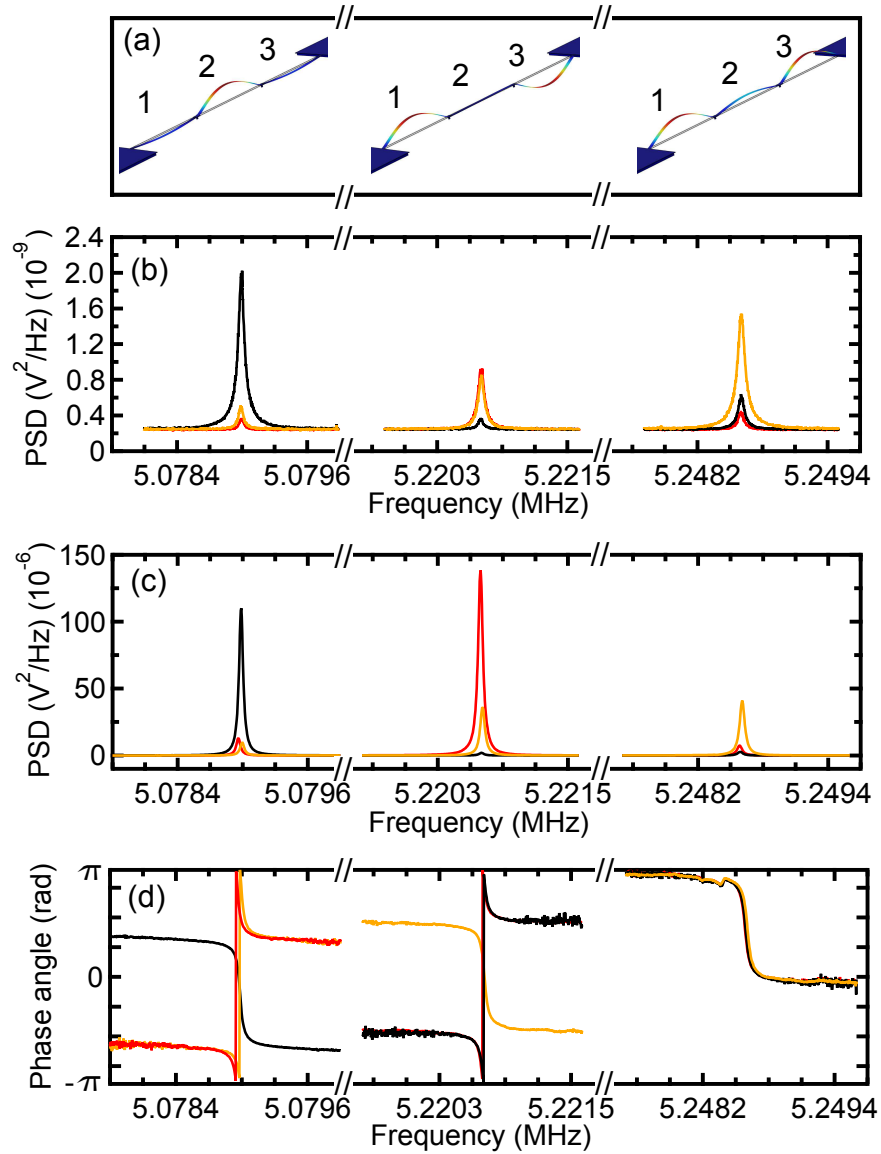


Figure 6.3: (a) Three different mode shapes for the three-string array from FEM simulation. 1, 2, and 3 present 1st, 2nd, and 3rd string in the array respectively, (b) thermomechanical signal amplitude for three different modes for each string, (c) driven signal amplitudes for three different modes for three different strings and (d) phase angle for each string in three different modes. The red, black and orange lines represent 1st, 2nd and 3rd string in the array respectively.

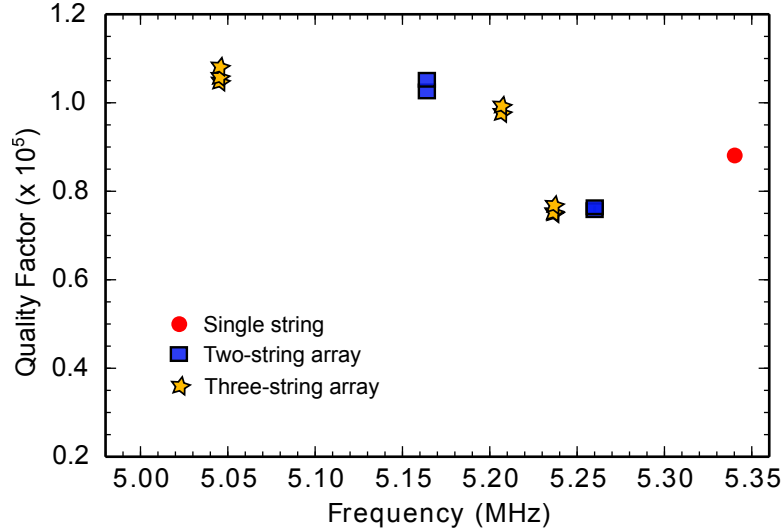


Figure 6.4: Q comparison for a single string, a two-string and a three-string array.

string. The Q s of a single string, two-string array and three-string array can be compared to see the variation of dissipation in different arrays. The single string has one fundamental frequency at 5.34 MHz and the associated Q is $\approx 5.7 \times 10^4$. Two-string system has two frequencies corresponding two different modes. Fig. 6.4 shows that Q s associated with lower frequency modes for both strings have a higher value compared to that of the higher frequency modes. Interestingly, the Q s of higher frequency modes are smaller than that of the single string. However, the Q s of lower frequency modes are increased by $\sim 16\%$ compared to the single string Q . This indicates a small Q enhancement in the two-string array. Both strings have identical frequencies and are coupled to each other by a tiny post. Two strings are in phase for symmetric mode (higher frequency) and out-of-phase for anti-symmetric (lower frequency) shape. The forces exerted by each string on the connecting post are almost identical but in opposite directions for the anti-symmetric mode. This reduces phonon leaking out of the string through the connecting post in comparison with the symmetric mode.

For further investigation, we extract Q s for the three-string system. This system is more complicated than the two-string array. It has three different mode shapes associated with three frequencies. In Fig. 6.4, the Q s associated with high mode

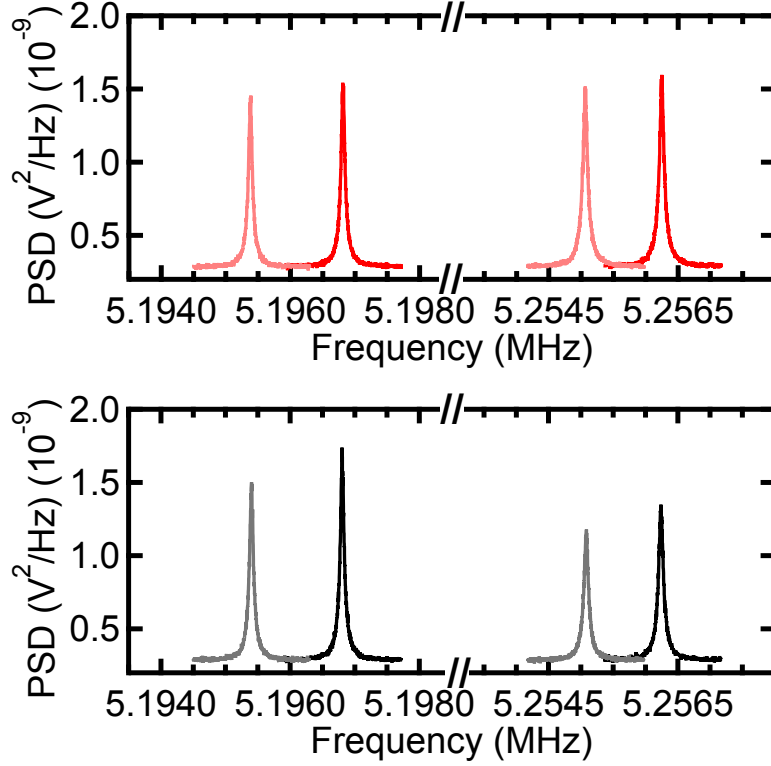


Figure 6.5: (a)–(b) The thermomechanical signal amplitudes of the two-string array both before and after a mass deposition on the 2nd string in the array. Red and black colors represent 1st and 2nd string in the array. Dark and light colors represent PSD of the strings before and after mass deposition respectively.

frequency are smaller than the single string's Q . However the Q s of lower mode frequencies are higher than that of the single string. The Q enhancement is $\sim 20\%$ (for highest Q s) in the three-string array compared to the single string's Q . In addition, the Q is increasing slowly with the number of strings in an array (considering higher Q s only). This also supports the hypothesis that dissipation comes mostly from anchor points due to phonons leaking out at anchor points. We need to study the dissipation mechanism in detail to understand this Q variation which depends both on mode shape and string in the array.

6.3 Allan deviation of frequency and amplitude

Due to the promising Q enhancement of the arrays, it may be possible to use them as sensors. In the literature [19, 20], it has been suggested to use the amplitude change instead of the frequency change for better mass sensitivity in a coupled system. Hence we have performed the experiment to observe the frequency and amplitude variation of our system by depositing mass on a particular string in a two-string array. The mass is deposited by a highly collimated electron beam from

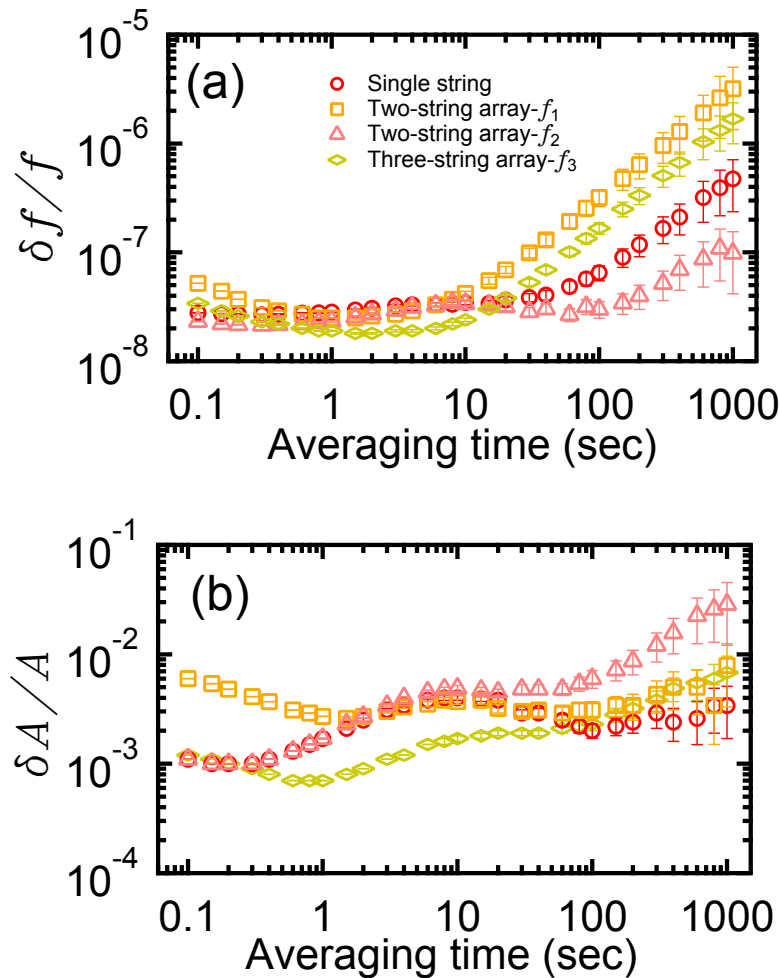


Figure 6.6: The thermomechanical signal The stability of (a) frequency and (b) amplitude for different string array.

a scanning-electron microscope (SEM) onto the middle of the 2nd string in two-string array. The SEM is focused through a small window ($\sim 3.5 \times 6.5 \mu\text{m}^2$) for 120 s. The SEM is also focused onto the middle of a single string for same time with same window. The added mass is then calibrated from the frequency shift of the single string, which is ~ 30 fg. Deposition of small mass on a string resulting a change in the oscillation amplitudes of the array. Fig. 6.5 shows the thermomechanical signals of two fundamental modes before and after adding mass. The resonance frequencies are shifted to lower values for both antisymmetric and symmetric modes due to the mass deposition in the array. The amplitudes also decrease for both symmetric and anti-symmetric mode frequencies. The observed frequency shifts for both modes measured on both strings are ~ 0.025 %. However the relative changes in amplitude are ~ 5 % and ~ 15 %, respectively, for both modes when measured for string 1 and string 2. The amplitude change is at least 3 orders of magnitude higher than the frequency change in our two-string system. Thus we have done a careful measurement to see the stability of amplitude and frequency of our system.

The stability of a resonator is an important feature for the detection of any perturbation to the resonator, since it sets the limit of the smallest possible detection. Specifically, we are interested in the stability of the resonant frequency and the maximum amplitude of our resonators. To quantify the resonant frequency fluctuations, we have used the Allan deviation [54] $\sigma_{Allan}(\tau_A)$ defined as :

$$\sigma_{Allan}(\tau_A)^2 = \frac{1}{2(N-1)} \sum_{m=2}^N \left(\frac{f_m - f_{m-1}}{f_0} \right)^2 \quad (6.3)$$

where f_m is the average resonant frequency measured over the m^{th} time interval τ_A , N is the total number of intervals τ_A , and f_0 is the initial resonant frequency.

There are different methods to calculate this Allan deviation, one can measure directly the resonant frequency over time and compute Eq. (6.3), or one can measure the phase noise fluctuations through the spectral density function and then compute the Allan deviation. We have chosen the first method using the phase locked loop (PLL) technique of our high frequency lock-in amplifier (model HF2LI from Zurich Instrument). The resonant frequency of our resonator is locked using the PLL, which adjusts continuously the drive frequency such as the response signal from the detection side was shifted by $\pi/2$ from the drive signal. The parameters of the PLL are optimized relative to the lock-in time constant prior to taking the measurements

of the resonant frequency over time. The data, shown in Fig. 6.6(a)-(b), is taken with a lock-in time constant of $400 \mu\text{s}$ and post averaged over different time intervals τ_A ranging from 0.1 s to 1000 s. Fig. 6.6(a) shows a relative frequency stability better than 6×10^{-8} leading to a mass sensitivity of a few attograms, for averaging times as large as 40 s which is a time period much longer than the duration required to measure the resonant frequency of a device. The instability in the resonant frequency of our resonator for longer time period might have different origins, it can come from mechanical vibrations, temperature fluctuations, local heating of the laser, etc. The measurement technique with the PLL itself can introduce an additional instability. We have presented the frequency stability of our devices within the actual experimental set-up, even though this is not necessarily their ultimate limit of frequency stability.

We further measured the amplitude of the signal at the resonant frequency and computed a similar deviation as the Eq. 6.3 but using the maximum amplitude instead of the resonant frequency. The maximum amplitude stability is mostly of the order of 10^{-3} as shown in Fig. 6.6(b). Thus the frequency stability is at least 4 orders of magnitude higher than the amplitude stability for the three string array and 5 orders of magnitude higher for two string array and single string. There are different mechanisms that can explain the lack of amplitude stability relative to the frequency stability. The most likely is that the measured amplitude is not as intrinsic as the resonant frequency of the resonator, since it depends, for example, on the quality of the adjustment of the optics. Hence it is unlikely to use amplitude parameters instead of frequency parameters for mass sensing.

6.4 Remote sensing in hybridized array

Finally, we have realized possible advantages of these hybridized arrays of nanos-trings for mass sensing applications in a different way. We have deposited mass at the femtogram level in a series onto a particular string in two- and three-string array using SEM. Figure 6.7 shows the variation of resonant frequencies and ratio (of two frequencies) of a two-string array due to mass deposition on target strings 2 and 1 in turn. It is observed that frequencies of both fundamental modes f_1 and f_2 are shifting downward with different slopes for mass deposition on strings 2 (Fig. 6.7(a)-(b)) and 1 (Fig. 6.7(d)-(e)) in the array. Interestingly the ratio of f_1/f_2 decreases for

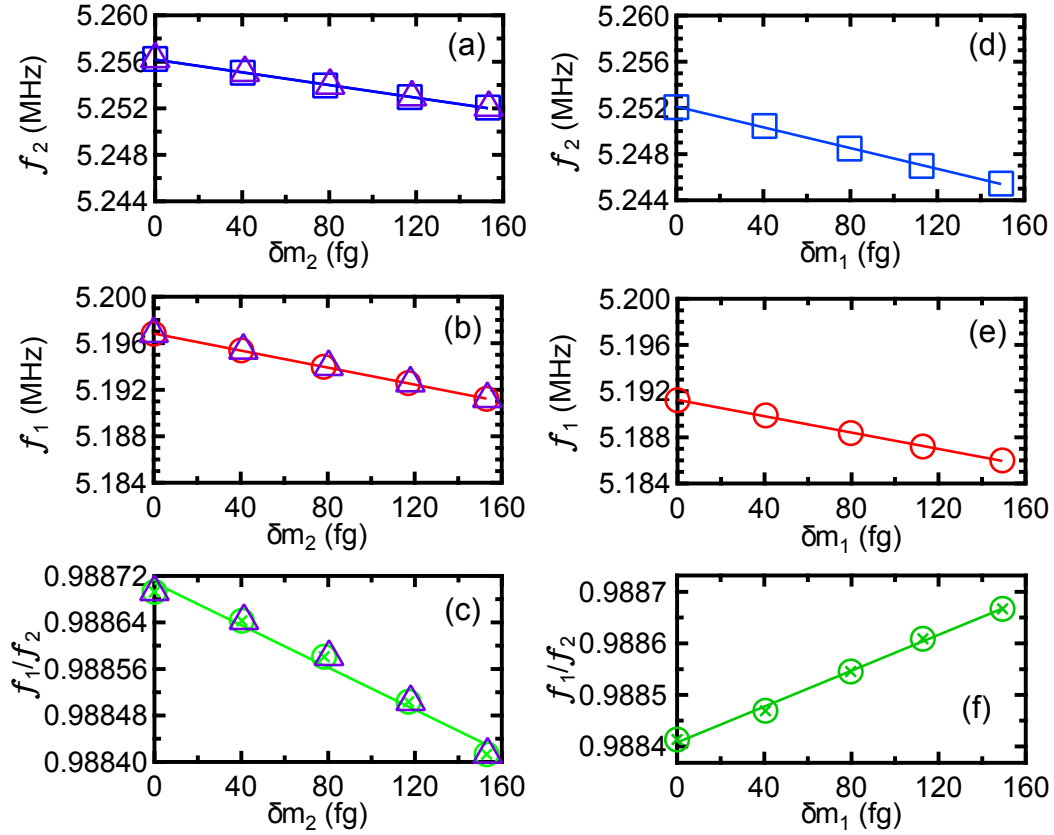


Figure 6.7: Frequency response for mass deposition on (a–c) second string and (d–f) first string in the array. Circles, squares and triangles represent individual experimental data.

the first case (Fig. 6.7(c)), but increases for the second case as shown in Fig. 6.7(f). From this ratio, it is possible to infer onto which string the mass is added. For example, the frequency ratio would go upward for mass deposition onto the string 1 for this two-string array. It is worth noting that the experiment is performed only on a single string of the array to get the information that provides an opportunity for remote sensing. Only drawback of this process is the mass calibration which is done from a single string with similar dimensions. Instead it is possible to use this frequency ratio to figure out the position (on which string) of the deposited mass and Eq. 6.2 can be used to calculate the deposited mass. Lets say a small mass δm_2 is deposited onto string 2 in two-string array which changes the spring constant k_2

to $(1 - \delta m_2/m)k_2$. Then Eq. 6.2 can be used to get an expression for δm_2 as

$$\frac{\delta m_2}{m} = \frac{\frac{k_1+c}{m} + \frac{k_2+c}{m}}{\frac{k_2}{m}} - \frac{\omega_2'^2 + \omega_1'^2}{\frac{k_2}{m}} \quad (6.4)$$

The $\omega_2'^2$ and $\omega_1'^2$ are shifted frequencies for the mass deposition. Knowing these subsequent frequencies one can calculate the deposited mass. In Fig. 6.7(a)-(c), triangles (purple) present calculated masses, which match with calibrated masses. Similarly, it is possible to extend this scheme to a three-string array for further experimentation.

In conclusion, in this Chapter we studied one dimensional arrays and we were expecting to get large Q -enhancement. We found a modest improvements in Q . However, we found that strong coupling in an array provides mode hybridization which provides remote sensing opportunity. Therefore a coupled array (two-string, three-string and so on) providing remote sensing greatly simplifies the measurement of the array and could have applications in parallel molecular analysis. Moreover, we solved the dispute for the stability of the frequency and the amplitude of a resonator.

CHAPTER 7

Explosive Molecule Detection by silicon nitride nanostrings

1

After characterization of silicon nitride nanostrings in Chapters 5 and 6, we started to implement these strings in sensing applications. To accomplish, in this chapter, we demonstrate detection of the explosive molecule 1,3,5-trinitroperhydro-1,3,5-triazine (RDX) using nanomechanical resonators combined with photothermal spectroscopy and mass desorption.

7.1 Adding chemical specificity

Nanomechanical resonators are good candidates as sensors because of their small mass, high frequency and high quality factor. In particular for mass sensing, the absorbed mass is estimated from the shift in mechanical resonance frequency. Fantastic progress has been made in mass sensitivity, reaching the single protein [56, 55] and even yoctogram mass level [57]. Yet this technique alone is not sufficient to identify the adsorbent molecule. We must add a second technique to our system to gain chemical specificity. Photothermal infrared (IR) spectroscopy [58, 59, 60, 61, 62, 63, 64], a technique based on IR absorption by resonant molecular vibrations, is straight forward, simple, and easy to couple to the system.

¹A version of this section has been published in Analytical Chemistry. Biswas *et al.*, *Anal. Chem.* **86**, 11368 (2014).

The molecule absorbs light at the wavelength of its molecular vibration, producing heat, resulting in a shift of the resonance frequency of the resonator. Combining this IR absorption spectroscopy with nanostring mechanical resonators, we have detected femtogram levels of the explosive molecule 1,3,5-trinitroperhydro-1,3,5-triazine (RDX), representing the lowest RDX values ever measured by IR spectroscopy.

7.2 Measurement of RDX

The RDX samples were purchased from AccuStandard, Inc. (New Haven, CT) of concentration 1 mg/mL and used without further purification. RDX vapors are deposited on the sample by passing nitrogen at a fixed flow (200 sccm) through a thermal vapor generator (100 °C for 6 minutes at ambient pressure). This technique mimics in-the-field thermal vaporization of a swab containing trace explosive residue and was performed by Prof. Thomas Thundat's group in the department of Chemical and Materials Engineering at University of Alberta. The calibrated initial amount of RDX are 2.72, 0.224, and 0.212 pg, deposited onto 215, 174 and 150 μm long string. The corresponding mass/area are calculated as 4.25, 0.437, and 1.696 g/m^2 for initial RDX deposited onto these strings. We have characterized the devices after this deposition both by optical microscopy, Figure 1a, and atomic force microscopy, Figure 1b. These reveal that the evaporated RDX condenses on the substrate in the form of nanoscale crystallites. Interestingly, we have found that RDX demonstrates preferential adsorption onto the silicon nitride surface, as opposed to the silicon substrate. As can be seen in the optical image of Figure 1a, there is a nonuniform distribution of the crystallites in the vicinity of the strings, with a higher percentage forming on the strings and the pedestals that support the strings. This is an unexpected bonus of using silicon nitride nanostrings for photothermal spectroscopy of RDX.

A schematic and a photograph of our experimental setup are shown in Fig. 7.3. After deposition and characterization, the chip, containing nanostrings, is mounted on the top of a piezobuzzer inside the vacuum chamber. A QCL is used in this set-up to produce IR laser. This laser is properly aligned using gold coated mirror and IR detection card. Usually, the IR laser can not transmit through glass window therefore the glass window is replaced by a ZnSe window. We can actuate our device

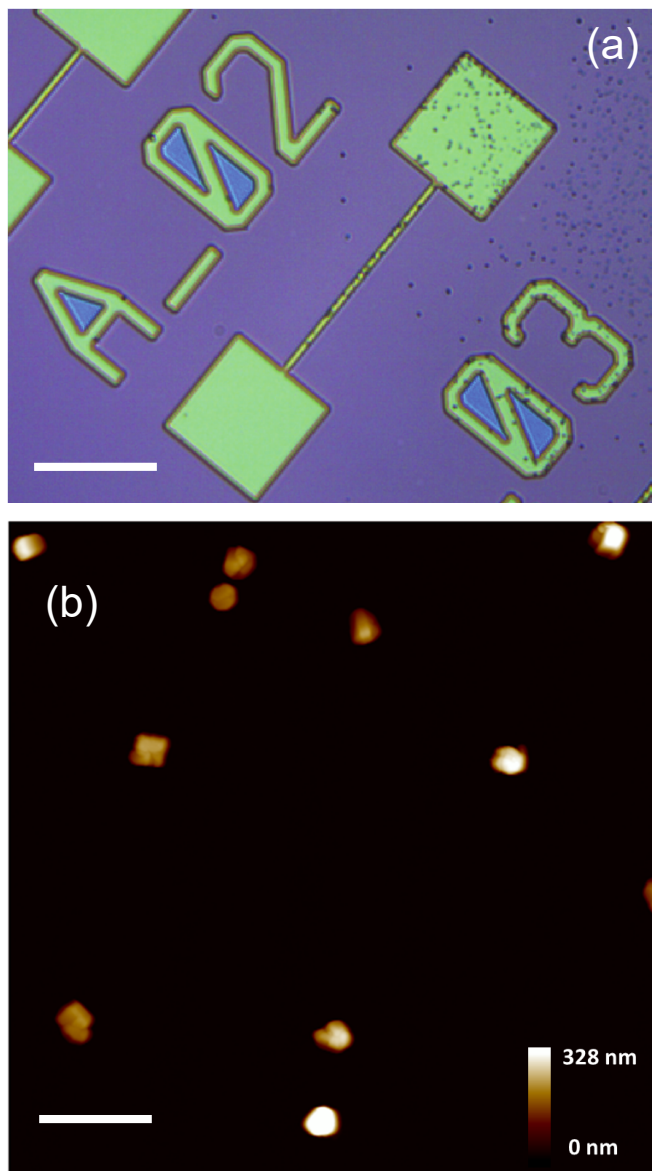


Figure 7.1: (a) Optical image of a 100 μm long silicon nitride nanostring with RDX on the surface. Note that the RDX crystallites have an affinity for the silicon nitride surfaces (green), as compared with the underlying silicon surface (purple). Scale bar 50 μm . (b) AFM topography of RDX crystallites on an un-patterned silicon nitride surface. Scale bar 1.5 μm

using this buzzer to determine the device resonance frequencies. Once determined, we eliminate the piezo drive and resolve the thermomechanical vibration of the string at room temperature. In this section I report only thermomechanical measurements.

In general, the addition of a perturbed mass to the string causes a frequency shift to lower frequency, which provides information about the amount of deposited mass [65]. In addition, for molecular specificity, here we combine our interferometric setup with photothermal spectroscopy [66, 67]. That is, a quantum cascade laser (QCL)[68] from Daylight Solutions (pulsed Über model) is used as an IR source to illuminate the RDX coated nanostrings. This is possible because the optical access of the vacuum chamber uses a ZnSe window, Fig. 7.2, allowing transmission of the IR wavelengths used in this experiment. The IR power is set constant at 300 mW peak power. The repetition rate is 100 kHz and the pulse length is 500 ns, with a duty cycle of 5 percent. The chamber is pumped to a moderate vacuum ($\sim 10^{-4}$ torr) to eliminate viscous damping of the nanostrings [3]. RDX slowly sublimates from the nanostring surface at this vacuum. We are therefore able to simultaneously perform measurement of the physical desorption, as well as photothermal spectroscopy of the RDX during the sublimation process.

The detection scheme is based on a straightforward interferometric technique which is discussed in detail in Chapter 4 and Chapter 5. Approximately one second of the time-domain interference signal is captured at each IR wavelength as the IR laser is stepped through its range at 1 cm^{-1} intervals. The time-domain data is then Fourier transformed to calculate the power spectral density, and automated fitting of the mechanical power spectral density [30] in the frequency domain data gives the center frequency of the mechanical resonance at sequential IR wavelengths. In a wavelength sweep of the QCL laser - when the IR wavelength reaches a vibrational resonance of the RDX molecules adsorbed on the nanostring - there is an additional frequency shift of the nanostring resonance frequency based on local resonant heating. This provides a molecular fingerprint of the adsorbed molecule, while the frequency shift from mass desorption provides a calibrated molecular mass.

We observe peaks from the vibrational spectroscopy of the adsorbed RDX near $7.55 \mu\text{m}$ (1320 cm^{-1}), a broad peak from the silicon nitride itself [63] near $8.2 \mu\text{m}$ (1220 cm^{-1}), and a background slope as shown in Fig.7.4(a). The background slope comes from the physical desorption of RDX occurring during the measurement. This slope can be subtracted by performing a second data run (without IR

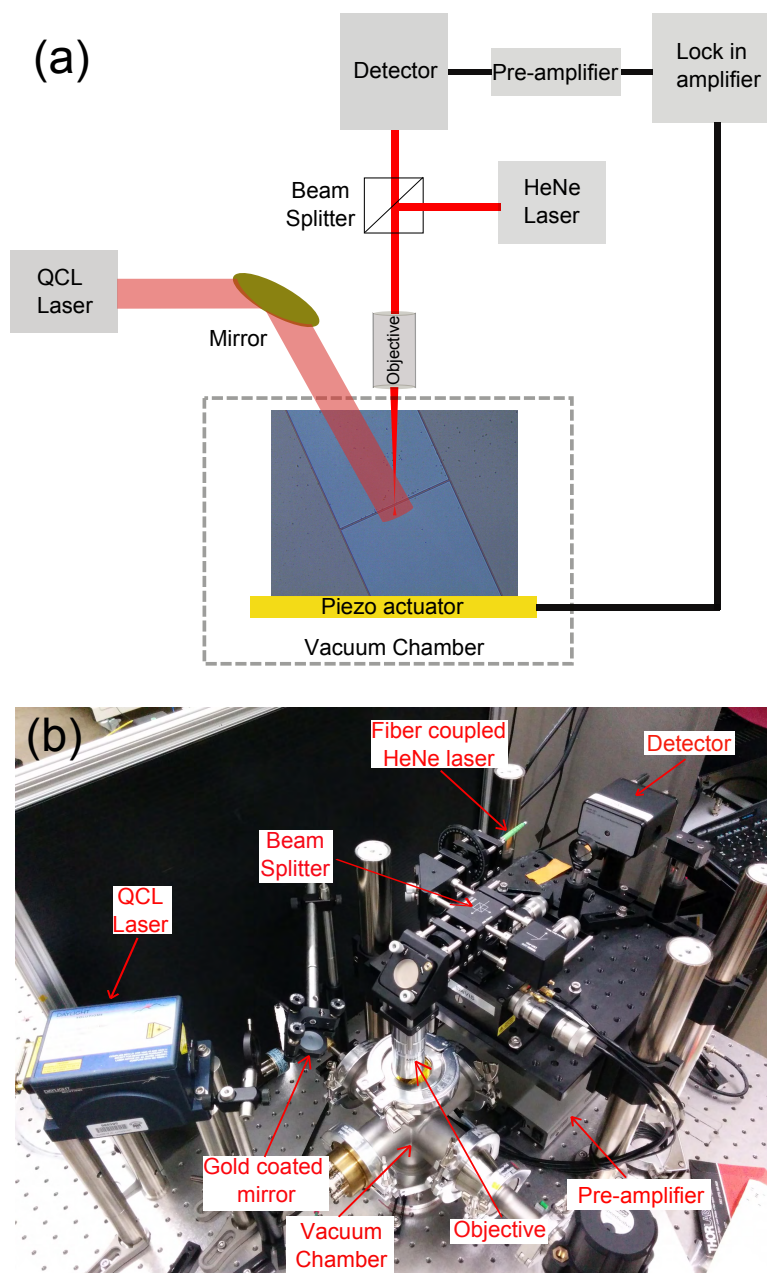


Figure 7.2: (a) Schematic and (b) photograph of the experimental setup. The various key parts are labeled.

illumination) immediately following the first data run (with IR illumination) shown in Fig.7.4(b). The broad silicon nitride peak can be subtracted after taking an ad-

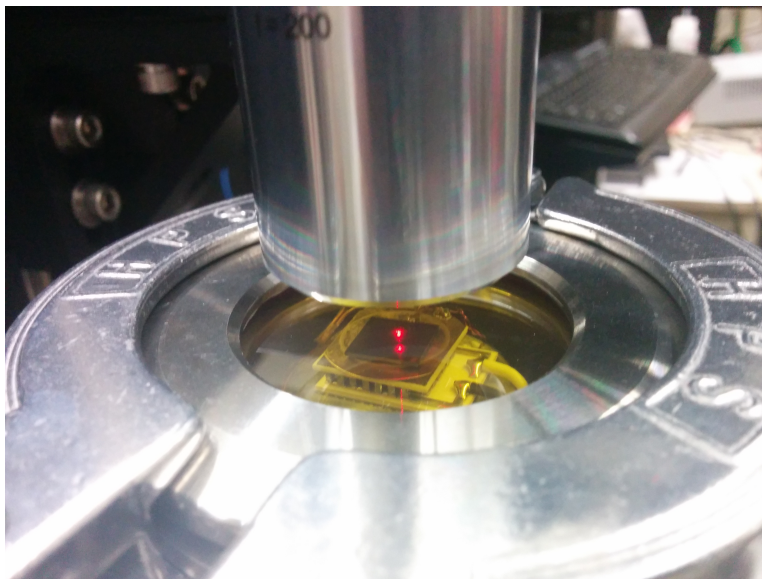


Figure 7.3: ZnSe window that allows to transmit IR laser through it.

ditional wavelength scan without any RDX onto the string. This scan can be taken once the RDX has been entirely pumped off the nanostring as shown in Fig.7.4(c). This control trace can also be taken before any RDX deposition onto the string. So the background subtraction involved three data sets, IR-on, IR-off, and silicon nitride background. Since these three data sets present three different frequency ranges, they should be either normalized or converted to relative frequency shifts. Here we converted them to the relative frequency shifts. After subtraction of IR-off and silicon nitride background data from IR-on data, three photothermal peaks from RDX are revealed, as in Fig.7.4(d). The peaks in this wavelength range have been previously identified to result from symmetric stretching of the N-NO₂ bonds in RDX [69]. Here these peaks result from a thermal stress relaxation of the silicon nitride nanostring, and therefore appear as shifts to lower mechanical resonance frequency [63].

Since a vibrational mode of the adsorbed RDX crystallites on the nanostring can be modeled as a damped harmonic oscillator we expect absorption peaks to be Lorentzian shaped. As seen in Fig.7.4(d), the data is fit to a line plus three Lorentzian peaks, the smooth dark blue curve. The data is slightly smoothed before the fit (not shown) to prevent spurious fitting of peaks to single data points in low

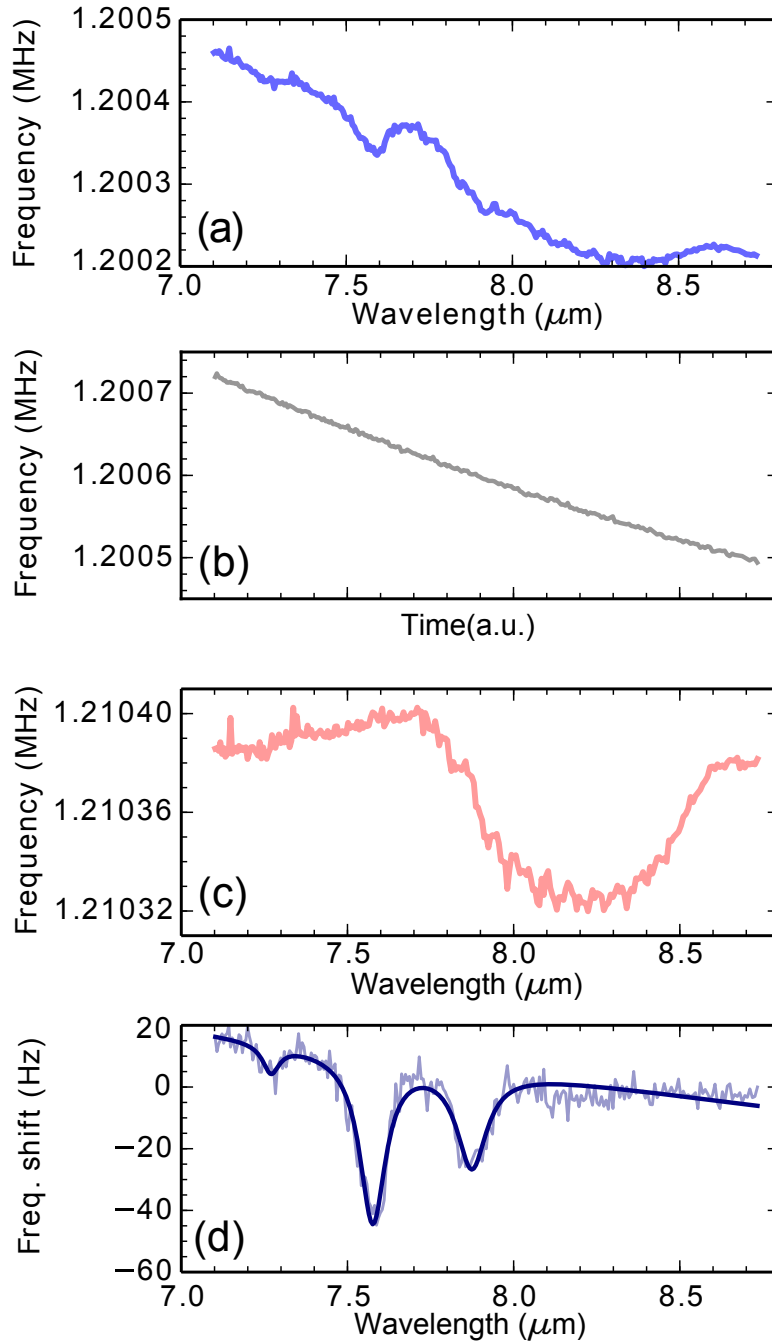


Figure 7.4: The mechanical resonance frequency extracted from the power spectral density (PSD) function. (a) The frequency variation as a function of infrared wavelength for the first mode of a 215 μm long string with 2.72 μg RDX on the string. (b) The background frequency variation of the string (without shining IR laser) for the corresponding sweeping time of (a). (c) The baseline frequency variation from the silicon nitride (without RDX) as a function of infrared wavelength. (d) The photothermal signal from RDX only (light blue), after background subtraction. The dark blue curve is a multi-peak Lorentzian fit to the data.

signal-to-noise data sets.

In addition to revealing RDX photothermal peaks, it is also possible to calibrate the mass of the RDX on the string. The deposited or desorbed RDX can be estimated by $\delta m_{\text{eff}} = 2m_{\text{eff}}(\delta f/f)$. Here m_{eff} is the effective mass of the mechanical resonator, which depends on the mode shape [30]. Note that for a string the effective mass is simply one half the geometric mass [30]. Fig.7.4(b) shows the frequency shift (due to RDX desorption) during the data acquisition. This frequency shift can be converted to the mass of desorbed RDX achieved that time. It is also possible to extract the remaining RDX on the string once the frequency shift is measured from the base frequency (just before the RDX deposition on the string). All masses reported represent the effective mass at the mid point of the data set, and the error bars represent the variation in mass during data acquisition.

7.3 Photothermal Spectroscopy

In this experiment, the sublimation of RDX is a slow process, typically only $\sim 10\%$ of the adsorbed mass is sublimated from the nanostring during data acquisition time. Our data acquisition protocol takes only sixteen minutes, eight for the wavelength scan and eight for the background control scan. Therefore we can perform experiments continuously as the RDX mass on the nanostring is decreased smoothly. A series of these photothermal spectroscopy scans as a function of RDX on the nanostring is shown in Figure 3. As the RDX is pumped away, the peaks gradually decrease until they begin to disappear into the noise. In this data set the smallest peaks are from 1.01 ± 0.04 pg of RDX, although the signal-to-noise ratio remains good for this small mass.

The experiment is repeated with different nanostrings of varying length. We have found that the magnitude of the photothermal frequency shift does not depend on nanostring length. This is expected from the work of Yamada *et al.* [63] since the power adsorbed by a vibrational mode is

$$P = \delta f \frac{32\kappa A \sqrt{\sigma \rho}}{n\alpha E}. \quad (7.1)$$

Here ρ is the density, σ is the tensile stress, E is the Young's modulus, α is the thermal expansion coefficient, κ is the thermal conductivity, δf is the observed

frequency shift, A is the cross-sectional area of the nanostring, and n is the mode number. The material properties of silicon nitride are used from previously reported values [70]. While the observed frequency shift depends on the mode number, as observed in Fig. 7.5, the power absorbed does not, and therefore our photothermal signal to noise ratio does not depend on mode number. We also observe in Eq .7.1, for a constant power, δf depends only on the cross sectional area A of the string.

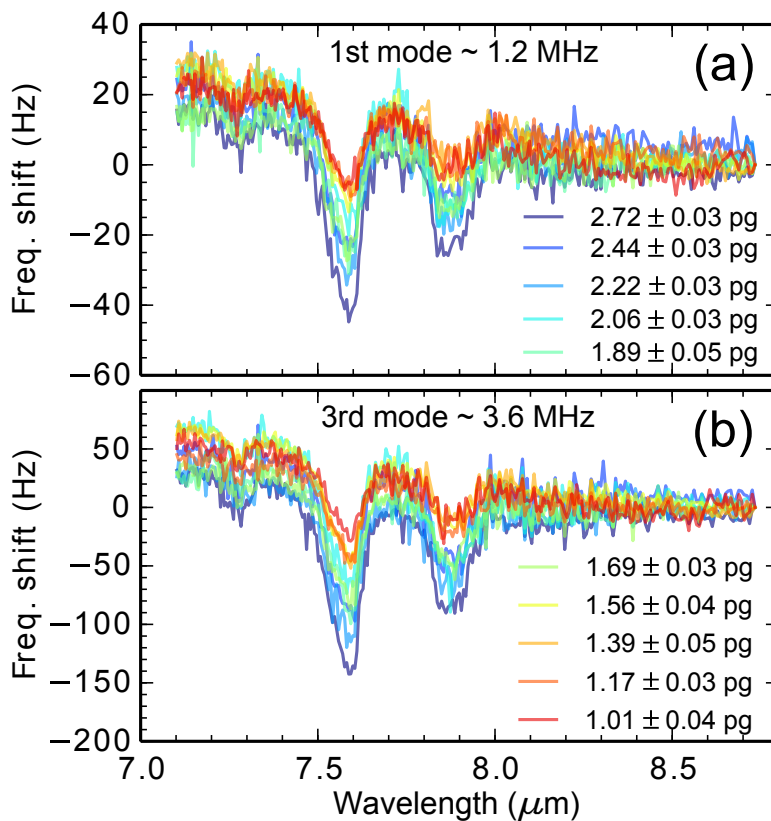


Figure 7.5: The frequency shifts due to the RDX photothermal effect on the string for the first (a) and third mode (b). The corresponding background and baseline frequency traces are subtracted to get each trace in these plots. The data is taken from a 215 μm long string.

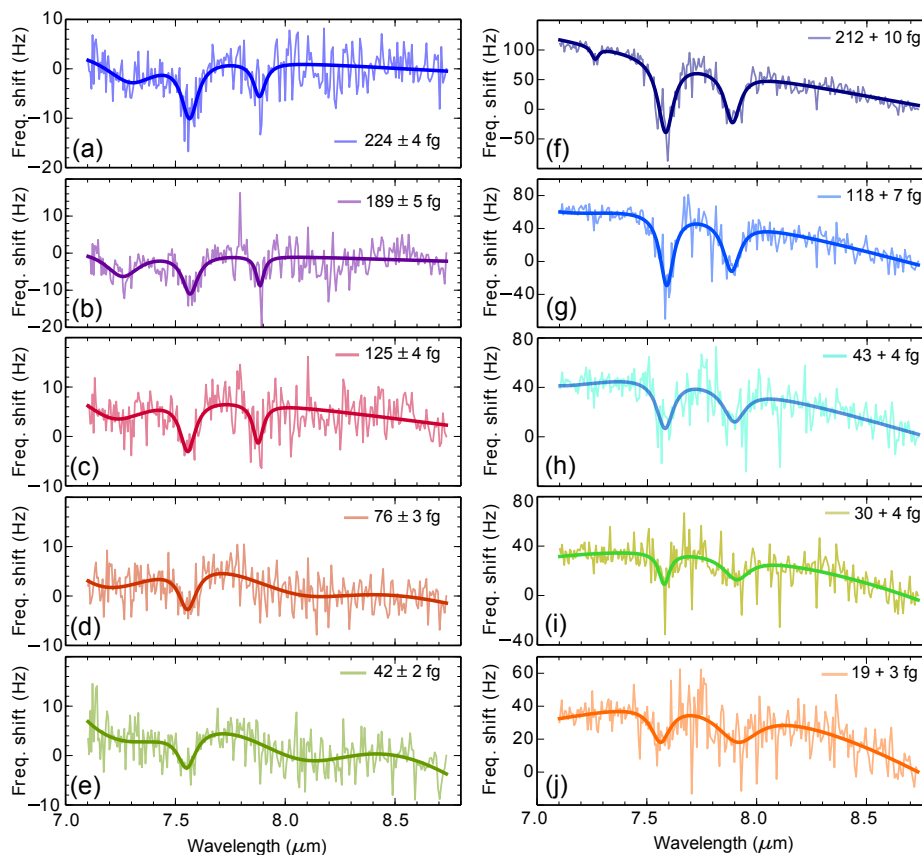


Figure 7.6: Data from (a–e) 174 μm long and 2 μm wide string, and (f–j) 150 μm long and 500 nm wide string, with small initial RDX deposition. The data is fit with an automated multi-peak Lorentzian fit, which helps to reveal the RDX adsorption peaks.

7.4 Lowest RDX detection by photothermal spectroscopy

In order to explore the ultimate limits of the optically detected silicon nitride nanostrings, we performed a similar set of experiments to that described above, but beginning with a smaller amount of RDX deposited on the device. As can be seen in Fig. 7.6(a), the initial mass of RDX deposited on the 174 μm long string was only 224 ± 4 fg. Yet with this small amount of target molecule we can still resolve the three spectroscopic peaks seen with higher masses, and the fitting function has no trouble separating the peaks from the noise. At 125 ± 4 fg (Fig. 7.6(b)) on the

nanostiring we have lost most of the signal at $7.2 \mu\text{m}$, yet the peaks at 7.55 and $7.9 \mu\text{m}$ are observable. At the lowest masses of 76 ± 3 and 42 ± 2 fg (Fig. 7.6(d-e)), we are only able to clearly resolve one peak - that is the peak at $7.55 \mu\text{m}$.

In contrast, Fig. 7.6(f) shows that the initial mass of the RDX on the $150 \mu\text{m}$ long and 500 nm wide string was only 117 fg and with this small amount of RDX, we are able to resolve three spectroscopic peaks. Moreover, at least two peaks are observable at the lowest mass of 18 fg on the string. Interestingly, this lowest mass is already ~ 2 times lower than previous one. This proves that the narrow string has better resolution. It was difficult to measure any string narrower than 500 nm in our system. So we could not go further below to test it. It is worth noting that the minimum resolvable mass using photothermal spectroscopy is significantly higher than using mass desorption alone. From measurements of the Allan deviation we have previously shown that these devices have a minimum detectable mass of 1.8 attograms in Chapter 6.

In Fig. 7.7 we show the peak power absorbed, as given by equation 1, for the photothermal peak at $7.55 \mu\text{m}$ as a function of mass on the string. As can be seen, the trend is reasonably linear with the difference between the different strings arising from variations in their cross-sectional area. The thickness of each individual string is 250 nm . However the widths are different for different length of the strings due to the tolerance of the fabrication process (these are 2.56 , 2.8 , 2.05 and $2.83 \mu\text{m}$ for 215 , 200 , 174 and $100 \mu\text{m}$ long strings). We note that optimizing the nanostiring design is best accomplished through minimizing the cross-sectional area. This could be accomplished with thinner starting materials (here we use 250 nm thick silicon nitride [10]). Or narrower nanostirings can be fabricated with electron-beam lithography, as opposed to optical lithography, but they become more difficult to measure using optical interference. Instead, it may be useful to integrate alternate detection schemes, such as electrical [71, 72, 73] or optomechanical [74, 75, 76, 77, 78] readout, to measure such nanostirings. In addition, the system we have demonstrated here can be extended to multiple adsorbed molecules, either directly through differentiation of the molecular IR signature [79] or through the use of arrays of nanostirings to detect molecules adsorbed to different strings in the array [65].

Our goal was to show one of the potential applications of our silicon nitride nanostirings. In this Chapter, we have successfully shown that explosive molecules RDX

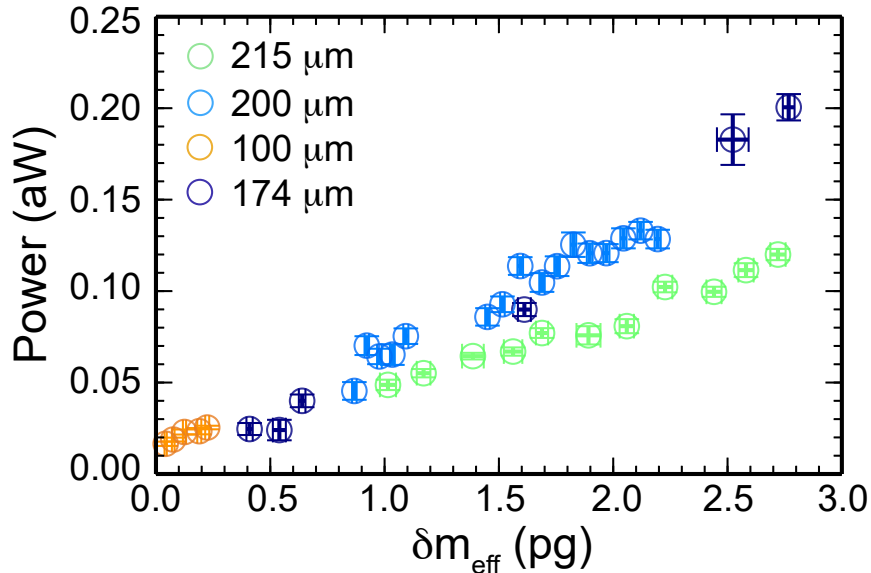


Figure 7.7: Power absorbed at $7.55 \mu\text{m}$ as a function of RDX mass adsorbed on a string. We show four different strings of 215, 200, 174 and 100 μm lengths, with 2.78, 2.2, 0.224 and 2.8 pg initial amounts of RDX deposited. They all follow a linear trend, with small differences due to varying cross-sectional areas of the strings. Error bars for power are from the Lorentzian fit to the data, and the error bars in mass are due to the variation during data acquisition.

can be detected by our nanostring using a second detection technique, photothermal spectroscopy in our case. We have demonstrated the lowest quantity of molecules adsorbed to a mechanical resonator ever directly measured by photothermal spectroscopy, down to $42 \pm 2 \text{ fg}$ - corresponding to just 190 attomoles (or 110×10^6 molecules) of RDX.

However it is difficult to determine the constant of proportionality between the amount of mass added to a resonator and the change in resonance frequency of the resonator which reveals the detection of adsorbed mass in terms of ‘effective mass’. This limitation is a major impediment to high-accuracy nanomechanical mass sensing. In next Chapter, we will introduce a multi-mode analysis expecting to provide better accuracy in mass sensing.

CHAPTER 8

Time Resolved Mass Sensing by Nanomechanical Strings ¹

In Chapter 7, we discussed the detection of RDX by our nanostrings. It is reported that the RDX formed nano-crystals during deposition and densely adsorbed on the string. It is also noticed that there is a slow sublimation of RDX over time due to the vacuum pressure. However, it is possible to track the multiple resonance frequencies over the time for a resonator. Therefore, it will be interesting to perform multi-mode analysis to obtain better accuracy in mass sensing. In addition, it is expected to have instantaneous mass profiles along a device from its time evolution resonance frequencies.

8.1 Relationship between frequency response and mass distribution

In this Chapter, it is shown that the particular distribution of mass deposited on the surface of a nanomechanical resonator can be estimated by tracking the evolution of the devices's resonance frequencies during the process of desorption. It has been shown that multimode response of the system enables mass sensing at much higher levels of accuracy than is typically achieved with a single frequency-shift measurement. In addition this multimode analysis provides an adequate mass profile along the string.

¹A version of this section has been published. Biswas *et al.*, *Phys. Rev. Applied.* **3**, 064002 (2015).

Nanomechanical resonators are highly sensitive to added mass [80, 81, 82, 83] due to the accuracy in measurement of their mechanical frequencies. Mass adsorbed at the scale of femtograms or smaller are detectable as shifts in the resonance frequencies [84, 85, 86] of a resonator of tens or hundreds of picograms. Although it is not always straight forward to determine the relationship between the change in resonance frequency and the added mass to a resonator. The constant of proportionality is easy to compute for a uniform distribution of added mass. In fact, it is given by the ratio of the resonator's mode-specific 'effective mass' to its true inertial mass [30]. However the distribution is of arbitrary form and more or less unknown in a typical sensing application. In that case, there is no reliable way to extract the total adsorbed mass from frequency shift measurements [55], except at the level of an order-of-magnitude estimate.

Efforts have been made to avoid this problem by mass adsorption to specific sites on a device through complex fabrication [87]. Multimode measurements [56, 88, 89, 90, 91] is an alternative approach, which provide some degree of spatial resolution. The simplest example is that both the size and location of a *point mass*—situated along a resonator with extent primarily in one dimension—can be determined from a simultaneous measurement of two resonance frequency shifts [92, 1, 93]. The original experiment to determine mass and location of a point particle was performed by Dohn *et al.* on cantilevers [92]. Later, it was shown that the sinusoidal mode shapes characteristic of nanomechanical strings simplify the analysis [1].

In a previous study on nanostrings, real-time mass sensing was mimicked by carrying out sequential frequency shift measurements of the first two harmonics in conjunction with pick-and-place deposition of a single micro-particle [1]. In our work, genuine real-time observations are made: we measure the first, third, and fifth harmonics (for the longest device) simultaneously as a function of time while mass sublimates from the device surface. This is possible because all these odd modes are resolved using optical interferometry at the midpoint of the string with the device entirely under thermomechanical actuation. It is shown that measurements of any pair of modes reveal not only the instantaneous total mass of molecules adsorbed but also their distribution—at least in the regime where the distribution is smooth, slowly varying, and roughly symmetric about the resonator midpoint.

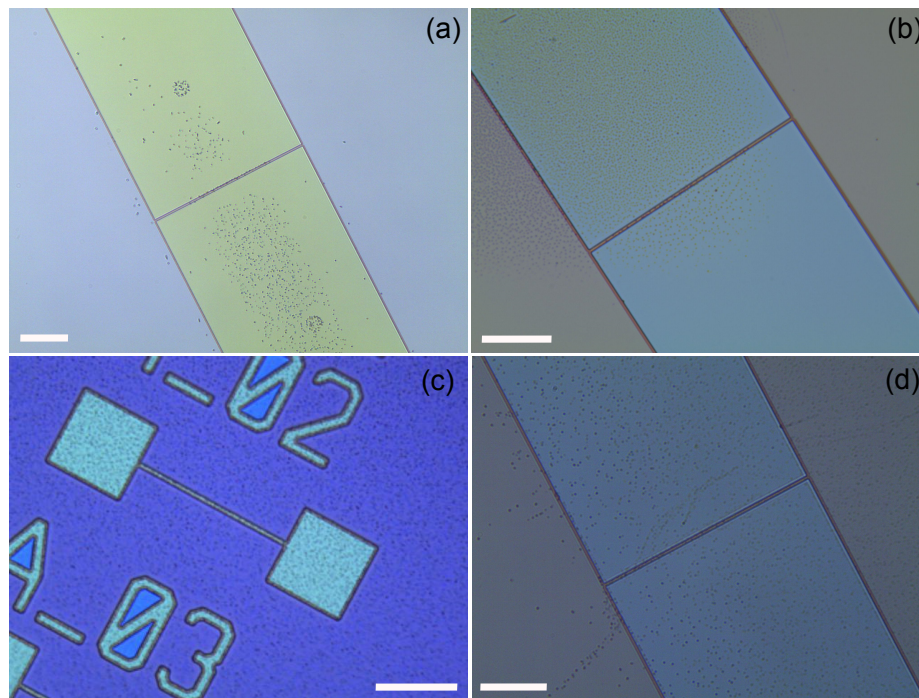


Figure 8.1: Optical microscope images show a $101.7 \mu\text{m}$ nanostring with a large number of RDX crystallites physisorbed onto the device surfaces. (a), (b), and (d), show various RDX mass profiles along the string and (c) shows unbiased mass profile onto the string.

8.2 Experimental method

The nanomechanical resonators under study are fabricated from high-stress silicon nitride materials using standard optical lithography and subsequent process. The details are given in Chapter 3. These devices are 250 nm thick, $2\text{--}3 \mu\text{m}$ wide and $100\text{--}300 \mu\text{m}$ long. RDX molecules are adsorbed onto the nanostring by vapor deposition technique as described in Chapter 7. Fig 8.1 shows both biased and unbiased RDX profiles along the string. A mask has been used, at different positions around the midpoint of the string, to get various mass profiles along the string. In addition, no mask is used for an unbiased RDX deposition onto the string. It is observed that the RDX preferentially adsorbs onto the silicon nitride and aggregates in clusters. Measurements are performed using optical interferometry technique which is described in Chapter 4. The red laser is focused at the center of the

nanostings so that their odd harmonics [30] can be measured conveniently without disturbing the system. The laser power incident on the string is no more than 120 μW . The weak thermal actuation of the string has no effect on where the RDX settles.

A high frequency Zurich lock-in amplifier (model HF2LL, capable of demodulating as many as six independent frequencies) is used to isolate up to three harmonics that have large thermomechanical displacement at the device midpoint. We track these harmonics as a function of time in order to extract useful information about the distribution of mass on the device surface and about the characteristics of the RDX sublimation process. In practice, the continuous time trace of the optical interferometry measurement, $z(t)$, is used to generate a power spectral density (PSD),

$$S(\omega; t) = \frac{1}{T} \int_0^T d\tau e^{i\omega\tau} \int_{t-T}^{t-\tau} z(\tau') z(\tau' + \tau), \quad (8.1)$$

computed over a sliding time window of duration $T \approx 0.85$ s. The “instantaneous” resonance frequency $\omega_n(t)$ is obtained at each time t by fitting the PSD in the vicinity of its n th peak to the usual (nearly-Lorentzian) damped harmonic oscillator lineshape, $S(\omega; t) = A_n \omega_n(t) / [(\omega_n(t)^2 - \omega^2)^2 + (\omega \omega_n(t) / Q_n)^2]$, with the quality factor Q_n and the overall amplitude A_n also optimized as part of the fit [10, 30]. This analysis is simple enough that it can be done concurrently with the data acquisition.

The initial resonance frequency of each string is measured before any deposition. The RDX is deposited onto each string in an individual run. The string is then mounted back into the chamber immediately after the deposition. Since the vacuum results in a slow sublimation of RDX, the frequency of the string changes over time. The frequencies for the first, third, and fifth (only for the longest string) harmonics of a string, are simultaneously measured over time during the experiment. Fig. 8.2 shows the change of relative frequency shift as a function of time for three different length of strings. The length of the longest string is 309.49 μm and hence we are capable of resolving the resonance frequency up to the fifth mode of the string. Its worth noting that all these measurements are performed under thermomechanical actuation. Offsets are added to the higher mode relative frequency shifts for clear view in Fig. 8.2. Eventually, all these devices regain their initial state after long period of time – clean device without any RDX on it. This regain time of a device solely depends on the amount of initial RDX deposition assuming the rate of vacuum

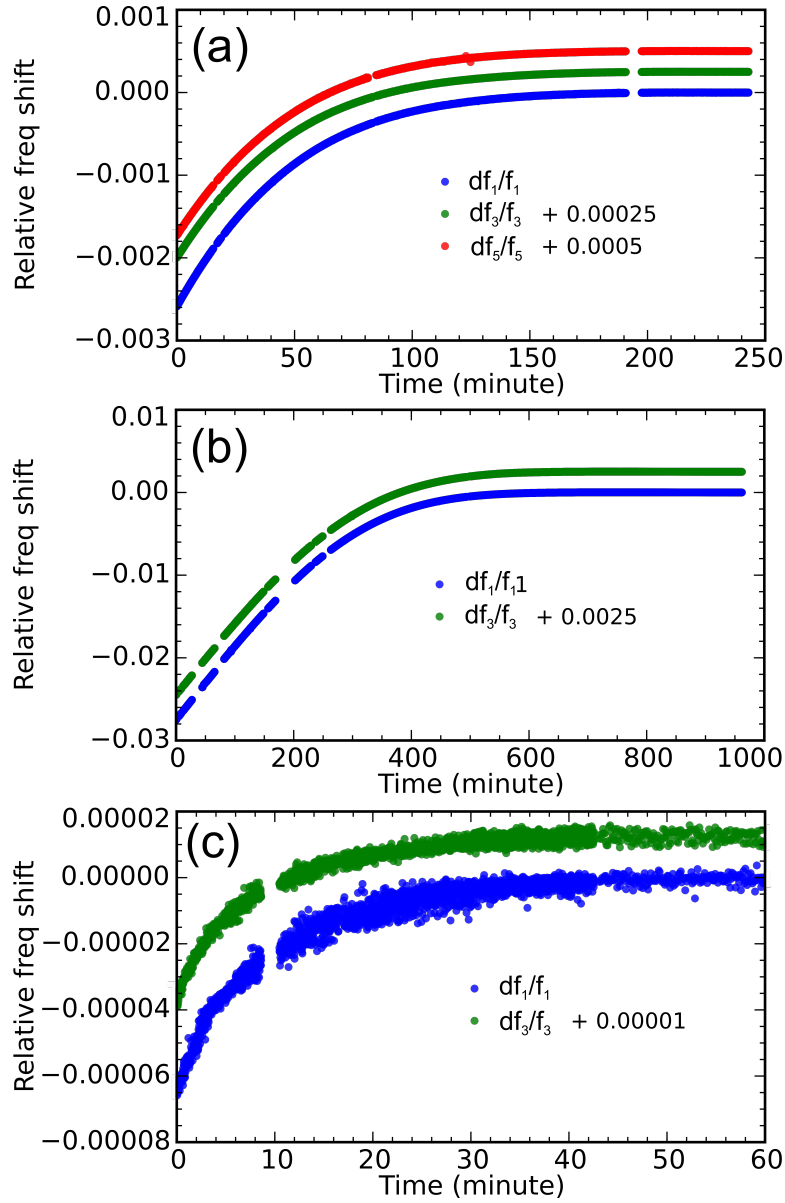


Figure 8.2: Multimode relative frequency shifts as a function of elapsed time from (a) 309.49 μm , (b) 101.07 μm , and (c) 172.60 μm long string. The initial deposited RDX amounts are 2.85, 11.8 and 0.028 μg for 309.49, 101.07, and 172.60 μm long string respectively. For visual clarity, the mode 3 and mode 5 data sets are translated upward by some arbitrary numbers.

of the chamber remains constant.

It is easy to estimate the effective mass of the adsorbed RDX at a particular time by knowing the frequency shift of a particular mode frequency. But the effective mass is mode dependent and it strongly depends on the distribution of the adsorbed mass onto the string. So the estimation of adsorbed mass in terms of effective mass is not trustworthy for an arbitrary distribution. In our system, since it is possible to track more than one harmonic frequency hence this gives us opportunity to do multimode analysis and results better accuracy in mass sensing.

Let us consider an unperturbed string which has a uniform mass distribution $\mu(x) = M/L$. A small mass perturbation, onto the string, leads to a modified mass distribution $\mu(x) \rightarrow \mu(x) + \delta\mu(x)$ and a corresponding frequency shift $\omega_n \rightarrow \omega_n + \delta\omega_n$. The relationship between the frequency shift and perturbed mass can be expressed as,

$$-\frac{\delta\omega_n}{\omega_n} = \frac{1}{M} \int_0^L dx \delta\mu(x) \sin^2\left(\frac{n\pi x}{L}\right). \quad (8.2)$$

For a perfectly flat mass distribution profile, with $\delta\mu(x) = m/L$ leading to

$$-\frac{\delta\omega_n}{\omega_n} = \frac{m}{2M}, \quad (8.3)$$

the mass added (m) can be determined from a *single* frequency shift measurement in any mode. A strongly peaked profile represents the extreme opposite case. A point mass deposited with $\delta\mu(x) = m\delta(x - x_m)$ leads to

$$-\frac{\delta\omega_n}{\omega_n} = \frac{m}{M} \sin^2\left(\frac{n\pi x_m}{L}\right), \quad (8.4)$$

and hence the mass added (m) and its position (x_m) must be determined from *two* frequency shift measurements in any pair of modes: specifically,

$$-\frac{m}{M} = \frac{\delta\omega_1}{\omega_1} \left(\frac{3}{4} \pm \frac{1}{4} \sqrt{\frac{\delta\omega_3/\omega_3}{\delta\omega_1/\omega_1}} \right)^{-1}, \quad (8.5)$$

$$x_m = \frac{L}{\pi} \arcsin \left(\frac{3}{4} \pm \frac{1}{4} \sqrt{\frac{\delta\omega_3/\omega_3}{\delta\omega_1/\omega_1}} \right)^{1/2} \quad (8.6)$$

for modes 1 and 3. The detailed derivation of these analytical expressions can be found in Chapter 2.

The general mass-sensing problem, however, is much more difficult than either of these two limits. As it is seen in Fig 8.1, deposited RDX does not make any uniform thin film coated over the string. It forms nanocrystals and spreads over the string in arbitrary distribution. So the constant of proportionality in the relationship $\delta\omega_n/\omega_n \propto m/M$ is undetermined, and there is no way to recover an arbitrary mass profile $\delta\mu(x)$, except from an infinite number of error-free frequency shift measurements.

8.3 Two-parameter mass distribution ansatz

A simple two-parameter model has been proposed [94] to represent the distribution of mass deposited on the string:

$$\delta\mu(x) = \frac{m_0}{L} + \frac{\pi m_1}{2L} \sin\left(\frac{\pi x}{L}\right). \quad (8.7)$$

Here two assumptions are made on the distribution of mass. They are (i) the mass distribution is symmetric under reflection about the midpoint of the string and (ii) the mass distribution is smooth and slowly varying enough that it can be approximated by one component that is uniform across the string and another that places mass preferentially toward (or away from, when $m_1 < 0$) its center. m_0 and m_1 have units of mass, and the total mass sitting on the string is

$$\int_0^L dx \delta\mu(x) = \frac{m_0}{L} L + \frac{\pi m_1}{2L} \frac{2L}{\pi} = m_0 + m_1 \equiv m. \quad (8.8)$$

Here m_0 is nonnegative, but m_1 may be of either sign. $m_1 > 0$ describes a convex mass distribution, whereas $-2m_0/\pi < m_1 < 0$ describes a concave one. The lower bound on m_1 , which follows from $\delta\mu(L/2) \sim m_0 + \pi m_1/2 > 0$, ensures that the mass distribution remains everywhere nonnegative.

Length	Width	M	Trial	δf_1	δf_3	m_0/M	m_1/M	$m = m_0 + m_1$	m_u	m_u/m
(μm)	(μm)	(pg)		(kHz)	(kHz)			(pg)	(pg)	
101.07 [†]	2.83	218	1	-	-	0.051	0.0034	11.8	12.0	1.02
172.60	2.05	270	1	71.08 -0.10	210.51 -0.24	9.56× 10 ⁻⁶	93.7× 10 ⁻⁶	0.028	0.036	1.30
			2	-1.71	-	0.014	-	1.41	0.62	0.44
			3	-	11.10	0.036	0.009	5.99	4.73	0.79
			4	13.05 -2.11	48.87 -7.75	0.006	0.014 -	0.947	0.76	0.81
216.34	2.56	422	1	-9.89	-	0.008	0.006	6.05	6.90	1.14
309.49	2.72	642	1	-2.16	26.32 -5.64	0.002	0.002	2.85	3.33	1.17

Table 8.1: Results of a sequence of RDX depositions onto nanostrings spanning four different geometries, organized by string length and deposition trial. The dagger ([†]) marks the one experiment in which the RDX deposition process was completely unbiased; the others involved some degree of masking in order to engineer a nonuniform mass distribution.

Putting Eq. 8.7 into Eq. 8.2, the frequency shift becomes for the first mode,

$$\begin{aligned}
-\frac{\delta\omega_1}{\omega_1} &= \frac{1}{M} \int_0^L dx \left[\frac{m_0}{L} + \frac{\pi m_1}{2L} \sin\left(\frac{\pi x}{L}\right) \right] \sin^2\left(\frac{\pi x}{L}\right) \\
&= \frac{1}{M} \left[\frac{m_0}{L} \int_0^L dx \sin^2\left(\frac{\pi x}{L}\right) + \frac{\pi m_1}{2L} \int_0^L dx \sin^3\left(\frac{\pi x}{L}\right) \right] \\
&= \frac{1}{M} \left[\frac{m_0}{L} \frac{L}{2} + \frac{\pi m_1}{2L} \frac{4L}{3\pi} \right] \\
-\frac{\delta\omega_1}{\omega_1} &= \frac{1}{M} \left(\frac{m_0}{2} + \frac{2m_1}{3} \right). \tag{8.9}
\end{aligned}$$

For the 2nd mode, the frequency shift becomes

$$\begin{aligned}
-\frac{\delta\omega_2}{\omega_2} &= \frac{1}{M} \int_0^L dx \left[\frac{m_0}{L} + \frac{\pi m_1}{2L} \sin\left(\frac{\pi x}{L}\right) \right] \sin^2\left(\frac{2\pi x}{L}\right) \\
&= \frac{1}{M} \left[\frac{m_0}{L} \int_0^L dx \sin^2\left(\frac{2\pi x}{L}\right) + \frac{\pi m_1}{2L} \int_0^L dx \sin\left(\frac{\pi x}{L}\right) \sin^2\left(\frac{2\pi x}{L}\right) \right] \\
&= \frac{1}{M} \left[\frac{m_0}{L} \frac{L}{2} + \frac{\pi m_1}{2L} \frac{16L}{15\pi} \right] \\
-\frac{\delta\omega_2}{\omega_2} &= \frac{1}{M} \left(\frac{m_0}{2} + \frac{8m_1}{25} \right). \tag{8.10}
\end{aligned}$$

For the 3rd mode, the frequency shift becomes

$$\begin{aligned}
-\frac{\delta\omega_3}{\omega_3} &= \frac{1}{M} \int_0^L dx \left[\frac{m_0}{L} + \frac{\pi m_1}{2L} \sin\left(\frac{\pi x}{L}\right) \right] \sin^2\left(\frac{3\pi x}{L}\right) \\
&= \frac{1}{M} \left[\frac{m_0}{L} \int_0^L dx \sin^2\left(\frac{3\pi x}{L}\right) + \frac{\pi m_1}{2L} \int_0^L dx \sin\left(\frac{\pi x}{L}\right) \sin^2\left(\frac{3\pi x}{L}\right) \right] \\
&= \frac{1}{M} \left[\frac{m_0}{L} \frac{L}{2} + \frac{\pi m_1}{2L} \frac{36L}{35\pi} \right] \\
-\frac{\delta\omega_3}{\omega_3} &= \frac{1}{M} \left(\frac{m_0}{2} + \frac{18m_1}{35} \right). \tag{8.11}
\end{aligned}$$

Hence the general expression for the frequency shifts in the various modes can be expressed as,

$$-\frac{\delta\omega_n}{\omega_n} = \frac{1}{M} \left(\frac{m_0}{2} + \frac{2n^2 m_1}{4n^2 - 1} \right). \tag{8.12}$$

Inverting the relationship, we find that the values of m_0 and m_1 can be estimated from frequency-shift measurements on any pair of modes. For instance, in the case of modes 1 and 2 and modes 1 and 3, we find that

$$\frac{m_0}{M} = 8 \frac{\delta\omega_1}{\omega_1} - 10 \frac{\delta\omega_2}{\omega_2}, \quad \frac{m_1}{M} = \frac{15}{2} \left(\frac{\delta\omega_2}{\omega_2} - \frac{\delta\omega_1}{\omega_1} \right); \tag{8.13}$$

$$\frac{m_0}{M} = \frac{27}{4} \frac{\delta\omega_1}{\omega_1} - \frac{35}{4} \frac{\delta\omega_3}{\omega_3}, \quad \frac{m_1}{M} = \frac{105}{16} \left(\frac{\delta\omega_3}{\omega_3} - \frac{\delta\omega_1}{\omega_1} \right). \tag{8.14}$$

According to Eq. (8.12), higher modes (larger n) exhibit decreasing differentiation

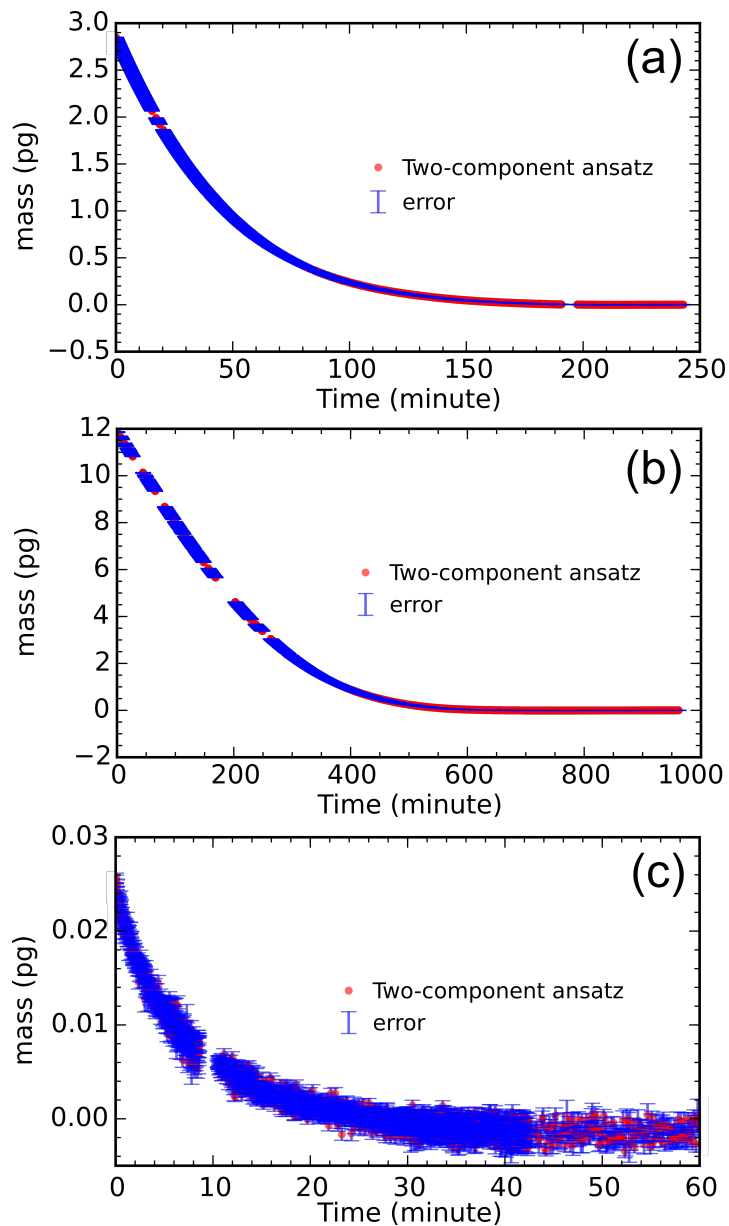


Figure 8.3: Figure shows the RDX mass extracted from the data presented in the Fig. 8.2 using the two-parameter model.

in the m_1 coefficient and so become less useful for distinguishing the components of the mass distribution: $-\delta\omega_n/\omega_n \rightarrow (m_0 + m_1)/2M$, independent of n , as $n \rightarrow \infty$.

A revealing, preliminary application of this style of analysis is provided in Table 8.1, where Eq. (8.14) has been utilized to characterize the mass distributed on seven nanostrings of four different lengths following various levels of RDX exposure. In each instance, the resonant frequencies of modes 1 and 3 are measured before and after RDX vapor deposition. The shifts in those frequencies after the mass deposition, δf_1 and δf_3 are reported in columns 5–6. M is the total pre-deposition mass inferred from the material density and device volume. We find that the estimates for m_1 exhibit both positive and negative sign (meaning convex and concave mass profiles), and in some cases show magnitude $|m_1|$ comparable to m_0 itself. This is evidence for a quite substantial variation in how RDX settles along the length of the string from one experiment to the next, and it confirms that a mass distribution close to uniform is only rarely the outcome of our sample preparation. Traditionally, one would use the shift of the first harmonic alone in conjunction with Eq. (8.3) to determine the adsorbed mass; we label this quantity m_u , since it is based on the assumption of a uniform mass distribution. Comparison of m_u with the corresponding value $m = m_0 + m_1$, coming from our improved two-component analysis, reveals that the two estimates can differ quite substantially. Fluctuations in the ratio m_u/m indicate that the traditional approach routinely over- or under-estimates the adsorbed mass in the range of 10% to 50%. This quantitative comparison is, as far as we know, the first of its kind, and it demonstrates the absolute importance of a multimode analysis for accurate mass sensing. The results in Table 8.1 are fully consistent with our intentional biasing of the vapor deposition process.

The preliminary results appearing in Table 8.1 are obtained from two discrete measurements of the devices' resonance frequencies, before and after RDX exposure. We have the capability, however, to make ongoing measurements of the resonance frequencies; these change continuously in time as the adsorbate molecules are removed from the nanostring because of the vacuum environment as shown in Fig. 8.2 . Using the result of two parameter model (Eq. 8.3), the instantaneous total adsorbed mass is estimated as,

$$\frac{m}{M} = \frac{m_0}{M} + \frac{m_1}{M} = 0.1875 \delta\omega_1/\omega_1 - 2.1875 \delta\omega_3/\omega_3 \quad (8.15)$$

and associated error is estimated as,

$$\Delta\left(\frac{m}{M}\right) = 0.1875 \Delta\left[\delta\omega_1/\omega_1\right] + 2.1875 \Delta\left[\delta\omega_3/\omega_3\right] \quad (8.16)$$

The variations of RDX mass over time are shown in Fig. 8.3 for three strings with different lengths. The deposited initial RDX amounts are substantially different from each other. But similar decay behaviors are observed in each case.

8.4 Sublimation model

It is nice to see that the two-parameter model can generate reliable mass extraction over the full period of time. Therefore, using this model the total amount of RDX mass onto a string can be extracted at any particular time. In addition, it is observed that the sublimation rate is not constant over time and follows an exponential decay profile. Hence it is interesting to explore the sublimation rate and exponential factor of the behavior. Moreover it is also interesting to find the RDX mass profile along the string at any instant of time. However, the two-parameter model itself is not sufficient enough to explore those facts. Since we have continuous multimode frequency so it is possible to sketch a time dependent sublimation model. The model was mainly developed by Prof. K.S.D. Beach, based on the experimental observations described in this Chapter. The sublimation model reveals the sublimation rate and the nature of sublimation of RDX. This model is also capable of producing a snapshot of the RDX mass profile along the string at any instant [94].

According to the sublimation model (details provided in Appendix D), the time dependent mass distribution along the string is

$$\delta\mu(x, t) = \left[\delta\mu(x, 0)^{1-\phi} - (1-\phi)\alpha\mu_*^{1-\phi}t \right]^{1/(1-\phi)}. \quad (8.17)$$

Here α is the sublimate rate from the string surface, ϕ is the exponential factor of mass sublimation, and t is the time at any instance after the vacuum starts.

Then the total mass can be estimated by the integration of the Eq. 8.17 as,

$$m(t) = \int_0^L dx \delta\mu(x, t), \quad (8.18)$$

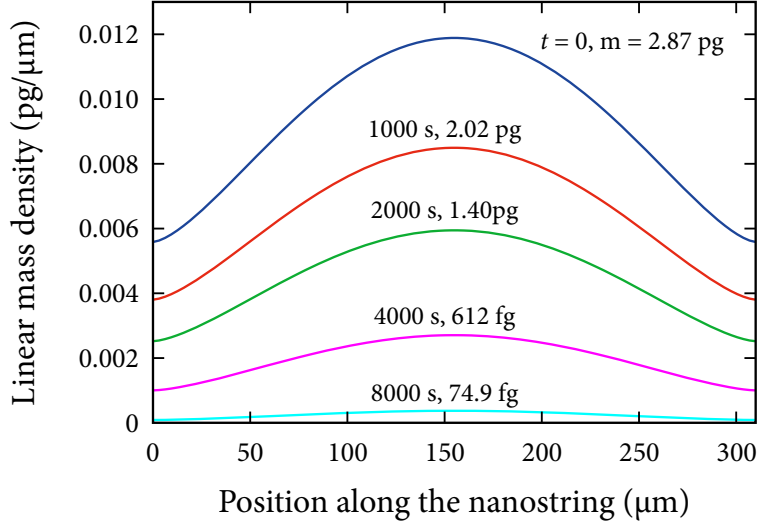


Figure 8.4: Profiles of the mass distributed along the nanostring of length 310 μm and mass 641.88 pg at representative moments in time.

and the time dependent relative frequency shifts expressed as,

$$-\frac{\delta\omega_n(t)}{\omega_n} = \frac{1}{M} \int_0^L dx \delta\mu(x, t) \sin^2\left(\frac{n\pi x}{L}\right). \quad (8.19)$$

Eq. 8.18 was solved numerically by Prof. K.S.D. Beach. The mass profiles along the string at a few instances are shown in Fig. 8.4 for the longest string (310 μm long). Such a determination of the real-time mass distribution may have important applications, such as the study of diffusion of molecules along the surface [95], or atomic layer reconstruction [96], of a nanomechanical resonator.

Fig. 8.5 indicates the effective instantaneous decay rate. One can see clearly that the rate is not constant in time—and hence it's incompatible with pure exponential decay. Rather, it seems to increase steadily. Moreover, between 8000 s and 11000 s, it turns up in a way that is consistent with the fractional power of ϕ . It is worth reiterating that this implies that sublimation occurs from the surface of crystallites—and not uniformly from the surface of the device—in agreement with optical and atomic force microscopy images shown in Chapter 7.

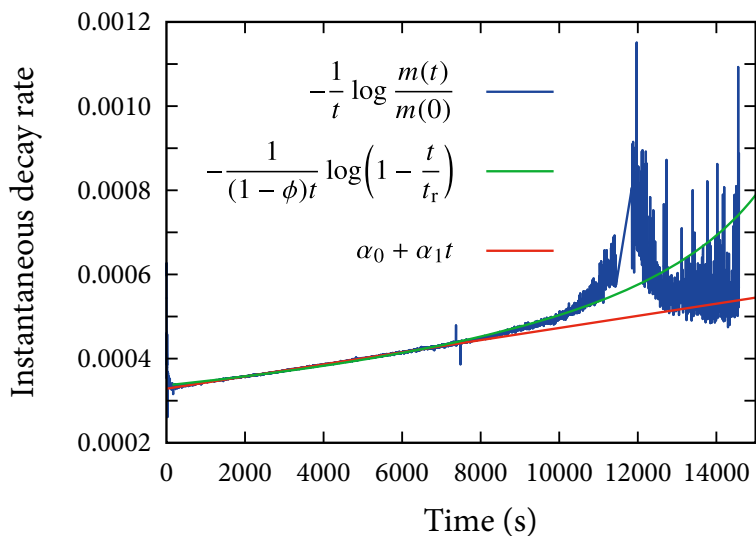


Figure 8.5: The instantaneous rate at which RDX desorbs from the nanos-tring clearly increases over time. A linear fit over the time interval [250 s, 7750 s] produces $\alpha(t) = \alpha_0 + \alpha_1 t = 0.00032865(6) + 1.445(1) \times t$.

In Chapter 7, we have shown the lowest amount of RDX detection in terms of “effective mass”. In this Chapter it is found that the “effective mass” is not always trustworthy to determine exact amount of adsorbed mass for a non-uniform mass distribution. Therefore multi-mode analysis and sublimation model are applied to find better accuracy for a non-uniform mass distribution.

CHAPTER 9

High Q gold and silicon nitride bilayer nanostring ¹

In the last two Chapters, we found that we were able to explore molecular sensing with our nanostrings, mainly due to the fact that the explosive molecule RDX is “sticky” and it adsorbs to the silicon nitride surface. Generally molecules will not stick to our silicon nitride nanostrings. Therefore, we need to add an intermediate layer for functionalization. This is often achieved by adding gold on a resonator surface [97]. Addition of gold might reduced the Q of a resonator [98], resulting in degradation of sensor performance. Instead in this chapter, it is shown that a metallic layer (gold in our case) can be deposited on the top of a bare silicon nitride nanostring without destroying its quality factor for the fundamental mode. Instead the device retains its mechanical responsiveness while gaining sensitivity to molecular bonding. Alternatively, dissipation can be circumvented by depositing only in areas that do not become stressed upon actuation [99, 100]. Furthermore, differences in thermal expansion within the bilayer causes internal stresses that can be electrically controlled. In particular, an alternating current (AC) excites resonant motion of the nanostring.

9.1 Addition of gold on top of silicon nitride string

Though silicon nitride nanostrings [2, 3] have many applications, they are unfortunately not very good candidates for universal molecular sensing applications [24, 25]

¹A version of this section has been published in Applied Physics Letters. Biswas *et al.*, *Appl. Phys. Lett.* **101**, 093105 (2012).

due to inert nature of silicon nitride. They should have a chemically functionalizable surface that allows them to be used as a chemical sensor. In most cases, the silicon and silicon nitride resonators are coated with gold to make them chemically functionalizable. Then a molecule of choice can be affixed to the gold overlayer, attached by way of a thiol intermediary [26, 27]. The addition of the gold has no adverse consequences for static, stress-response measurements [101].

We have found that the Q of the fundamental frequency is not adversely affected by a relatively thick metallic layer (53 nm) on top of our silicon nitride nanostrings (250 nm thick), even though it nearly doubles the total mass of the string. However, Q s associated with higher harmonics are reduced to lower values compared to the bare silicon nitride nanostrings. This indicates that the dissipation mechanism is different for a metal coated string for which the bulk bending is the dominant mechanism.

In addition, differing thermal expansion coefficients of the gold and silicon nitride layers make the strings sensitive to temperature [102, 103, 104]. While this could prove useful in temperature sensing or provide an independent measurement of the resonator temperature, our focus lies elsewhere. In particular, we demonstrate that it is possible not only to vary the temperature of the device electrically via direct current (DC) ohmic heating but also to actuate resonant motion via alternating

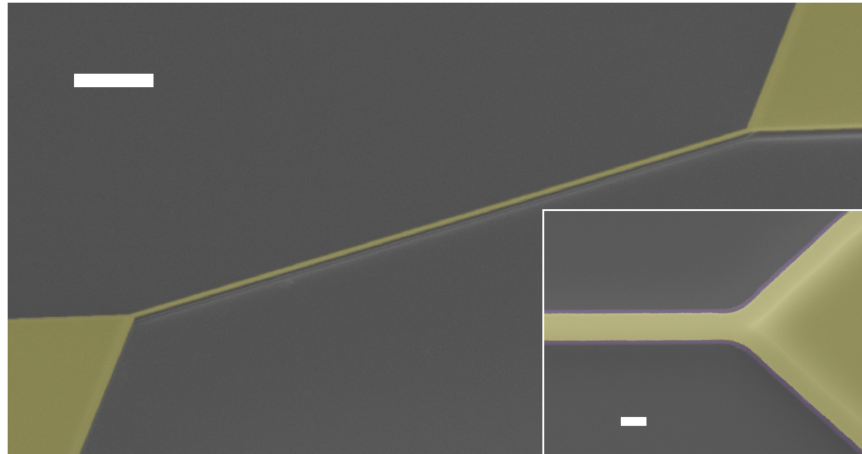


Figure 9.1: Scanning electron microscope (SEM) image of a 210 μm long gold and silicon nitride bilayer nanostring (scale bar 20 μm). The overhead view of the device is shown in inset (scale bar 2 μm).

current (AC) thermoelastic heating. The DC drive allows us to study the thermal properties of molecules affixed to a resonator [105, 106, 107, 108, 109]. The AC drive provides integrated actuation [110, 111, 112] and avoid the need for a piezoelectric buzzer or other external driving mechanism.

The fabrication started with stoichiometric silicon nitride (250 nm) deposited onto silicon dioxide (2 μm) on a silicon handle from Rogue Valley Microdevices. The wafer is sputtered with 10 nm chromium layer followed by 43 nm of gold layer. The detailed fabrication process is described in Chapter 3. The thin chromium layer served as an adhesive layer in between gold and silicon nitride layers. Hence, we refer this as a bilayer nanostring. The completed device is shown in Fig. 9.1. The string is 210 μm long, 2.75 μm wide and ≈ 305 nm thick. The gold is slightly over-etched, although this is not important since the string's normal modes are insensitive to the exact transverse dimensions.

Measurements are performed by optical interferometry using a 632.8 nm laser focused onto the nanostring, as described in Chapter 4. The nanostring is mounted into an optical access vacuum chamber as shown in Fig. 9.2(a). The temperature of the sample stage of this chamber can be controlled and accurately determined. Since the nanostring has a gold layer on top of silicon nitride, it is important to minimize any heating effects produced by absorption of the red laser. Though the system has the ability to generate a maximum laser power of 5 mW, the incident power on the device is 13 μW , which is below the onset of significant optical heating effects. The peak frequency and Q are determined by fitting to the characteristic power spectral density (PSD) [30] as discussed in Chapter 5. This analysis is appropriate regardless of the actuation method: thermomechanical, external piezoelectric, or integrated ohmic (thermoelastic). In addition, our optical system can be scanned using closed-loop piezo stages with respect to the sample [114], providing spatial maps of the amplitude and phase output by the Zurich lock-in as shown in Fig. 9.3 for a 210 μm long string. Mapping images of two adjacent pairs of out-of-plane and in-plane modes are presented here to show clear comparison. The left panel of each figure shows the spatial scan near the center of the string and the right panel of each figure presents simultaneous phase information at the same position. In the phase diagram, for a out-of-plane motion, there is no evidence of splitting rather it lies along the string's position. In contrast, for in-plane motion it shows splitting in phase images and they are followed by the edges of the string. In addition, since the

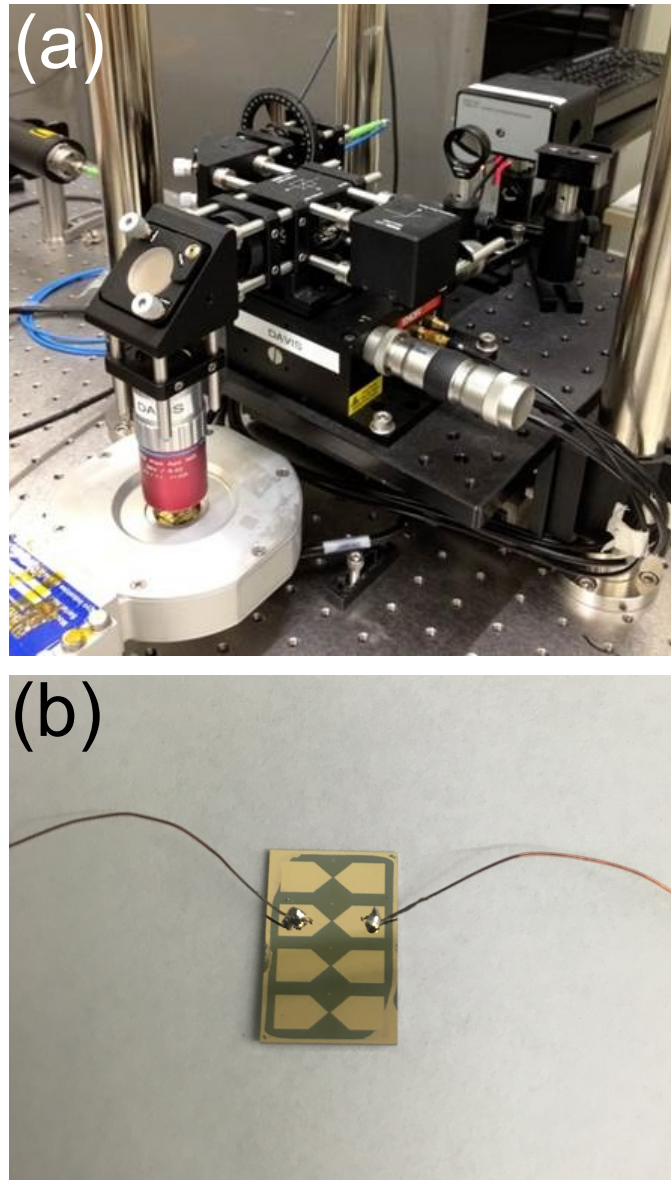


Figure 9.2: Optical image of the experimental setup.

measurement is performed in vacuum and the string's width is much larger than the string's thickness, the motion of the string in the out-of-plane direction requires less energy compared to the motion in the in-plane direction. This is also reflected in the associated Q values of each resonance frequency. Hence, we can unambiguously

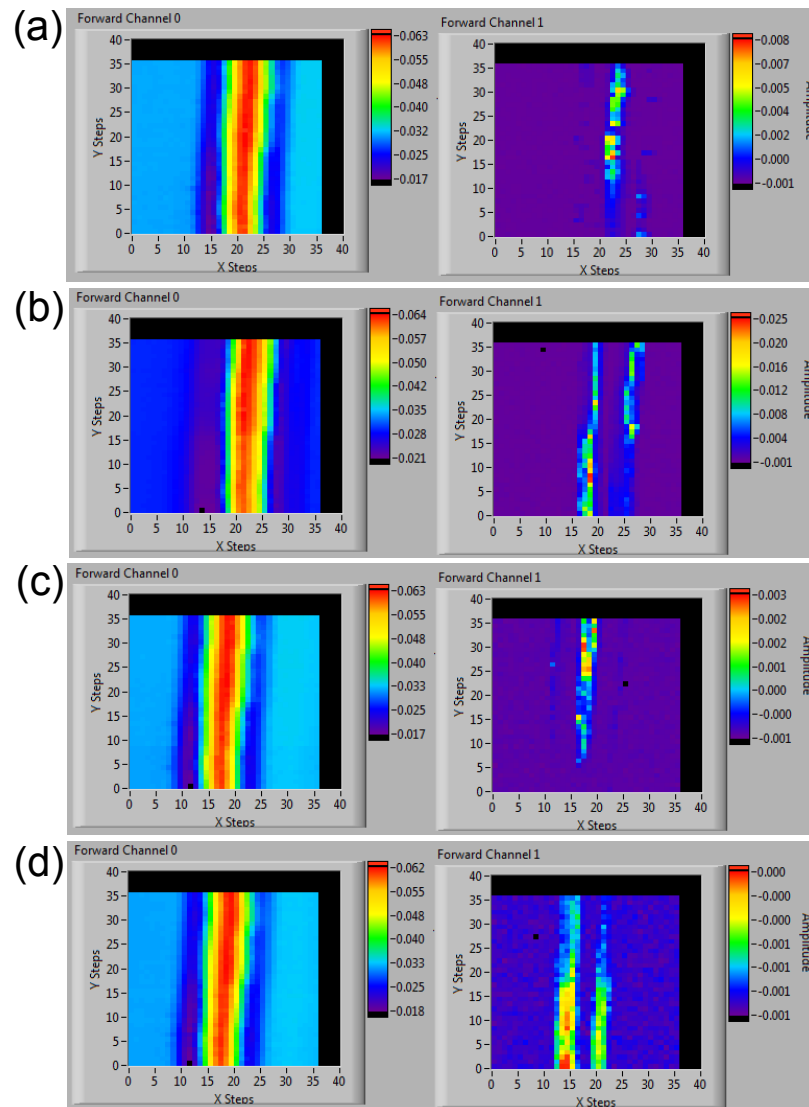


Figure 9.3: Spatial scan of amplitude and phase of a 210 μm long string for (a) 0.852 MHz, (b) 0.981 MHz, (c) 4.229 MHz, and (d) 4.729 MHz resonance frequencies.

distinguish between in-plane and out-of-plane motion.

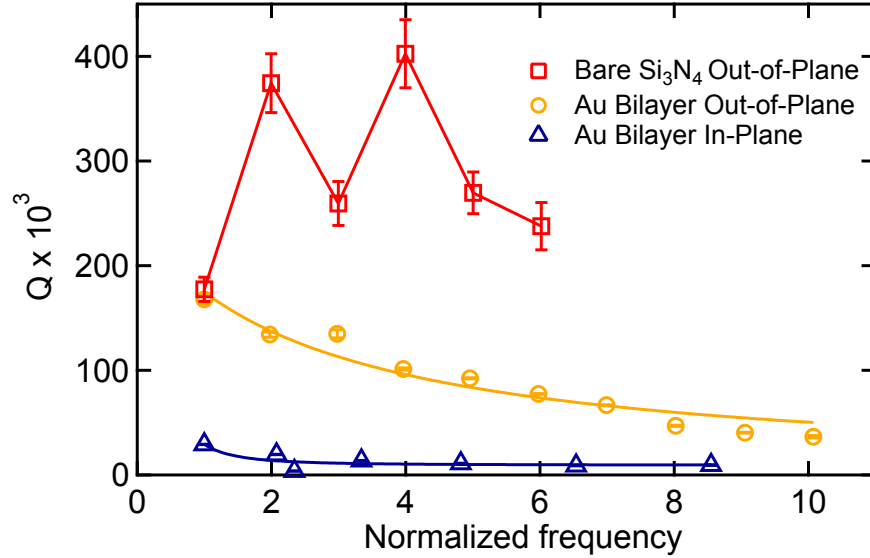


Figure 9.4: The Q variation with mode harmonics for the $210 \mu\text{m}$ long gold bilayer nanostring and a similar bare silicon nitride string. The orange circles are out-of-plane and purple triangles are in-plane Q s for the bilayer string and red squares are out-of-plane Q s for the bare string from Ref. [10]. Here the string is actuated using an external piezoelectric.

9.2 Dissipation in bi-layer nanostrings

The bilayer string is actuated by an external piezoelectric buzzer to get the interferometric signal from the string at the resonance frequency. This is because the thermomechanical actuation is not sufficient enough to be detected by low laser power ($13 \mu\text{W}$). The Q s are then extracted by fitting to the power spectral density [10] of the device and are shown in Fig. 9.4. These Q s are compared with the Q s of the out-of-plane modes of a uncoated silicon nitride nanostring with comparable geometry. It shows that the Q s of the fundamental out-of-plane mode of the bilayer nanostring are almost same to that of the uncoated string. I believe, this is mainly because of the geometry of supporting pads of these resonators. The shape of the supporting pads are triangular (Fig. 9.1) instead of square which could possibly play a vital role in dissipation mechanism.

On the other hand, the higher order modes are damped as compared to the bare string. Both bare and gold bilayer devices demonstrate the alternating even/odd

behavior previously seen for silicon nitride membranes [14] and nanostrings [10], which has been reported to originate from dissipation due to phonon tunneling [14]. However, the alternating even/odd behavior is in opposite phase for gold coated bilayer string with compared to the bare string. We need further investigation to understand this phenomenon properly. Aside from this oscillation, the Q of the bare device is essentially flat with respect to frequency (or, equivalently, mode number). The Q of the gold bilayer strings, however, decays with frequency. A key difference appears to be the high thermal conductivity of the metallic layer, which allows for efficient transport of energy from within the string (dissipated as a result of internal stresses during bulk bending) to the outside.

As discussed in Chapter 5, the Q varies by mode according to

$$Q_n = \frac{m\omega_n}{\gamma_n} \approx \frac{m}{\tilde{\gamma}^{\text{visc}}\omega_n^{-1} + \tilde{\gamma}^{\text{anchor}} + \tilde{\gamma}^{\text{bulk}}\omega_n}. \quad (9.1)$$

Here, viscous damping $\gamma_n^{\text{visc}} = \tilde{\gamma}^{\text{visc}}$, damping at anchor points $\gamma_n^{\text{anchor}} = \tilde{\gamma}^{\text{anchor}}\omega_n$, and damping due to bulk bending $\gamma_n^{\text{bulk}} = \tilde{\gamma}^{\text{bulk}}\omega_n^2$. The tilde decorated quantities are damping coefficients from which the leading order frequency dependence has been factored out. Since the experimental chamber is evacuated to $\approx 2 \times 10^{-6}$ torr, the viscous damping term, $\tilde{\gamma}^{\text{visc}}$, can be neglected [9]. In the case of the bare string, the Q s of higher modes are essentially flat except for an even/odd parity due to phonon tunnelling. This indicates that dissipation mostly comes from the bending at anchor points, and $\tilde{\gamma}^{\text{anchor}}$ is the overwhelmingly dominant contribution [10]. On the other hand, the Q s of higher modes for the bilayer nanostrings decay with increasing frequency. This confirms that the dominant dissipation mechanism is no longer localized at anchor points since the decaying tail can only be fit with a non-vanishing $\tilde{\gamma}^{\text{bulk}}$ term. We have found that $\omega_1\tilde{\gamma}^{\text{bulk}}/\tilde{\gamma}^{\text{anchor}} = 0.38 \pm 0.08$ from the out-of-plane data in Fig. 9.4(b).

9.3 Local and global heating of bi-layer nanostrings

In addition to the dissipation mechanism, the gold layer of our string makes it sensitive to temperature and optical power. In particular because of the access to the metallic overlayer, we can change the temperature of our device by direct current (DC) ohmic heating. This mechanism provides an opportunity to return the string

to a clean state by desorbing attached molecules from it. Moreover an alternating current (AC), passing through our string, can actuate it efficiently which obviates the need for an external actuator.

I also noticed that the resonant frequencies of the nanostring shift with temperature. To do this end, we need to observe temperature dependent frequency sweeps. Therefore, we use a cryogenic vacuum chamber as shown in Fig. 9.2. This chamber has an integrated heater inside the chamber that is capable to generate heat in a controlled fashion. In particular, the frequency shift is observed in two different cases. For the first case, the sample stage is in thermal equilibrium at a uniform temperature $T = T_{\text{room}} + \Delta T$, and the frequencies can be expressed as

$$f_n = \frac{\omega_n}{2\pi} = \frac{n}{2L} \sqrt{\frac{A_1 \sigma - \sum_{k=1}^3 A_k E_k \alpha_{k,0} \Delta T}{\sum_{k=1}^3 A_k \rho_k}}, \quad (9.2)$$

where σ is the internal stress and $\alpha_{k,0} = \alpha_k - \alpha_0$ are the relative thermal expansion coefficients. The parameters E_k , A_k , α_k are Young's moduli, cross-sectional areas, thermal expansion coefficients of the materials [41]. These material parameters are defined for each layer with the indices $k = 0$ (silicon), $k = 1$ (silicon nitride), $k = 2$ (chromium), and $k = 3$ (gold).

The relative frequency shift for a small temperature change has the form of

$$\frac{f_n(\Delta T) - f_n(0)}{f_n(0)} = - \left[\frac{1}{2\sigma A_1} \sum_{k=1}^3 A_k E_k \alpha_{k,0} \right] \Delta T. \quad (9.3)$$

Equation 9.3 shows that the prefactor to ΔT is either positive or negative depending on the value of α_0 . For our string, the thermal expansion coefficient of the substrate, $\alpha_0 = 2.6 \times 10^{-6} \text{ K}^{-1}$, is larger than an effective alpha of the string that depends on the expansion coefficients of the constituent materials, $(\sum_{k=1}^3 E_k A_k \alpha_k) / (\sum_{k=1}^3 E_k A_k) = 1.89 \times 10^{-6} \text{ K}^{-1}$. Hence, the string is stretched tighter and the frequency of the string shifts upwards with heating of the device. The slope in Fig. 9.5 is $1.10 \times 10^{-4} \text{ K}^{-1}$, is consistent with our predicted value of $1.30 \times 10^{-4} \text{ K}^{-1}$, which is calculated by putting reasonable estimates of the material parameters [70].

For the second case, current is passed through the string such that the resistance of the metallic layer produces local heating. In this case, the supports and substrate can be considered as a heat bath at T_{room} . The resistance of the metallic layer

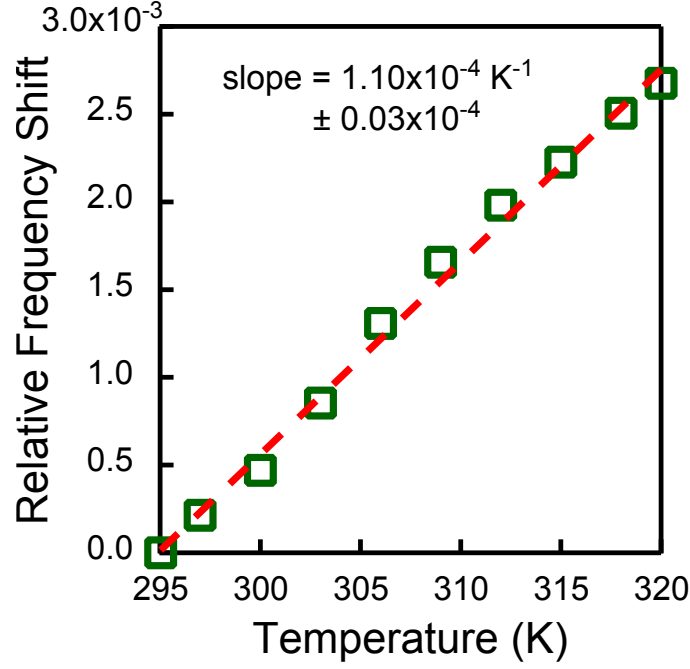


Figure 9.5: Relative frequency shift of the fundamental out-of-plane mode in vacuum (actuated with external piezoelectric) versus temperature as the entire sample stage is heated.

produces a local heating. The frequency shift has a similar form to Eq. (9.3), except that each $\alpha_{k,0}$ is replaced by its bare value α_k because the substrate remains in thermal equilibrium. In a model of resistive heating, the total excess heat energy comes into equilibrium when $\dot{U} = P - U/\tau_{\text{th}} = 0$, where P is the constant power of the current passing through the string and τ_{th} is the half-life for thermal energy to leak out of the string. The energy outflow can be estimated as a sum of thermal currents (of the form $j = -\kappa\nabla T$) driven by a gradient $\nabla T \approx \Delta T/(L/2)$. We can approximate

$$\tau_{\text{th}} = \frac{L^2 \sum_{k=1}^3 A_k \rho_k c_k}{2 \sum_{k'=1}^3 A_{k'} \kappa_{k'}} \approx 750 \mu\text{s} \quad (9.4)$$

using the overall heat capacity $C = L \sum_{k=1}^3 A_k \rho_k c_k \approx 3.69 \times 10^{-10}$ J/K of the string.

The analysis we have outlined is primarily limited by the fact that we have supposed the temperature profile $\Delta T(x, t) = \Delta T(t)$ to have no meaningful variation along

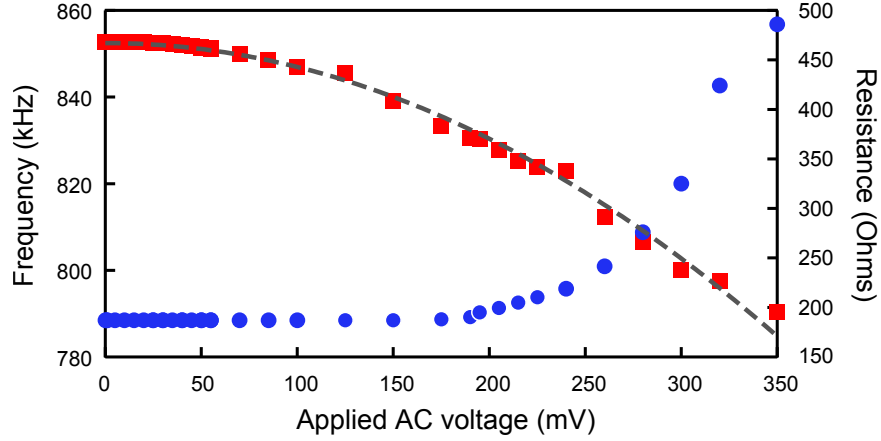


Figure 9.6: Absolute frequency shift of the fundamental mode in vacuum versus applied voltage using AC ohmic actuation (red squares) and corresponding device resistance (blue circles). Fit (dashed grey curve) is to Eq. 9.5.

the length of the string. Still, it reliably captures the fact that the thermal time scale is on the order of microseconds (rather than nanoseconds, as for the device described in Ref. [110]), orders of magnitude faster than the time for the mechanical energy to be transferred to the environment, as dictated by the high Q of the string: $Q/f_1 \approx 200$ ms.

For the case of AC local heating, the power passing through the string can be expressed as $P = V^2/R$, where R is the string's electrical resistance and $V(t) = V_0 \cos \omega t$ is the alternating voltage applied across the string. The resistance of the string can be estimated from the geometry of the string using reasonable values r_2 , and r_3 for the resistivity of Cr and Au ($R_1 \approx \infty$ for silicon nitride): $R = (\sum_{k=1}^3 1/R_k)^{-1} \approx L(A_2/r_2 + A_3/r_3)^{-1} = 52 \Omega$. It is also possible to measure the resistance of the string experimentally which is 176Ω . This measurement is performed by a simple two probe technique. The experimental value is higher because it includes the resistance of the metallic supports as shown in Fig. 9.2(b).

Since an AC voltage is applied, the analogue of Eq. (9.2) is

$$\begin{aligned} \frac{f_n(\Delta T) - f_n(0)}{f_n(0)} &= -\frac{V_0^2 \tau_{\text{th}}}{4\sigma A_1 C R} \sum_{k=1}^3 A_k E_k \alpha_k \\ &= -\frac{L}{8\sigma A_1 R} \left(\frac{\sum_{k=1}^3 A_k E_k \alpha_k}{\sum_{k'=1}^3 A_{k'} \kappa_{k'}} \right) V_0^2. \end{aligned} \quad (9.5)$$

The relative frequency shift is quadratic in V_0 and always negative which is consistent with the observed data in Fig. 9.6. In contrast to the relative frequency shift described by Eq. (9.3), which is insensitive to the device length, the effect described in Eq. (9.5) is predicted to scale as $\tau_{\text{th}}/C \sim L$ (and thus can be made arbitrarily large by choosing a long enough string). The estimated coefficient, 0.04133 V^{-2} , is about 15 times smaller than the value $0.648(9) \text{ V}^{-2}$ obtained by fitting Eq. 9.5 to the data in Fig. 9.6. We can rectify this inconsistency by taking the thermal time constant to be $\tau_{\text{th}} = 72 \mu\text{s}$. This inconsistency is likely because of the over-simplified, uniform temperature profile along the string.

9.4 Integrated actuation of bi-layer nanostrings

It is observed that a very small amount of AC current along the string can actuate our string efficiently. Specifically, this local heating can be used to actuate the bilayer nanostring by passing an AC current along the length of the device. Note that this is subtly different from the bimaterial effect in cantilevers and non-uniformly coated beams, where the gold exerts a force on the cantilever that pushes it towards the substrate [110, 111, 112]. In such a scenario, the force is directional, and hence the AC drive voltage must be applied at frequency $f/2$ in order to produce heating and bending at f . In contrast, in our system there is no preference towards or away from the substrate as the gold expands, since it forms a continuous layer over the string. Heating and bending occur twice per string oscillation, and therefore the applied drive voltage and resulting motion have the same frequency. It is also possible to actuate our device at $f/2$. In Fig. 9.7, PSD amplitudes of the same string are shown but actuated at different frequencies. It is actuated at f in Fig. 9.7(a) and at $f/2$ in Fig. 9.7(b). The drive voltage is 10 mV in both scenarios. Therefore, it reveals that the actuation at $f/2$ is ≈ 1000 times less efficient for the string—consistent with the

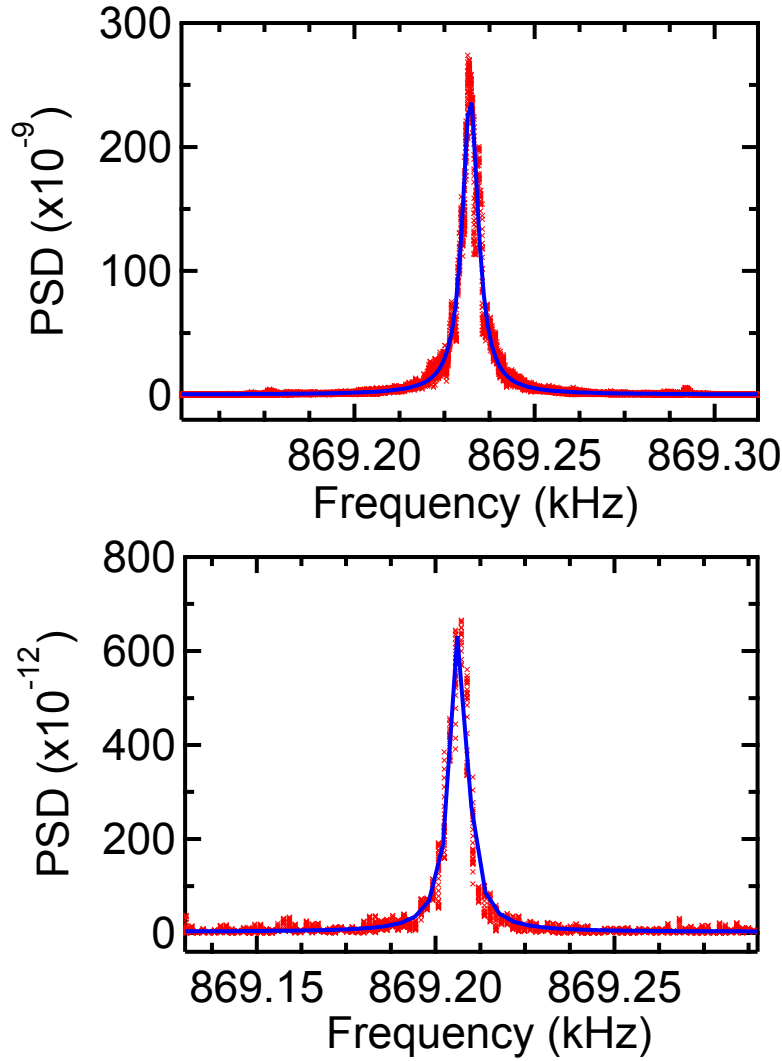


Figure 9.7: Fundamental out-of-plane mode of a 210 μm long string, actuated at (a) f , and (b) $f/2$ by the AC ohmic thermal effect. The corresponding line widths are 5.28 and 5.62 Hz for figure (a) and (b) respectively.

above explanation. It is also notified to us that the actuation of our bi-layer string at f and $f/2$ could be well explained in terms of opto-mechanical interactions [113].

Fig. 9.8 shows the frequency sweeps of the string actuated by AC local heating at different drive voltages using the reference output of the Zurich lock-in amplifier. This integrated electronic actuation scheme is simple, compact, and robust. With

root-mean-square AC voltages as small as $100 \mu\text{V}$ we can clearly detect resonant motion, while the maximum signal-to-noise is achieved with approximately 15 to 20 mV. At higher drives the nanostring becomes nonlinear. Yet even at quite high drives, in vacuum, there is no significant change in the resistance (Fig. 9.6) of the bilayer nanostring up to 180 mV which is approximately 10 times higher than the voltage for optimal signal-to-noise ratio. Hence the local heating of the bilayer nanostring is nondestructive to the gold layer in the linear actuation regime and beyond. In addition, we note that the resonance frequency is entirely non-hysteretic at these actuation voltages—further evidence that the AC ohmic actuation scheme is robust. The optimum signal-to-noise is achieved with ~ 15 to 20 mV. Only at voltages > 180 mV, the resistance starts to increase with increasing applied voltage and diverges at 350 mV, where it becomes an open circuit. Using the extracted value $\tau_{\text{th}} = 72 \mu\text{s}$, we can estimate that the upturn in resistance, appearing at $V_0 \approx 180$ mV in Fig. 3(c), begins when the device has been heated an additional $\Delta T \approx 56$ K and that burn out occurs when $V_0 \approx 450$ mV and $\Delta T \approx 350$ K. An

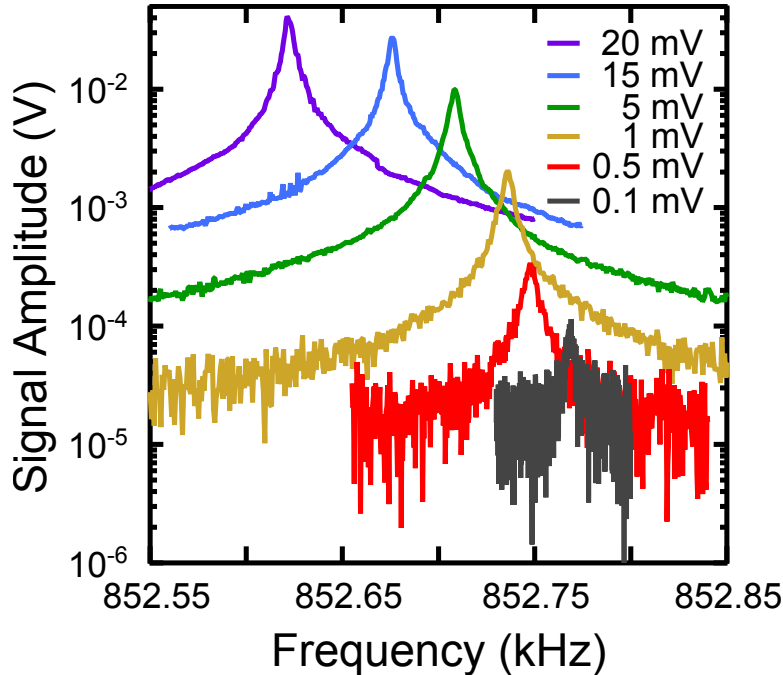


Figure 9.8: Fundamental out-of-plane mode actuated by the AC ohmic thermal effect.

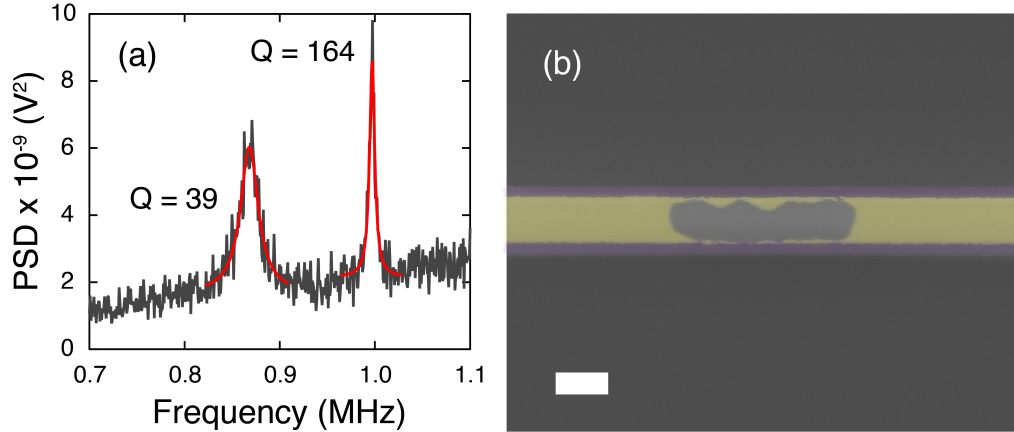


Figure 9.9: (a) Frequency response of the first out-of-plane (lower frequency) and in-plane (higher frequency) modes in air using AC thermoelastic actuation (400 mV drive) with corresponding PSD fits (red) to extract the Q . (b) SEM of the gold bilayer nanostring after current induced failure after ≈ 450 mV AC drive. Gold has come off the device enough to break the current path, resulting in insulating behavior. Scale bar is $2\mu\text{m}$.

SEM of our damaged string is shown in Fig. 9.9(b).

It is worth noting that the AC thermoelastic heating works for both higher-order harmonics in vacuum as well as for the fundamental modes in air. The Q s of the fundamental out-of-plane and in-plane modes are 40 and 160 in air respectively as shown in Fig. 9.9(a) orders of magnitude smaller than the Q s in vacuum. This is due to the fact that the nanostring experience strong viscous damping and squeeze film forces at ambient pressure, especially when the motion is perpendicular to the string's width. This is because there is a greater cross-section for molecular collisions, and thus energy loss, in the out-of-plane direction. Furthermore, the voltages required to actuate the nanostring in air (≈ 400 mV) result in resistance changes and eventual failure. Improving the Q in viscous environments [71, 115] would decrease the required actuation voltages and prevent such failure.

In this Chapter, we have shown that a metallic layer gold can be added on top of our silicon nitride nanostrings without adversely destroying the Q of our devices. This layer provides a scheme for local heating to study thermal response of molecules or desorb unwanted molecules, and provide simple and integrated actuation. Moreover this will provide us the opportunity to functionalize our nanostrings and capture

particular molecules as described in next Chapter.

CHAPTER 10

Metabolite Acetone Detection

Here we show the potential to detect the metabolite acetone in human breath. In the human body, there are numerous metabolites generated by various processes. When diseased, these metabolites can change concentrations or result in new metabolites [116, 117]. For example, a diabetic patient produces an excess of acetone which can be present in the breath [116, 118]. To detect diseases in their early stages, it could be a useful to make a breath analyzer that can detect even tiny changes in metabolites, such as acetone in the breath.

Here we are proposing a way to use our nanostring sensor as a one prototype to serve this purpose. As seen throughout this thesis, our nanostrings are patterned from high stress silicon nitride and hence provide very high mechanical quality factor resulting in great sensitivity. These devices are excellent candidates for mass sensing as shown in Chapter 6. However, they alone are not good enough to detect a particular molecule adsorbed on their surfaces. As shown in Chapter 7, we have to add a second technique in our system to probe the attached molecule RDX by our nanostrings. Building on the gold layer of Chapter 9, here we propose a way to functionalize that gold surfaces with particular thiol molecules to capture a molecule of choice.

10.1 Functionalization of a gold surface to form self assembled monolayers (SAMs)

10.1.1 Functionalization with 3-amino-1-propanethiol hydrochloride

We collaborate with Prof Juli Gibbs-Davis from the Department of Chemistry at University of Alberta to build a protocol on functionalization of a gold surface. There are three components in self assembled monolayers (SAMs), such as a head group which binds to the substrate, a carbon chain, and a tail group which is the functional portion. Functionalization of a gold surface by thiol species is one of the convenient ways to form SAMs because gold has a great affinity to sulphur. The dissociation energies for gold-sulphur and gold-gold bonds are 418 kJ/mol and 226 kJ/mol respectively [28]. Thiols (R-SH) are organic compounds which are sulfur analog to alcohol (R-OH). These are named by adding suffix -thiol to the parent hydrocarbon name.

In this thesis, we prefer to functionalize our gold surfaces with particular thiols in solution phase [119]. As a preliminary test, 3-amino-1-propanethiol hydrochloride is chosen to functionalize gold surface of our devices. The chemical formula of

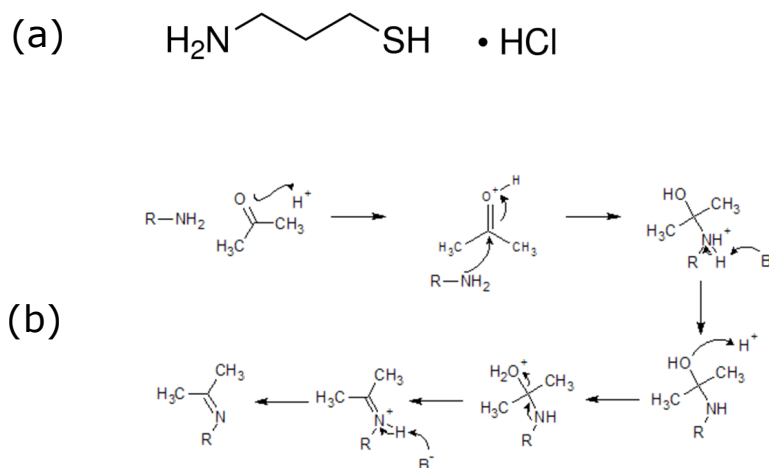


Figure 10.1: (a) Structure of 3-amino-1-propanethiol hydrochloride, and (b) mechanism of imine formation.

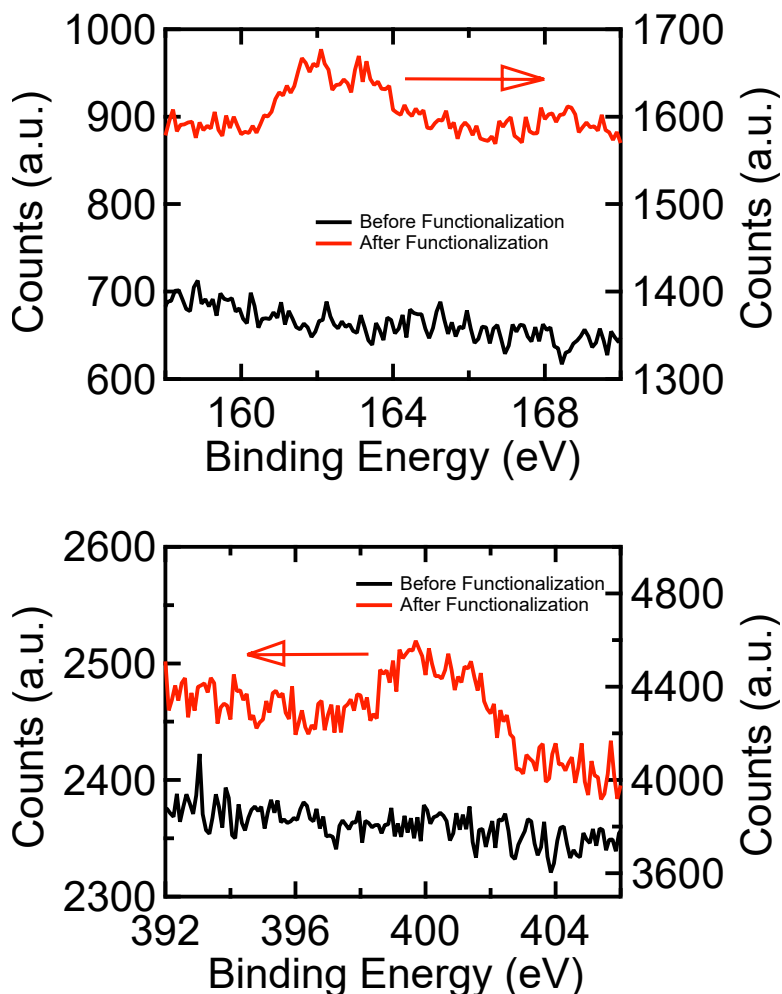


Figure 10.2: XPS data shows comparison for two gold chips with same dimensions and same gold thickness. One gold chip is functionalized with 3-amino-1-propanethiol and another without functionalization. The peaks due to the existence of (a) sulfur and (b) nitrogen from the functionalized device. However no peaks are visible from the gold chip without functionalization.

this compound is $C_3H_9NS \cdot HCl$ and the structure of this compound are shown in Fig. 10.1(a). This compound is chosen to capture acetone by chemisorption, through an imine formation, as seen in Fig. 10.1(b).

To prepare the amine solution, glasswares are cleaned with acetone, isopropyl alcohol (IPA), and ethanol, respectively. It is important and crucial to ensure no

acetone remained in any glassware to avoid reaction with 3-amino-1-propanethiol hydrochloride. A balance was used to weigh 0.0185 g of 3-amino-1-propanethiol and then added to 20 mL of 100% ethanol (in a glass beaker) to yield a 7.2 mM solution. It is observed that the thiol molecules absorb moisture from the atmosphere and hence it is recommended to weigh the molecules in as short as possible time. The glass beaker is then sonicated for a couple of minutes to mix the thiol molecules in ethanol properly. No precipitate is observed at the bottom of the beaker. Then triethylamine is added to the solution until it obtained a pH of 11–12. The solution is then divided into two equal portions and poured into two vials. A gold chip (without pattern) is dipped into one vial and a chip, containing gold and silicon bi-layer strings (as shown in Chapter 9), is dipped into another vial. The gold thickness (43 nm) is same for both chips. Open space of the vials are backfilled with inert helium gas and then sealed with parafilm. The vials are wrapped with aluminium foil to avoid light exposure. The chips were left in solution for 72 hours at room temperature. After removal, the chips were gently rinsed in 100% ethanol to remove any extra 3-amino-1-propanethiol hydrochloride. Both chips were dried by gently flow with nitrogen. The chip containing bi-layer strings was mounted immediately into the vacuum chamber to characterize. The gold chip was submitted for X-ray photoelectron spectroscopy (XPS) data. In addition, another gold chip (without functionalization) is submitted for XPS for comparison.

10.1.2 Confirmation of SAMs formation on gold surface

After getting back the XPS data, analysis was performed. Fig. 10.2 shows the data from both the functionalized gold chip and bare gold chip. Two separate graphs are generated to show peaks of sulfur and nitrogen clearly. It is noticed that the existence of sulfur is confirmed from the functionalized gold chip as shown in Fig. 10.2(a). However no sulfur peak is visible from the bare gold chip XPS data. Similarly, a nitrogen peak is visible in Fig. 10.2(b) which comes from the functionalized gold chip. These peaks clearly indicates the formation of SAMs by 3-amino-1-propanethiol hydrochloride on our gold surface. In addition, water contact angle measurement was performed. It was observed that average value of contact angle was shifted from 66.3 degree to 77.2 degree. This could be due to the hydrophobicity of the carbon chain competing with the hydrophilicity of the amine group.

10.1.3 Data from a functionalized gold and silicon nitride bi-layer string

Fig. 10.3(a) shows the resonance frequency of a 174 μm long gold and silicon nitride bi-layer string (as described in Chapter 10) before functionalization. The resonance frequency and the Q of the device are 1.2818 MHz and 8×10^4 respectively. The chip containing this device is then dipped into 3-amino-1-propanethiol hydrochloride solution to form SAMs on top of gold surface. From the result of the previous section, now we have confidence that the SAMs are formed on top of our gold surface. After maintaining similar procedure as discussed in the previous section, the chip is cleaned and mounted back into the vacuum chamber immediately. The frequency sweep is taken from the same device after functionalization as shown in Fig. 10.3(b). It is expected to decrease the resonance frequency due to the addition of new molecules to the string's surface. However, it is observed that the resonance frequency (1.8261 MHz) is increased by 5 kHz compared to the frequency of the device before functionalization. The tension of the surface layer could be increased due to the formation of the SAMs on top of gold surface. This is also reflected in the Q of the device after functionalization which is 10×10^4 . This Q value is slightly higher than the Q value of the device before functionalization.

The next step is to capture acetone by this functionalized string. Therefore, saturated acetone vapour is flowed through the chamber and then resonance frequency is measured. If acetone molecules are captured by the functionalized string then the mass of the string will be increased. Then it is expected that the resonance frequency of the device will go down due to the increase of the mass. However, we could not find any significant frequency shift of the device. That leads us to make the conclusion about two possibilities. The acetone might not be captured with this chosen thiol molecules or the mass addition due to acetone capture is too small to our device to notify.

10.2 Acetone detection by a functionalized nanostring

The result of the previous section gives us confidence that the gold surface of our device could be functionalized with particular thiol molecules 3-amino-1-propanethiol hydrochloride. Unfortunately, acetone could not be detected with this thiol molecule.

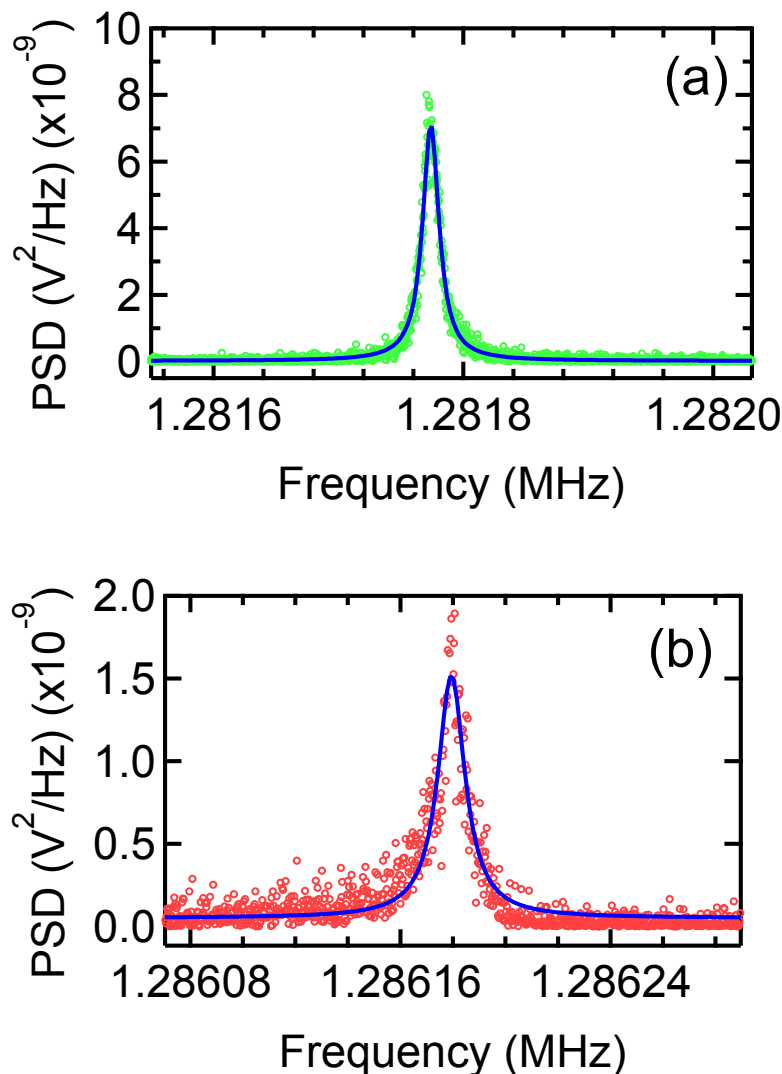


Figure 10.3: The frequency sweep is taken from a 174 μm long string (a) before, and (b) after functionalization with 3-amino-1-propanethiol hydrochloride. 14.42 Hz and 12.55 Hz are corresponding line widths of the string before and after functionalization.

Therefore, it is decided to explore new thiol molecules to capture acetone. The new thiol molecule 11-(aminooxy)undecane-1-thiol is synthesized in Gibbs-Davis lab of the Department of Chemistry at University of Alberta. The chemical formula of this structure is $\text{C}_{11}\text{H}_{25}\text{NOS}$. In addition, there is another possibility that the captured acetone mass is too small to make any significant shift in resonance frequency of

the device. Therefore, a second detection technique photothermal spectroscopy is incorporated into our system as discussed in detail in Chapter 7. The principle of this technique is that the molecules absorb IR wavelength at one of their vibrational frequency then produce heat which is transferred to the device and results in a shift of the resonance frequency to a new value.

As discussed in Chapter 7, it is essential to take a frequency sweep of a device using QCL before capture of any molecules. This frequency sweep is considered as a baseline for the device. This baseline gives us opportunity to compare the frequency response of the device after functionalization and acetone capture. Therefore, attempt is made to take baseline from a gold and silicon nitride bi-layer strings. But no significant change in frequency shift is observed due to the IR incident on the gold surface of the string. This is because gold is a metal and it has a good thermal conductivity. When IR laser is shined to the gold surface, the produced heat is immediately transferred to two giant end gold posts and no significant change in frequency shift is observed. Therefore, it is essential to re-design our device before further proceeding.

10.2.1 Fabrication of nanostring with two gold pads

As discussed, to avoid the immediate heat transfer, the nanostrings are re-designed and fabricated by electron beam lithography (EBL) process as shown in Fig. 10.4(a). The silicon nitride is patterned on a positive EBL resist (ZEP 520A) and then translated to silicon nitride by RIE. Then ZEP is removed by UV exposure followed by acetone and IPA rinse. To pattern the gold pads on selective portions of the string, a bi-layer PMMA is spun on the chip. EBL alignment is performed to open small windows in PMMA to open desire portions of the string. 5–7 nm of chromium is deposited followed by 35 nm of gold where chromium serves as an adhesion layer. Then lift off is performed to remove PMMA and unwanted gold and chromium from the chip. Finally the device is released by wet etch in BOE solution. One of the released devices fabricated by this method is shown in Fig. 10.4 (a). In our current device, we only have gold surfaces on two specific regions of our devices.

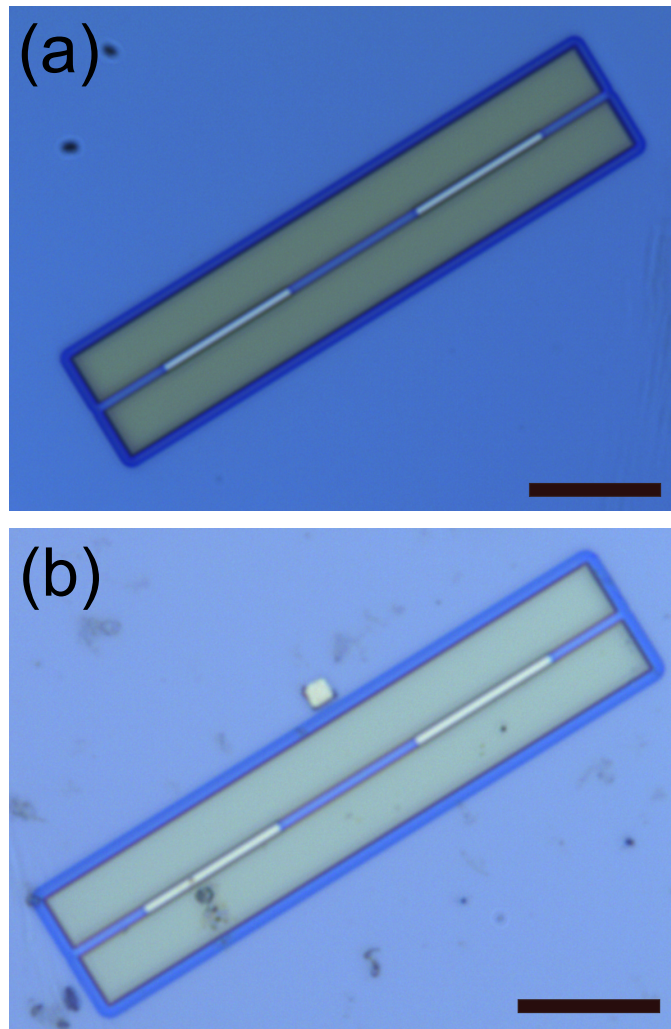


Figure 10.4: Optical microscope image showing a $90\ \mu\text{m}$ and $1\ \mu\text{m}$ wide nanostring. The optical image is taken (a) before and (b) after functionalization.

10.2.2 Baseline of a silicon nitride nanostring with two gold pads

It is expected that the detection laser (red) will not produce any heating effect because it will be parked at the middle of the string where no metal exists as shown in Fig. 10.4(a). The length of each gold pad is $22.5\ \mu\text{m}$ and the distance between two pads is also $22.5\ \mu\text{m}$. Interestingly, we still get a small heating effect

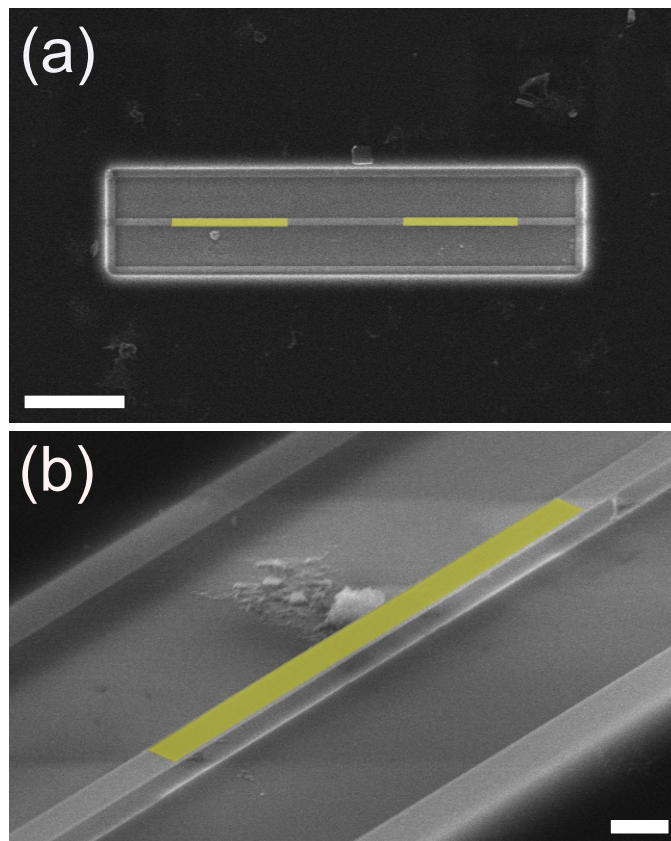


Figure 10.5: SEM image are taken from a 90 μm and 1 μm wide nanostring after functionalization. (a) Full image of the device, and (b) zoomed in image of a single gold pad on the string. The scale bars are of 20 μm and 2 μm long respectively.

from the red laser though the diameter of the laser spot is $\approx 1 \mu\text{m}$. The origin of this heating effect is believed due to scattering of light. We note that this heating effect gets smaller for larger gaps between two gold pads. To detect the existence of the acetone capture by these nanostrings a second technique is incorporated to our system as described in Chapter 7. We use a QCL laser head with range of $1565\text{--}1759 \text{ cm}^{-1}$ because strong absorption peak is observed in this range for a gaseous acetone. Immediately after the fabrication of a string, a baseline is taken using the QCL sweeps in 1 cm^{-1} interval as shown in Fig. 10.7(a). The detail data acquisition procedure is described in Chapter 7. However, it is observed that the signal is noisy because there are a lot of water absorption peaks in this wavelength

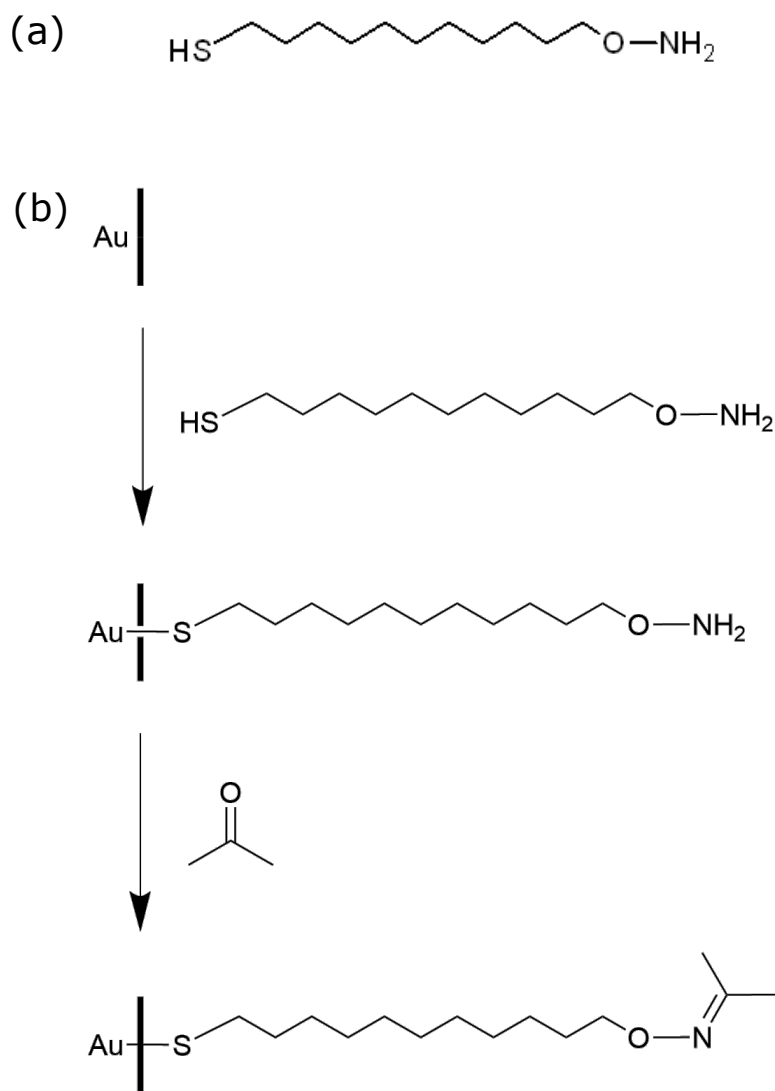


Figure 10.6: (a) Chemical structure of 11-(aminoxy)undecane-1-thiol, and (b) acetone capture scheme with a functionalized Au surface with this thiol molecule.

range.

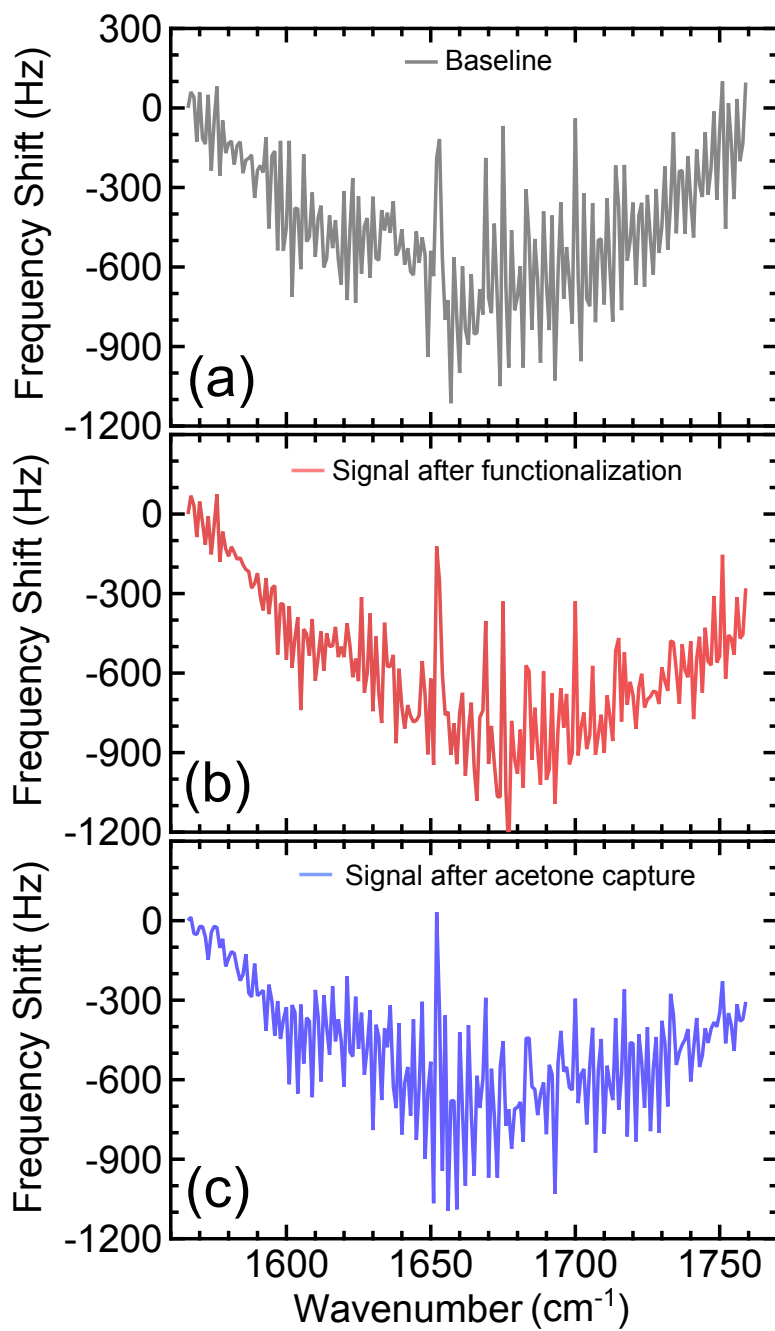


Figure 10.7: IR frequency sweep of (a) bare string, (b) after functionalization, and (c) after acetone capture.

10.2.3 Functionalization of new nanostrings

A new thiol molecule (11-(aminooxy)undecane-1-thiol) was synthesized in the Gibbs-Davis lab to form SAM on these devices. The structure of this molecule is shown in Fig. 10.6(a). A 5 mM solution of this molecule was prepared in a beaker with 20 mL of ethanol. The solution was poured in a wide neck vial. The chip was then dipped into the solution and sealed with para-film prior to fill the free space with nitrogen. The vial was wrapped with aluminium foil to avoid light exposure and left for at least 24 hours. It was expecting to have a uniform SAM after this time period. The chip was taken out of the vial and rinsed in ethanol for couple times then rinsed in isopropyl alcohol for three times to remove any loosely bound thiol molecules. It is also necessary to avoid long time exposure in air because that could lead the string to stick with the substrate. An optical image is taken immediately after this functionalization process as shown in Fig. 10.4(b). Scattered residues are observed all over the chip after this functionalization process. The SEM images of that device were also taken to inspect thoroughly. Fig. 10.5 shows no significant residues present on the device although a lot of scattered residues are observed all over the place. However, the solution could be filtered to avoid this problem. Then the chip was mounted into the vacuum chamber to take the IR frequency sweep of the same device as shown in Fig. 10.7(b).

10.2.4 Acetone detection

The proposed scheme of acetone capture by a functionalized Au surface (with 11-(aminooxy)undecane-1-thiol) is shown in Fig. 10.6(b). This scheme shows after the functionalization process, the Au surface should have a long carbon chain with NOH_2 at the end. At the final step (Fig. 10.6(b)), after acetone capture, the NH_2 will be replaced by $\text{N}=\text{C}$ bond. Since we are taking IR frequency sweep therefore a strong IR absorption peak is expected due to the $\text{C}=\text{N}$ stretching in between $1640\text{--}1660\text{ cm}^{-1}$ [120, 121].

After taking the IR frequency sweep of that device after functionalization, it was dipped into 20 mL of acetone in a beaker. The beaker was sealed and left for at least 24 hours to make stable reaction between acetone and thiol molecules. After 24 hours, the chip was rinsed in acetone, ethanol and isopropyl alcohol to wash off any extra solvent. The sample was mounted back into the vacuum chamber to

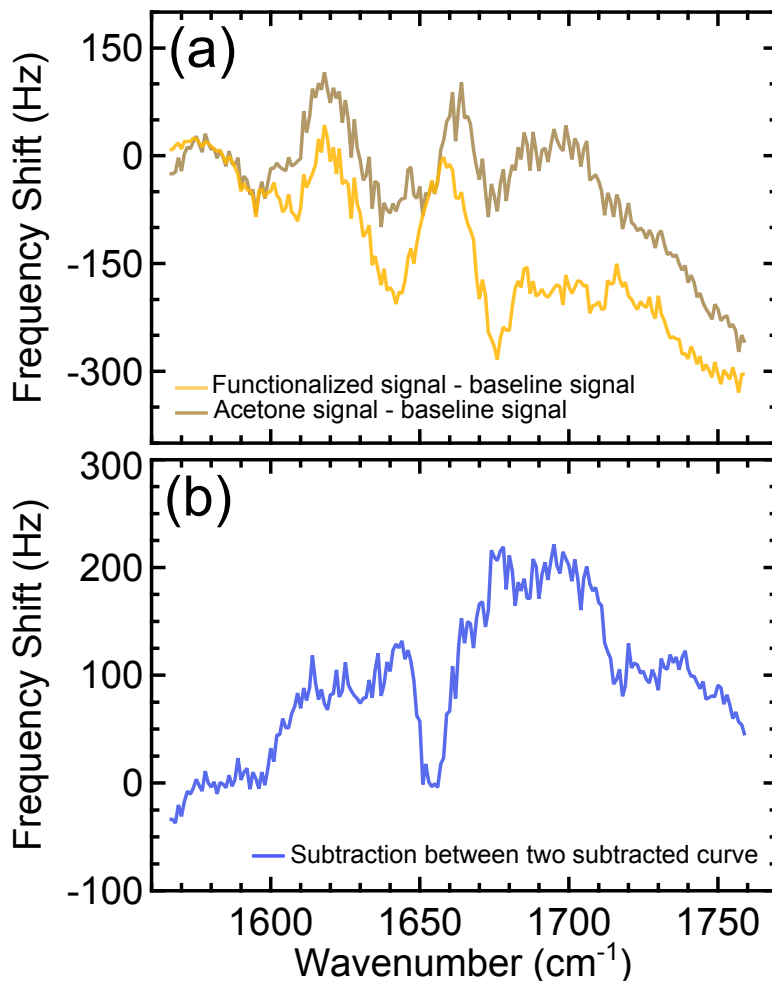


Figure 10.8: (a) Baseline is subtracted from the frequency sweeps after functionalization and after acetone capture. (b) Baseline subtracted functionalized sweep is subtracted from the baseline subtracted acetone sweep.

take the IR frequency sweep of the device after the acetone capture as shown in Fig. 10.7(c). The signals are noisy, so no significant difference is visible immediately between the signal from bare nanostring, functionalized nanostring and acetone captured nanostring. However, after careful inspection we found a significant change in signal around 1650 cm^{-1} . Therefore, for a better presentation, the baseline signal is subtracted from the functionalized signal and acetone captured signal as shown in Fig. 10.8(a).

It is now obvious that there is a change between these two subtracted lines around 1650 cm^{-1} with different background slopes. This is because of the frequency instability due to heating effect produced from the scattering of the red laser. However, Fig. 10.8(b) shows the subtraction of those two subtracted signals and an IR absorption peak is visible at 1655 cm^{-1} which is consistent with other reported IR absorption peak [121]. This clearly indicates the existence of C=N double bond onto our functionalized string which confirms the acetone capture by our string. However, we could not estimate the captured acetone amount or sensitivity from this experiment. It might need further detail study to conclude the sensitivity of our device for sensing acetone as metabolites.

In this Chapter, silicon nitride nanostring is fabricated with two selective gold pads onto the string in such a way that the middle of the string is not metallized. This provides us the opportunity to shine the red laser at the middle of the string without major heating of the gold pads. The string is then functionalized with specific thiol molecules. The IR frequency sweep confirms the acetone capture by this functionalized string.

CHAPTER 11

Metabolites sensing by hybridized arrays

In this chapter, I propose how to make gold coated two-string and three-string array so that these arrays could be functionalized to capture metabolites molecules. The sensing applications of these hybridized nanostrings are potential future work of this thesis.

11.1 Better frequency stability avoiding laser heating effect

The frequency instability due to laser heating effect was one of the major impediment for the method described in Chapter 10. The device proposed for two-string array is shown in Fig. 11.1. A bare silicon nitride string is connected to another silicon nitride string coated with gold strip by a small connecting post. If the frequencies of these two devices are close to each other then they will demonstrate hybridization. Then the bare string will act as a detection string where red laser will be focused at the middle of the string. Since the gold strip is far away from the silicon nitride string so it is expected to have negligible or no laser heating effect.

Now we know that hybridization occurs only if the frequencies of each device are identical to each other or integer multiple of each other. According to our proposed design of the hybridized array, one string is made of silicon nitride and another one is coated with gold. Gold is heavier than silicon nitride. Therefore, the frequency of a gold coated string will be shifted to a lower value. In that case, there is a

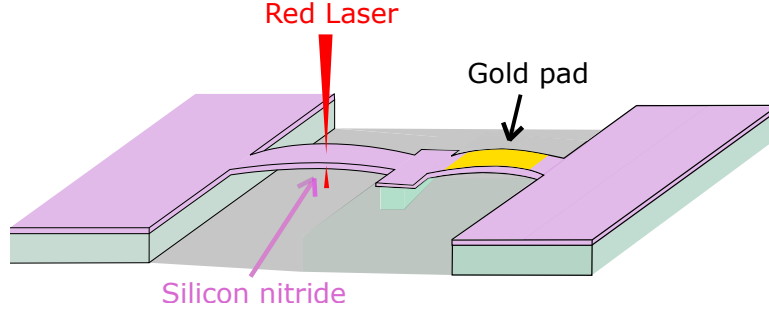


Figure 11.1: Schematic shows hybridized array of a silicon nitride string and gold coated silicon nitride string.

less possibility to observe hybridization between them. In that case, one must first perform modelling to optimize the dimensions of gold pad and the silicon nitride string.

11.2 Theoretical model to enable hybridization between a silicon nitride and gold coated silicon nitride string

As I pointed out in last section, it is important to make a proper choice of the strings lengths to form hybridization between them. Since one string will be gold coated therefore their lengths should be different from each other. Let us consider a string of length L as shown in Fig. 11.2. The gold pad is chosen at the middle of the string and length, width and thickness of the gold pad are $2d$, w and t respectively. Then the effective mass of this gold pad can be written as,

$$dm_{eff} = \int \rho Y_n^2(x) dV = \int_0^t \int_0^w \int_0^L \rho(x) \sin^2(n\pi x/L) dx dy dz. \quad (11.1)$$

This can re-write as,

$$dm_{eff} = tw\rho \int_{\frac{L}{2}-d}^{\frac{L}{2}+d} \sin^2(n\pi x/L) dx. \quad (11.2)$$

After solving this equation, we have

$$dm_{eff} = t w \rho \left[d - \frac{L \cos\left(\frac{n\pi}{2}\right) \sin\left(\frac{2n\pi d}{L}\right)}{2\pi n} \right]. \quad (11.3)$$

Using Eq. 11.3, it could be possible to find the effective mass of the gold pad of the string. Since we know the relation between the effective mass and the frequency shift of a string, then it could be possible to calculate new frequency of the gold coated string. Finding the new frequency of the gold coated string, one could easily decide on the dimension of the bare silicon nitride string.

11.3 Functionalization of two-string array

Functionalization will be performed on the gold coated string using specific thiol molecules. For example, same thiol species can be used as described in Chapter 10. We are expecting to have no heating effect for this device. The frequency stability of this device will be tested by performing Allan deviation measurement. After testing the frequency stability, the device will be functionalized with a specific thiol molecule. For confirmation, photothermal spectroscopy can be performed to make sure the existence of the self assembled monolayer of the thiol species.

After preliminary test of this device, the acetone will be flowed in the chamber to get capture by functionalized device. Hopefully, the photothermal spectroscopy will be able to resolve the affixed molecules and the amount can be determined by the technique described in Chapter 6.

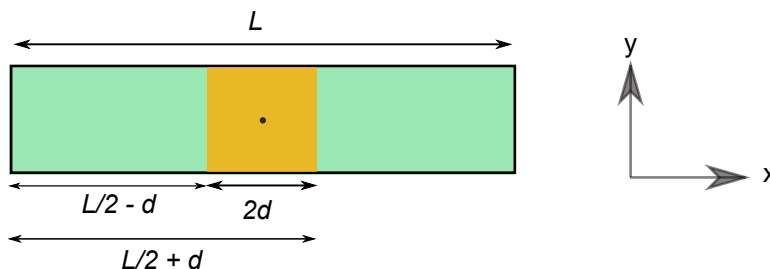


Figure 11.2: Diagram of a gold pad on a bare silicon nitride string.

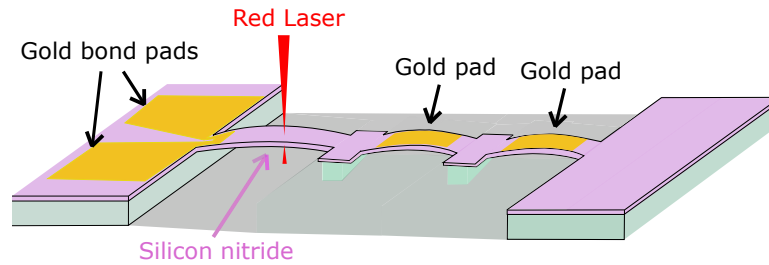


Figure 11.3: Schematic shows parallel sensing by a three-string array.

11.4 Parallel sensing by three-string array

Similarly, it could be possible to make a three-array with gold pads on them as shown in Fig. 11.3. The middle and right end strings have gold pads at the middle of the string. The gold surface of these strings can be functionalized with two different thiol molecules to capture two different metabolites (or other molecules). This application will be a better application of our hybridized string for parallel sensing application. In addition, a small gold loop is added to the left end string so that the array can be actuated externally.

In this Chapter, I have briefly enlisted few ideas which can be potential applications of our hybridized nanostrings. One can extend these ideas and could apply in various systems of sensing applications.

CHAPTER 12

Summary

Fantastic progress has been made on sensing applications using nanomechanical resonators for the last decade. The resonators are mostly used in sensing applications using the resonance frequency of as the sensing parameter. Therefore, on going interest was to investigate how to increase the quality factor of a mechanical device. The high quality factor device provides better resolution in sensing application specially for mass sensing.

In this thesis, our target was to fabricate new types of mechanical resonators which can be used in sensing applications. Varieties of experimental works performed to accomplish this goal. A number of procedures were developed to fabricate various nanomechanical nanostrings such as bare silicon nitride nanostring, one dimensional arrays of silicon nitride strings, gold coated silicon nitride strings and silicon nitride strings with a selected gold portion on it. After successful fabrication of nanostrings from high stress silicon nitride, devices were found to show high Q as expected. Then successful study was performed to investigate the loss channels of this nanostrings which inspired us to design one dimensional arrays of high Q nanostrings. After conceiving nanostring arrays, it is revealed that the Q increment was not that promising but strong coupling shows mode hybridization between the connecting strings. The mode hybridization is obtained through a small connecting post in between two adjacent nanostrings. Depending on the strong coupling the system shows strong mode hybridization which provides the opportunity of remote mass sensing applications. This mode hybridization could also provide the parallel sensing applications. Moreover, bare silicon nitride nanostrings demonstrated explosive molecule

detection with help of second detection technique, photothermal spectroscopy in our case. However, it was found that the bare silicon nitride itself is not good candidate in varieties of molecular sensing applications. Therefore, metallization of our nanostring was demonstrated by depositing Au and Cr on top of silicon nitride such that they can be functionalized by thiol species to capture a molecule of choice. The integrated actuation is demonstrated for this bi-layer nanostring without major reduction of the mechanical Q of the device. Then gold coated nanostring was functionalized with specific thiol molecules and it was demonstrated successfully to capture metabolite acetone. After this successful demonstration, we got the inspiration to functionalize hybridized arrays to capture specific metabolites remotely as discussed future extension of this thesis.

Bibliography

- [1] S. Schmid, S. Dohn and A. Boisen, *Sensors* **10**, 8092 (2010).
- [2] S.S. Verbridge, J.M. Parpia, R.B. Reichenbach, L.M. Bellan and H.G. Craighead, *J. Appl. Phys.* **99**, 124304 (2006).
- [3] S.S. Verbridge, H.G. Craighead and J.M. Parpia, *Appl. Phys. Lett.* **92**, 013112 (2008).
- [4] S. Schmid and C. Hierold, *J. Appl. Phys.* **104**, 093516 (2008).
- [5] J. Sulkko, M.A. Sillanpää, P. Hakkinen, L. Lechner, M. Helle, A. Fefferman, J.M. Parpia and P.J. Hakonen, *Nano Lett.* **10**, 4884 (2010).
- [6] X.M.H. Huang, M. Manolidis, S.C. Jun and J. Hone, *Appl. Phys. Lett* **86**, 143104 (2005).
- [7] M.L. Roukes, *arXiv:cond-mat/0008187v2*.
- [8] M.L. Roukes, *Physica B.* **1** 263-264 (1999).
- [9] S.S. Verbridge, R. Ilic H.G. Craighead and J.M. Parpia, *Appl. Phys. Lett* **93**, 013101 (2008).
- [10] A. Suhel, B.D. Hauer, T.S. Biswas, K.S.D. Beach and J.P. Davis, *Appl. Phys. Lett.* **100**, 173111 (2012).
- [11] S. Schmid, K.D. Jensen, K.H. Nielsen and A. Boisen, *Phys. Rev. B* **84**, 165307 (2011).
- [12] Q.P. Unterreithmeier, T. Faust and J.P. Kotthaus, *Phys. Rev. Lett.* **105**, 027205 (2010).

- [13] I. Wilson-Rae, *Phys. Rev. B* **77**, 245418 (2008).
- [14] I. Wilson-Rae, R.A. Barton, S.S. Verbridge, D.R. Southworth, B. Ilic, H.G. Craighead and J.M. Parpia, *Phys. Rev. Lett.* **106**, 047205 (2011).
- [15] Y.K. Yoo, M.-S. Chae, J.Y. Kang, T.S. Kim, K.S. Hwang and J.H. Lee, *Anal. Chem.* **84**, 8240 (2012).
- [16] M. Li, E.B. Myers, H.X. Tang, S.J. Aldridge, H.C. McCaig, J.J. Whiting, R.J. Simonson, N.S. Lewis and M.L. Routes, *Nano Lett.* **10**, 389 (2010).
- [17] A. Sampathkumar, K.L. Ekinci and T.W. Murrays, *Nano Lett.* **11**, 1014 (2011).
- [18] I. Bargatin, E.B. Myers, J.S. Aldridge, C. Marcoux, P. Brianceau, L. Durafourg, E. Colinet, S. Hentz, P. Andreucci and M.L. Roukes, *Nano Lett.* **12**, 1269 (2012).
- [19] E. Gil-Santos, D. Ramos, A. Jana, M. Calleja, A. Raman and J. Tamayo, *Nano Lett.* **9**, 4122 (2009).
- [20] E. Gil-Santos, D. Ramos, V. Pini, M. Calleja and J. Tamayo, *Appl. Phys. Lett.* **98**, 123108 (2011).
- [21] R. B. Karabalin, M. C. Cross, and M. L. Roukes, *Phys. Rev. B* **79**, 165309 (2009).
- [22] H. Okamoto, T. Kamada, K. Onomitsu, I. Mahboob and H. Yamaguchi, *Appl. Phys. Expr.* **2**, 062202 (2009).
- [23] L. A. Pinnaduwege, D. Yi, F. Tian, T. Thundat, and R. T. Lareau, *Langmuir* **20**, 2690 (2004).
- [24] R. Berger, E. Delamarche, H. Peter Lang, C. Gerber, J.K. Gimzewski, E.Meyer and H.-J. Güntherodt, *Science* **276** 2021 (1997).
- [25] J.L. Arlett, E.B. Myers and M.L. Roukes, *Nature Nano.* **6**, 203 (2011).
- [26] R. Marie, H. Jensenius, J. Thaysen, C.B. Christensen and A. Boisen, *Ultramicroscopy* **91**, 29 (2002).
- [27] M. Godin, P. J. Williams, V. Tabard-Cossa, O. Laroche, L.Y. Beaulieu, R.B. Lennox and P.H. Grütter, *Langmuir* **20**, 7090 (2004).

- [28] D.R. Lide (Editor in Chief), *Handbook of Chemistry and Physics* **86th ed.**, CRC press:Boca Raton, FL, 9-54 (2006).
- [29] S. Timoshenko, D. H. Young, and W. Weaver, Jr., *Vibration Problems in Engineering* **4th ed.**, John Wiley & Sons, (1974).
- [30] B.D. Hauer, C. Doolin, K.S.D. Beach, and J.P. Davis, *Annals of Physics* **339**, 181-207 (2013).
- [31] M. Bao, *Analysis and Design Principles of MEMS Devices* **1st ed.**, Elsevier B. V., (2005).
- [32] M. P. Norton and D.G. Karczub, *Fundamentals of Noise and Vibration Analysis for Engineers* **1st ed.**, Cambridge University Press, (2003).
- [33] M. J. Higgins, P. Proksch, J. E. Sader, M. Polcik, S. Mc. Endoo, J. P. Cleveland, and S. P. Jarvis, *Rev. Sci. Instrum.* **77**, 013701 (2006).
- [34] T. R. Albrecht, P. Grütter, D. Horne, and D. Rugar, *J. Appl. Phys.* **69**, 668 (1991).
- [35] K. L. Ekinici, Y. T. Yang, and M. L. Roukes, *J. Appl. Phys.* **95**, 2682 (2004).
- [36] Yin Zhang, *Sens. and Actuat. A: Physical* **194**, 169 (2013).
- [37] D.W. Dareing and T. Thundat, *J. Appl. Phys.* **97**, 043526 (2005).
- [38] H.P. Lang, M. Hegner, E. Meyer, and Ch. Gerber, *Nanotechnology* **13**, , R29 (2002).
- [39] S. Franssila, *Introduction to Micro Fabrication* **2nd Edition**, John Wiley and Sons Ltd, 2010.
- [40] A. N. Cleland, *Foundations of Nanomechanics* **2nd Edition**, Springer-Verlag Berlin Heidelberg, 2003.
- [41] T. Larsen, S. Schmid, L. Grönberg, A.O. Niskanen, J. Hassel, S. Dohn and A. Boisen, *Appl. Phys. Lett* **98**, 121901 (2011).
- [42] M. Eichenfield, R. Camacho, J. Chan, K.J. Vahala and Oskar Painter, *Nature* **459**, 550 (2009).

- [43] G. Anetsberger, O. Arcizet, Q.P. Unterreithmeier, R. Rivière, A. Schliesser, E.M. Weig, J.P. Kotthaus and T.J. Kippenberg, *Nature Phys.* **5**, 909 (2009).
- [44] K. Y. Fong, W. H. P. Pernice, Mo Li, and H. X. Tang, *Appl. Phys. Lett.* **97**, 073112 (2010).
- [45] A. N. Cleland, and M. L. Roukes, *J. Appl. Phys.* **97**, 2758 (2002).
- [46] D. R. Southworth, R. A. Barton, S. S. Verbridge, B. Ilic, A.D. Fefferman, H. G. Craighead, and J. M. Parpia, *Phys. Rev. Lett.* **102**, 225503 (2009).
- [47] A. K. Naik, M. S. Hanay, W. K. Hiebert, X. L. Feng, and M. L. Roukes, *Nature Nano.* **4**, 445 (2009).
- [48] S. Dohn, W. Svendsen, A. Boisen, and O. Hansen, *Rev. Sci. Instrum.* **78**, 103303 (2007).
- [49] W. A. P. Claassen, W. G. J. N. Valkenburg, M. F. C. Willemsen, and W. M. v.d. Wijgert, *J. Electrochem. Soc.* **132**, 893 (1985).
- [50] G. D. Cole, I. Wilson-Rae, K. Werbach, M. R. Vanner, and M. Aspelmeyer, *Nature Commun.* **2**, 231 (2011).
- [51] Schmid, S.; Jensen, K. D.; Nielsen, K. H.; Boisen A. *Phys. Rev. B* **2011**, 84, 165307.
- [52] T. P. M. Alegre, A. H. Safavi-Naeini, M. Winger, and O. Painter, *Opt. Express* **19**, 5658 (2011).
- [53] J. Chan, T. P. M. Alegre, A. H. Safavi-Naeini, J. T. Hill, A. Krause, S. Grblacher, M. Aspelmeyer, and O. Painter, *Nature* **478**, 89 (2011).
- [54] D.W. Allan, *IEEE Trans. on Ultrason., Ferroelec., and Freq. Control* **6**, 647 (1987).
- [55] A. K. Naik, M. S. Hanay, W. K. Hiebert, X. L. Feng, and M. L. Roukes, *Nature Nano.* **4**, 445–450 (2009).
- [56] M. S. Hanay, S. Kelber, A. K. Naik, D. Chi, S. Hentz, E. C. Bullard, E. Colinet, L. Duraffourg, and M. L. Roukes, *Nat. Nanotechnol.* **7**, 602 (2012).

- [57] J. Chaste, A. Eichler, J. Moser, G. Ceballos, R. Rurali ; A. Bachtold, *Nat. Nanotechnol.* **7**, 301 (2012).
- [58] J. R. Barnes, R. J. Stephenson, M. E. Welland, Ch. Gerber, and J. K. Gimzewski, *Nature* **372**, 79-81 (1994).
- [59] E. T. Arakawa, N. V. Lavrik, S. Rajic, and P. G. Datskos, *Ultramicroscopy* **97**, 459 (2003).
- [60] A. Wig, E. T. Arakawa, A. Passian, T. L. Ferrell, and T. Thundat, *Sensor Actuat. B-Chem.* **114**, 206 (2006).
- [61] A. R. Krause, C. V. Neste, L. Senesac, T. Thundat, and E. Finot, *J. of Appl. Phys.* **103**, 094906 (2008).
- [62] T. Larsen, S. Schmid, L. G. Villanueva, and A. Boisen, *ACS Nano.* **7**, 6188 (2013).
- [63] S. Yamada, S. Schmid, T. Larsen, O. Hansen, and A. Boisen, *Anal. Chem.* **85**, 10531 (2013).
- [64] S. Kim, D. Lee, and T. Thundat, *EPJ Tech. Instrum.* **1**, 7 (2014).
- [65] T. S. Biswas, J. Xu, X. Rojas, C. Doolin, A. Suhel, K. S. D. Beach, and J. P. Davis, *Nano Lett.* **14**, 14, 2541 (2014).
- [66] C. W. Van Neste, L. R. Senesac, D. Yi, and T. Thundat, *Appl. Phys. Lett.* **92**, 134102 (2008).
- [67] E. Finot, V. Rouger, L. Markey, R. Seigneuric, M.-H. Nadal, and T. Thundat, *Sensors and Actuators B: Chemical* **169**, 222 (2012).
- [68] J. Faist, F. Capasso, D. L. Sivco, C. Sirtori, A. L. Hutchinson, and A. Y. Cho, *Science* **264**, 553 (1994).
- [69] X. Liu, C. W. Van Neste, ; M. Gupta, Y. Y. Tsui, S. Kim, and T. Thundat, *Sensor Actuat. B-Chem* **191**, 450 (2014).
- [70] T.S. Biswas, A. Suhel, B.D. Hauer, K.S.D. Beach and J.P. Davis, *Appl. Phys. Lett* **101**, 093105 (2012).
- [71] M. Li, H. X. Tang, M. L. Roukes, *Nat. Nanotechnol.* **2007**, 2, 114 - 120.

- [72] S. Lee, V. P. Adiga, R. A. Barton, A. M. van der Zande, G.-H. Lee, B. R. Ilic, A. Gondarenko, J. M. Parpia, H. G. Craighead, and J. Hone, *Nano Lett.* **13**, 4275 (2013).
- [73] V. P. Adiga, R. De Alba, I. R. Storch, P. A. Yu, B. Ilic, R. A. Barton, S. Lee, J. Hone, P. L. McEuen, J. M. Parpia, and H. G. Craighead, *Appl. Phys. Lett.* **103**, 143103 (2013).
- [74] M. D. LaHaye, J. Suh, P. M. Echternach, K. C. Schwab, and M. L. Roukes, *Nature* **459**, 960 (2009).
- [75] E. Gavartin, P. Verlot, and T. J. Kippenberg, *Nature Nano.* **7**, 509 (2012).
- [76] T. Faust, P. Krenn, S. Manus, J.P. Kotthaus, and E.M. Weig, *Nat. Commun.* **3**, 728 (2012).
- [77] C. Doolin, P. H. Kim, B. D. Hauer, A. J. R. MacDonald, J. P. Davis, *New J. Phys.* **16**, 035001 (2014).
- [78] M. Pernpeintner, T. Faust, F. Hocke, J.P. Kotthaus, E.M. Weig, H. Huebl, and R. Gross, *Appl. Phys. Lett.* **105**, 123106 (2014).
- [79] S.Kim, D. Lee, X. Liu, C. Van Neste, S. Jeon, and T. Thundat, *Sci. Rep.* **3**, 1111 (2013).
- [80] Y. T. Yang, C. Callegari, X. L. Feng, K. L. Ekinici, and M. L. Roukes, *Nano Lett.* **6**, 583–586 (2006).
- [81] K. Jensen, K. Kim, and A. Zettl, *Nature Nano.* **3**, 533 (2008).
- [82] J. Chaste, A. Eichler, J. Moser, G. Ceballos, R. Rurali, and A. Bachtold, *Nature Nano.* **7**, 301 (2012).
- [83] S. Olcum, N. Cermak, S. C. Wasserman, *et al.*, *PNAS*, **111** 1310–1315 (2014).
- [84] K.L. Ekinici, X.M.H. Huang, and M.L. Roukes, *Appl. Phys. Lett.* **84**, 4469, 2004.
- [85] B.Ilic, Y. Yang, and H.G. Craighead, *Appl. Phys. Lett.* **85**, 2604, 2004.
- [86] B. Ilic, H.G. Craighead, S. Krylov, W. Senaratne, C. Ober, and P. Neuzil, *J. Appl. Phys.* **95**, 3694, 2004.

- [87] V. T. K. Sauer, M. R. Freeman, and W. K. Hiebert, *J. Micromech. Microeng.* **20**, 105020 (2010).
- [88] J. Lee, A. K. Bryan, and S. R. Manalis, *Rev. Sci. Instrum.* **82**, 023704 (2011).
- [89] J. D. Parkin and G H ahner, *Rev. Sci. Instrum.* **82**, 035108 (2011).
- [90] D. Kim, S. Hong, J. Jang, and J. Park, *Appl. Phys. Lett.* **103**, 033108 (2013).
- [91] R. Perenon, E. Sage, A. Mohammad-Djafari, L. Duraffourg, S. Hentz, A. Brenac, R. Morel, and P. Grangeat, *Proceedings of the 21st European Signal Processing Conference*, 1–5 (2013).
- [92] S. Dohn, W. Svendsen, A. Boisen, and O. Hansen, *Rev. Sci. Instrum.* **78**, 103303 (2007).
- [93] I. Stachiv, A. I. Fedorchenko, and Y.-L. Chen, *Appl. Phys. Lett.* **100**, 093110 (2012).
- [94] T.S. Biswas, Jin Xu, N. Miriyala, C. Doolin, T. Thundat, J.P. Davis, and K.S.D. Beach, *Phys. Rev. Applied.* **3**, 064002 (2015).
- [95] Y. T. Yang, C. Callegari, X. L. Feng, and M. L. Roukes, *Nano Lett.* **11**, 1753–1759 (2011)
- [96] A. Tavernarakis, J. Chaste, A. Eichler, G. Ceballos, M. C. Gordillo, J. Boronat, A. Bachtold, *Phys. Rev. Lett.* **112**, 196103 (2014)
- [97] Ann-Lauriene Haag, Y. Nagai, R. B. Lennox and P. Grütter, *EPJ Techniques and Instrumentation* **2**, 1 (2015).
- [98] R. Sandberg, K. Molhave, A. Boisen and W. Svendsen, *J. Micromech. Microeng.* **15** 2249 (2005).
- [99] G. Sosale, K. Da, L. Fréchet and S. Vengallatore, *J. Micromech. Microeng.* **21**, 105010 (2011).
- [100] A. Labuda, J.R. Bates and P.H. Grütter, *Nanotechnology* **23**, 025503 (2012).
- [101] M. Godin, V. Tabard-Cossa, Y. Miyahara, T. Monga, P.J. Williams, L.Y. Beaulieu, R.B. Lennox and P.H. Grütter, *Nanotechnology* **21**, 075501 (2010).

- [102] J.K. Gimzewski, Ch. Gerber, E. Meyer and R.R. Schlittler, *Chemical Physics Letters* **217**, 589 (1994).
- [103] J.R. Barnes, R.J. Stephenson, C.N. Woodburn, S.J. O'Shea, M.E. Welland, T. Rayment, J.K. Gimzewski and Ch. Gerber, *Rev. Sci. Instrum.* **65**, 3793 (1994).
- [104] J. Varesi, J. Lai, T. Perazzo, Z. Shi and A. Majumdera, *Appl. Phys. Lett* **71**, 306 (1997).
- [105] R. Berger, H.P. Lang, Ch. Gerber, J.K. Gimzewski, J.H. Fabian, L. Scandella, E. Meyer and H.-J. Güntherodt, *Chemical Physics Letters* **294**, 363 (1998).
- [106] J. Zhao, X. Yin, J. Shi, X. Zhao and J.S. Gutmann, *J. Phys. Chem. C* **115**, 22347 (2011).
- [107] D. Yi, A. Greve, J.H. Hales, L.R. Senesac, Z.J. Davis, D.M. Nicholson, A. Boisen and T. Thundat, *Appl. Phys. Lett.* **93**, 154102 (2008).
- [108] E. Iervolino, A.W. van Herwaarden, W. van der Vlist and P.M. Sarro, *J. Microelectromechanical Systems* **20**, 1277 (2011).
- [109] T. Liu, S. Pihan, M. Roth, M. Retsch, U. Jonas, J.S. Gutmann, K. Koynov, H.-J. Butt and R. Berger, *Macromolecules* **45**, 862 (2012).
- [110] I. Bargatin, I. Kozinsky and M.L. Roukes, *Appl. Phys. Lett.* **90**, 093116 (2007).
- [111] J. H. Seo and O. Brand, *J. Microelectromech. Syst.* **17**, 483 (2008).
- [112] L.G. Villanueva, R.B. Karabalin, M.H. Matheny, E. Kenig, M.C. Cross and M.L. Roukes, *Nano. Lett.* **11**, 5054 (2011).
- [113] M. Zalalutdinov, A. Zehnder, A. Olkhovets, S. Turner, L. Sekaric, B. Illic, D. Czaplewski, J.M. Parpia, and H.G. Craighead, *Proc. of SPIE* **4561**, 189 (2001).
- [114] J.P. Davis, D. Vick, D.C. Fortin, J.A.J. Burgess, W.K. Hiebert and M.R. Freeman, *Appl. Phys. Lett.* **96**, 072513 (2010).
- [115] X. Sun, K. Y. Fong, C. Xiong, W. H. P. Pernice, and H. X. Tang, *Opt. Express* **19**, 22316 (2011).

- [116] I. Horvath, Z. Lazar, N. Gyulai, M. Kollai and G. Losonczy, *Eur Respir J* **34**, 261-275 (2009).
- [117] C. Deng, J. Zhang, X. Yu, W. Zhang, X. Zhang, *Journal of Chromatography B* **820** , 269 (2004).
- [118] M. Li, S. Biswas, M.H. Nantz, R.M. Higashi and X. Fu, *Sensors and Actuators B* **180**, 130-136 (2013).
- [119] D. Graham, S. Dingman, *Material Matters* **1.2** , 18 (2006).
- [120] H. Ding, Ji-Shi Wei, and Huan-Ming Xiong, *Nanoscale* **6**, 13817 (2014).
- [121] L.G. Wade, Jr. *Organic Chemistry 6th Edition*, Pearson Prentice Hall, 2006.
- [122] D. K. T. Ng, Q. Wang, T. Wang, Siu-Kit Ng, Yeow-Teck Toh, Kim-Peng Lim, Y. Yang, and D. T. H. Tan, *ACS Appl. Mater. Interfaces* **7**, 21884 (2015).

APPENDIX A

Frequency variation in terms of optical power

A.1 Frequency stability of a silicon nitride string

In this section we will show if there is any heating effect on a silicon nitride string when a red laser impinges on it. The incident laser power on the string varies from $\sim 5\text{--}450\ \mu\text{W}$. However, silicon nitride has a negligible absorption in red laser [122]. Hence we expect no frequency variation with this laser. As it is seen in Fig. A.1,

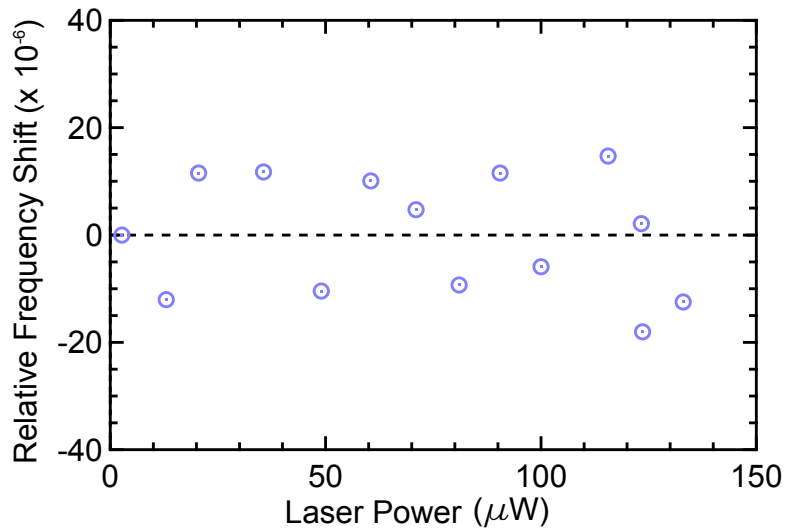


Figure A.1: Frequency variation of a 215 μm long string with respect to incident optical power.

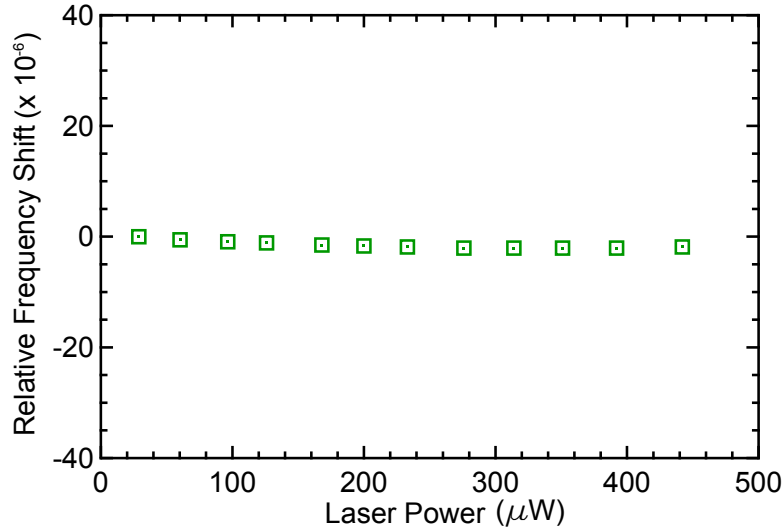


Figure A.2: Frequency variation of a 200 μm long string with respect to incident optical power.

we change the laser power and record the corresponding resonance frequency and the frequency shift is arbitrary and within the limit of ± 20 Hz. If there is any absorption occurs in this laser light then one could expect to get a trend in frequency shift in downward. In practice, we do not see any kind of that trend here. The arbitrary change in resonance frequency comes from the resultant system instability when the laser power is changed manually by the attenuator sitting on the stage. This mechanical noise can be reduced by taking the data more careful way without disturbing the system much. Fig. A.2 Shows a nice example with less disturbance during the data taking. To compare these two results we keep the vertical axes with same scales. It is noticed that this time the variation is in between ± 4 Hz only, which is 5 times smaller than before. It is also worth noting that the laser power tuned to higher values in the later measurement. From these observation, it is confirmed that there is no heating effect due to the red laser for a silicon nitride nanostring.

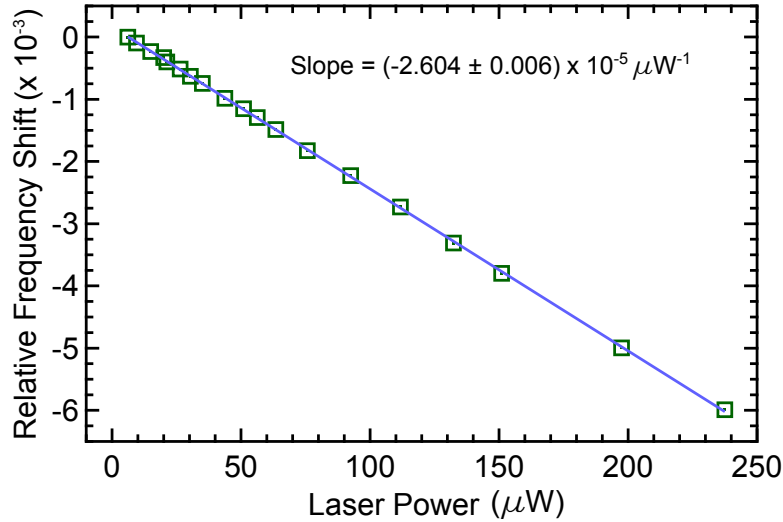


Figure A.3: Frequency variation of a 175 μm long string with respect to incident optical power.

A.2 Frequency variation of a gold and silicon nitride bilayer nanostring as a function of optical power.

It is observed opposite in case of a gold coated silicon nitride nanostring. Since gold is a good conductor and it has an absorption coefficient in visible range, hence light is absorbed when it shines on it. Absorbed light produces heat and results in the shift in resonance frequency downward.

Fig. A.3 shows the frequency shift as a function of incident laser power. It is observed that it has a strong influence on the metal coated string. There is a ~ 25 Hz shift for 1 μW change of laser power. So it is little bit tricky when we have to use gold coated string. It is recommended to keep the laser power as low as possible. In most of our experiment, we keep the laser power < 20 μW for a gold coated string. So it is hard to do the alignment and signal amplitude also gets lower. In contrast for a silicon nitride string, we can keep as high as possible to get maximum interference signal.

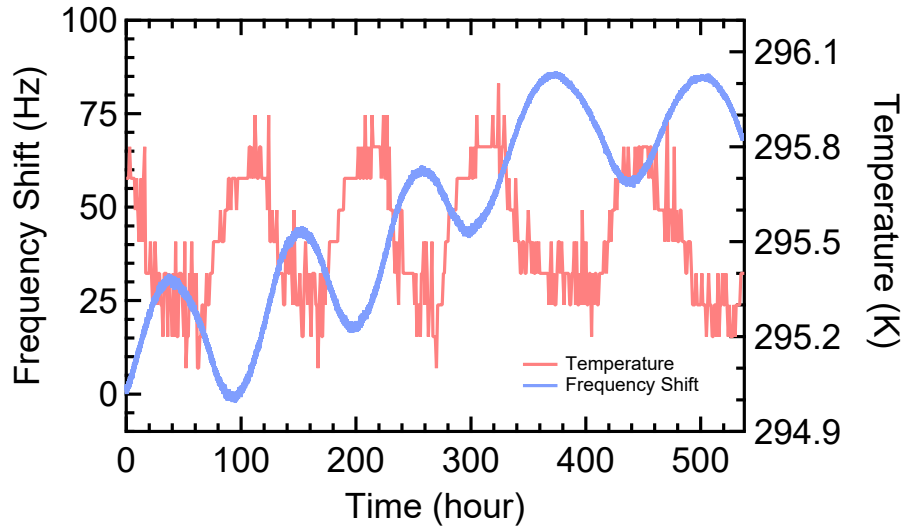


Figure A.4: Frequency variation of a $175 \mu\text{m}$ long string with respect to time.

A.3 Frequency stability of a silicon nitride string over a long period of time

It is nice to check the system stability over a long period of time. The Zurich instrument provides a nice feature PLL which can be used to track the resonance frequency of a resonator for such a long time. As it is seen in Fig. the frequency of a $50 \mu\text{m}$ long string changes periodically over the time of 8 hours. The total frequency shift is 150 Hz. But it is interesting to dig out the reason to get that periodicity in the frequency with a 103 min long wavelength.

As the experiment was run overnight at the lab, there was no mechanical shift or any other man made disturbance. So only thing was in our mind about the temperature of the room. Since the temperature of the room is controlled by a thermistor so there is a good chance to get the variation on that parameter. Hence a calibrated thermometer is placed near to the vacuum chamber and monitored for the whole period of time during the experiment. It is nice to see that the same periodicity is observed in temperature profile of the room. Almost similar wavelength in periodicity is noticed here. The only discrepancy here is that crest

and trough are not at the same position for temperature and frequency profiles. The best explanation for this is that the thermometer was not placed inside the vacuum chamber so the gradient of temperature certainly is different from the atmosphere. It might be possible to get better picture with detail modeling and experimentation of the system.

APPENDIX B

FIB milling of silicon nitride string

In this Appendix, I will show an alternative way to make resonators with small dimensions. Focused ion beam is a technique which can be used to remove materials physically by targeting focused Ga ions. We know that with optical lithography it is not possible to go below the resolution of $1.5\ \mu\text{m}$ using the optical lithography tool in our nanoFab. Hence it is decided to use a bypass technique to fabricate those devices which need small dimensions like $< 1.5\ \mu\text{m}$. Moreover it is well known that there is a overhang after the isotropic wet etch to release a resonator. FIB could be one of the techniques to remove that undercut. Keeping those two things in mind, I proceeded to make few devices by FIB milling.

Initially the devices are made by standard optical lithography process and released

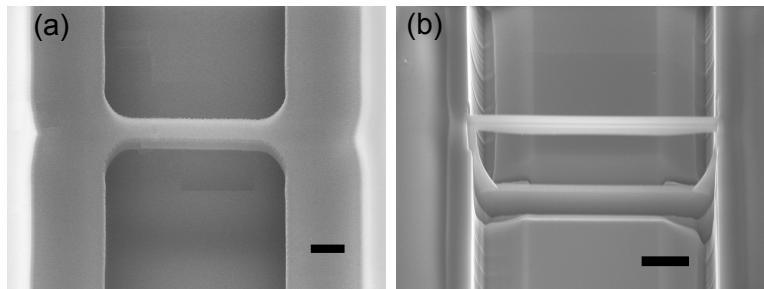


Figure B.1: (a) A released device fabricated by optical lithography process. (b) The same device is trimmed by FIB milling to reduce the width and to remove the undercut. Scale bars are $1\ \mu\text{m}$ long and $2\ \mu\text{m}$ long respectively.

by BOE etch. Then this device is trimmed by FIB milling process to remove the overhang part and also to reduce the width of the device. Fig. B.1(a) shows SEM image of a $5\ \mu\text{m}$ long device that is fabricated by optical lithography processed. This device is released in BOE solution which left $\sim 2\ \mu\text{m}$ undercut on each side. The device is then trimmed by FIB milling as shown in Fig.B.1(b). The device is now $\sim 400\ \text{nm}$ wide and $\sim 10\ \mu\text{m}$ long. To compare the quality factor and resonance frequency of a device before and after trimming, data was taken from a device of $124\ \mu\text{m}$ long as shown in Fig. B.2. The quality factor of the device was 220 k before trimming the device. The device's effective length increased by at least $4\ \mu\text{m}$ after trimming the overhang and width of the string that leads to a decrease in the resonance frequency as shown in Fig. B.2(c-d). Fig. B.2(c) and (d) show the frequency sweeps of the device after trimming for both thermomechanical actuation and driven data respectively. However the quality factor of the device decreased by almost factor of 4 compared to the quality factor of the device before FIB milling. The Ga ions penetrate through the substrate approximately $30\ \text{nm}$ and hence it could destroy the internal stress of silicon nitride material. As a result the resonance frequency and the quality factor also decreased.

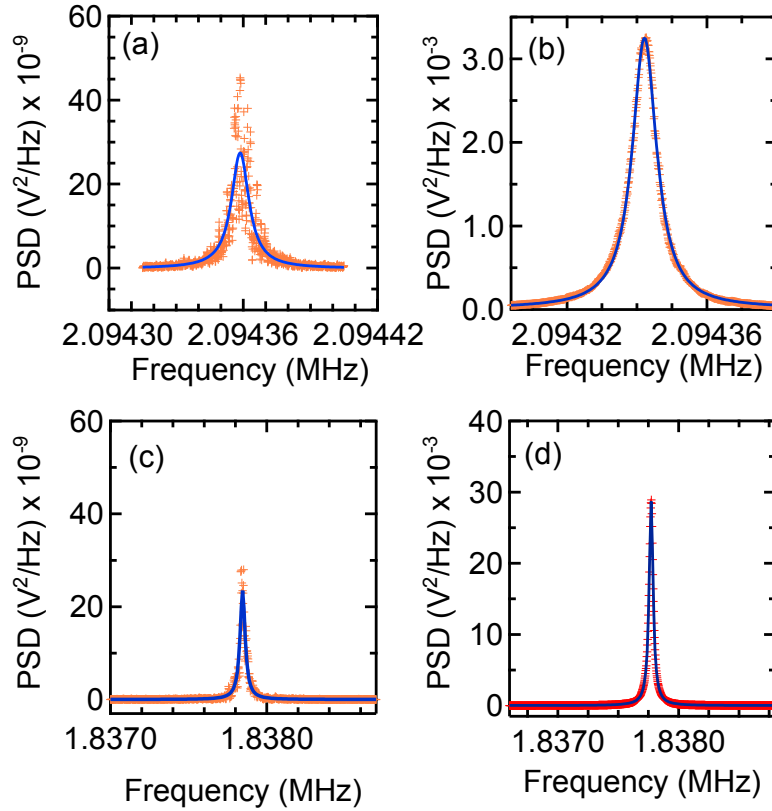


Figure B.2: Frequency sweep of a $124 \mu\text{m}$ long string (a–b) before and (c–d) after trimming by FIB milling. (a) and (c) present data due to thermomechanical actuation. (b) and (d) present driven data. The corresponding line widths are 11.9, 8.48, 38.8 and 39.81 Hz for (a), (b), (c), and (d) respectively.

APPENDIX C

Objective Comparison

In our optical interferometric technique, an objective is an essential part of the system. Usually a long working distance objective is selected. However, the question is which magnification is optimum. I showed a data comparison for first three modes of a 130 μm long string. For the first mode, it is seen that signal amplitude is better for a 20x objective. However signal amplitudes look similar for all other modes. One should keep in mind that if it is necessary to see small devices then it is better to select high resolution objective. I have used 50x objective in my data acquisition process for this thesis.

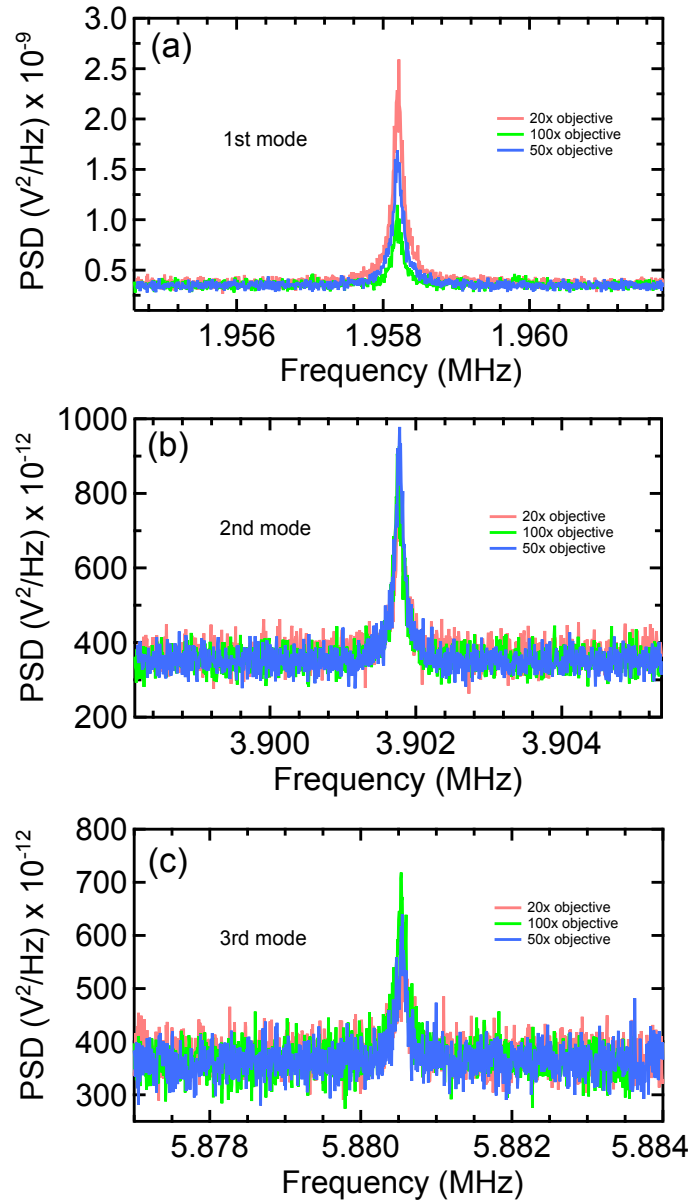


Figure C.1: Frequency sweep of (a) first mode, (b) second mode, and (c) third mode of a 130 μm long string using 20x, 50x and 100x long working distance objectives. The line widths are 172, 166, and 151 Hz for 20x, 50x, and 100x objectives for the first mode. The line widths are 153, 148, and 145 Hz for 20x, 50x, and 100x objectives for the second mode. The line widths are 160, 139, 178 Hz for 20x, 50x, and 100x objectives for the third mode.

APPENDIX D

Sublimation Model ¹

D.1 Sublimation model

In Chapter 7, we have observed that when RDX deposited to the nanostring they are stuck to the surface and do not sublime at ambient condition. Interestingly, they start to sublime slowly under vacuum (10^{-4} torr). We have the capability, however, to make ongoing measurements of the resonance frequencies; these change continuously in time as the adsorbate molecules are removed from the nanostring because of the vacuum environment.

Therefore it is useful to sketch out a model of how the mass on the string evolves with time in our experimental setup. The basic assumption is that the molecules are either residing on the string (m) or existing as vapor in the chamber (m_v). RDX sublimates from the string surface at a uniform rate α , and there is an incoming flux of molecules returning to the surface due to intermolecular collisions, denoted by β . Finally, there is γ , the rate at which the chamber is being evacuated. This picture leads to a coupled pair of rate equations:

$$\frac{d}{dt} \begin{pmatrix} m \\ m_v \end{pmatrix} = \begin{pmatrix} -\alpha & \beta \\ \alpha & -(\beta + \gamma) \end{pmatrix} \begin{pmatrix} m \\ m_v \end{pmatrix}. \quad (\text{D.1})$$

As a consequence, there are two rate constants, given by the eigenvalues of the matrix. When $\gamma = 0$, the eigenvalues are $\lambda_1 = 0$ and $\lambda_2 = \alpha + \beta$; hence, the system

¹A version of this section has been published. Biswas *et al.*, *Phys. Rev. Applied.* **3**, 064002 (2015).

equilibrates at a rate $\alpha + \beta$ to a steady state with $m_v/m = \alpha/\beta$. On the other hand, when γ is a fast rate—the experimentally relevant situation—we find that

$$\begin{aligned}\lambda_1 &= -\alpha + \frac{\alpha\beta}{\gamma} + \frac{\alpha\beta(\alpha - \beta)}{\gamma^2} + O(\gamma^{-3}), \\ \lambda_2 &= -\gamma - \beta - \frac{\alpha\beta}{\gamma} - \frac{\alpha\beta(\alpha - \beta)}{\gamma^2} + O(\gamma^{-3}).\end{aligned}\tag{D.2}$$

The full time dependence of m and m_v is then given by

$$\begin{aligned}\begin{pmatrix} m(t) \\ m_v(t) \end{pmatrix} &= \frac{\gamma m(0) + \beta m_v(0)}{\gamma^2 + \alpha\beta} \begin{pmatrix} \gamma \\ \alpha \end{pmatrix} e^{-(\alpha - \alpha\beta/\gamma)t} \\ &\quad + \frac{\gamma m_v(0) - \alpha m(0)}{\gamma^2 + \alpha\beta} \begin{pmatrix} -\beta \\ \gamma \end{pmatrix} e^{-(\gamma + \beta + \alpha\beta/\gamma)t}.\end{aligned}\tag{D.3}$$

For times $t \gg (\gamma + \beta + \alpha\beta/\gamma)^{-1}$, the mass on the string decays according to

$$m(t) = \frac{m(0) + (\beta/\gamma)m_v(0)}{1 + \alpha\beta/\gamma^2} e^{-\alpha(1 - \beta/\gamma)t}.\tag{D.4}$$

Moreover, if the chamber is being very aggressively evacuated, then the behavior looks like

$$m(t) = m(0)e^{-\alpha_{\text{eff}}t},\tag{D.5}$$

with $\alpha_{\text{eff}} = \alpha - \alpha\beta/\gamma \approx \alpha$ close to the intrinsic sublimation rate of the adsorbate, and we can safely proceed as if $m_v \approx 0$ at all times after the pump has been activated.

A refinement of this model is to consider the possibility that the rate of mass loss goes as a fractional power of the current mass load. This may be appropriate here since the RDX on the surface is known to aggregate, rather than arranging in a smooth monolayer. Sublimation in that case is likely to be at least partially controlled by loss from the surface area of the RDX crystallites ($A \sim m^{2/3}$), which puts a lower bound of $2/3$ on the effective scaling exponent.

If the distribution of crystallites along the device is roughly uniform, then we can account for this situation as follows:

$$\frac{dm}{dt} = -\alpha m_\star (m/m_\star)^\phi.\tag{D.6}$$

This description requires that we introduce a new material-specific mass scale m_\star

and a phenomenological exponent ϕ . We anticipate a value $2/3 \leq \phi \leq 1$, with conventional exponential decay recovered at the upper end of that range. When $\phi \neq 1$, we find that

$$\frac{dm}{m^\phi} = \frac{1}{1-\phi} d(m^{1-\phi}) = -\alpha m_\star^{1-\phi} dt.$$

This leads to

$$m(t) = m(0) \left[1 - \frac{t}{t_r} \right]^{1/(1-\phi)}, \quad (\text{D.7})$$

where, $t_r = [m(0)/m_\star]^{1-\phi}/\alpha(1-\phi)$ is the finite removal time after which all RDX has left the nanostring.

We now emphasize an important feature that distinguishes between the two kinds of behavior. When $\phi = 1$, the decay is exponential at a constant rate

$$-\frac{1}{t} \log \frac{m(t)}{m(0)} = \alpha. \quad (\text{D.8})$$

For a nontrivial value of the exponent, however, the mass loss is characterized by an apparent decay rate that increases over time:

$$\begin{aligned} -\frac{1}{t} \log \frac{m(t)}{m(0)} &= -\frac{1}{(1-\phi)t} \log \left[1 - \frac{t}{t_r} \right] \\ &= \frac{1}{(1-\phi)t_r} \left[1 + \frac{t}{2t_r} + \frac{t^2}{3t_r^2} + \dots \right] \\ &= \alpha \left(\frac{m_\star}{m(0)} \right)^{1-\phi} \left[1 + \frac{(1-\phi)\alpha t}{2} \left(\frac{m_\star}{m(0)} \right)^{1-\phi} \right. \\ &\quad \left. + \dots \right]. \end{aligned} \quad (\text{D.9})$$

Finally, a more complete description must account for a mass distribution that varies along the length of the string. We treat the deposited mass $\delta\mu(x, t)$ as a space- and time-dependent field subject to the governing equation

$$\frac{\partial}{\partial t} \delta\mu(x, t) = -\alpha \mu_\star \left(\frac{\delta\mu(x, t)}{\mu_\star} \right)^\phi. \quad (\text{D.10})$$

Here, μ_\star is a stand in for m_\star/L . In the previously considered situations where either $\phi = 1$ or the the initial mass distribution is uniform, the mass distribution simply

shrinks away while preserving its overall shape. That is not generally true:

$$\delta\mu(x, t) = \left[\delta\mu(x, 0)^{1-\phi} - (1-\phi)\alpha\mu_\star^{1-\phi}t \right]^{1/(1-\phi)}. \quad (\text{D.11})$$

Equation (D.11) also makes clear that, unlike in Eq. (D.7), $\delta\mu$ reaches zero at a removal time that is different at each point along the string.

With Eq. (D.11) in hand, it is straightforward to obtain the time-dependent total mass

$$m(t) = \int_0^L dx \delta\mu(x, t) \quad (\text{D.12})$$

or any of the relative frequency shifts

$$-\frac{\delta\omega_n(t)}{\omega_n} = \frac{1}{M} \int_0^L dx \delta\mu(x, t) \sin^2\left(\frac{n\pi x}{L}\right). \quad (\text{D.13})$$